

Summer 2000

Electroweak Structure of Three-and Four-Body Nuclei

Laura Elisa Marcucci
Old Dominion University

Follow this and additional works at: https://digitalcommons.odu.edu/physics_etds



Part of the [Nuclear Commons](#)

Recommended Citation

Marcucci, Laura E.. "Electroweak Structure of Three-and Four-Body Nuclei" (2000). Doctor of Philosophy (PhD), Dissertation, Physics, Old Dominion University, DOI: 10.25777/5n5r-7213
https://digitalcommons.odu.edu/physics_etds/52

This Dissertation is brought to you for free and open access by the Physics at ODU Digital Commons. It has been accepted for inclusion in Physics Theses & Dissertations by an authorized administrator of ODU Digital Commons. For more information, please contact digitalcommons@odu.edu.

ELECTROWEAK STRUCTURE OF THREE- AND FOUR-BODY NUCLEI

by

Laura Elisa Marcucci

Laurea, November 1995. Department of Physics, University of Pisa. Pisa (Italy)

A Dissertation Submitted to the Faculty of
Old Dominion University in Partial Fullfillment of the
Requirement for the Degree of

DOCTOR OF PHILOSOPHY

PHYSICS

OLD DOMINION UNIVERSITY

June 2000


Approved by: 

Rocco Schiavilla (Director)

Mark Havev

Sebastian Kuhn

Anatoly Radyushkin

Nancy Xu 

UMI Number: 9970448



UMI Microform 9970448

Copyright 2000 by Bell & Howell Information and Learning Company.

All rights reserved. This microform edition is protected against
unauthorized copying under Title 17, United States Code.

Bell & Howell Information and Learning Company
300 North Zeeb Road
P.O. Box 1346
Ann Arbor, MI 48106-1346

ABSTRACT

ELECTROWEAK STRUCTURE OF THREE- AND FOUR-BODY NUCLEI

Laura Elisa Marcucci
Old Dominion University, 2000
Director: Dr. Rocco Schiavilla

This work reports results for (i) the elastic electromagnetic form factors of the trinucleons; (ii) the nuclear response functions of interest in ${}^3\text{He}(\vec{e}, e')$ experiments, at excitation energies below the deuteron breakup threshold; (iii) the astrophysical S -factor for proton weak capture on ${}^3\text{He}$ (the hep reaction). The initial and final state wave functions are calculated using the correlated hyperspherical harmonics method, from a realistic Hamiltonian consisting of the Argonne v_{18} two-nucleon and Urbana IX three-nucleon interactions. The nuclear electroweak charge and current operators include one- and many-body components. The predicted magnetic form factor of ${}^3\text{H}$, charge form factors and static properties of both ${}^3\text{H}$ and ${}^3\text{He}$, are in satisfactory agreement with the experimental data. However, the position of the zero in the magnetic form factor of ${}^3\text{He}$ is underpredicted by theory. The calculated nuclear response functions in ${}^3\text{He}$ electrodisintegration at threshold are in good agreement with the experimental data, which have however rather large errors. Finally, the astrophysical S -factor for the hep reaction is predicted $\simeq 4.5$ larger than the value adopted in the standard-solar-model, with important consequences for the solar neutrino spectrum measured by the Super-Kamiokande collaboration.

Acknowledgements

I am grateful to many people who have supported and helped me during these four years of graduate studies. I hope I will mention all of them, without forgetting anybody.

First of all, I would like to thank my advisor Rocco Schiavilla, who has helped me during this work in many different ways, with useful suggestions and advice. His experience and understanding in the field of nuclear physics have given me fundamental insights in all my research projects. I would like to thank also Rocco and especially his wife Lynn for helping me to get settled here in Virginia, when I had just arrived and could barely speak and understand English. I am particularly thankful to Lynn for her constant support during all these years.

Great support has come to me also from the Physics Department of Old Dominion University. I would like to thank everybody for it. In particular, I would like to thank my committee members, Mark Havey, Sebastian Kuhn, Anatoly Radyushkin and Nancy Xu, for all their suggestions during this work. I am also very grateful to Andreas Klein for teaching me how to use the LSF system and for being always ready to help and solve any of the problems I experienced while running my codes. Without his help, my last research project would not yet be completed.

In these years, I spent most of my time at Jefferson Lab: I would like to thank the Theory Group, for giving me hospitality and allowing me to use permanently one of the offices. Furthermore, in these years everybody has always been ready to help, for any question or problem I had; in particular, I am very grateful to Jiri Adam and Jun Forest, my patient officemates, and Sabine Jeschonnek and

Rich Lebed. The possibility I had of interacting with the members of the Theory Group, of listening to the talks they gave or organized, of meeting visitors of the Lab and learning about physics not necessarily related to my particular field, but still interesting and exciting, have been of great help in my education as a physics researcher.

I would like to thank Sergio Rosati, Alejandro Kievsky, Michele Viviani and the whole Nuclear Theory Group of the Pisa University. During these years, their support has always been a reference point for me: the discussions on our common projects, the sharing of Fortran codes, and the CPU time I could use on Michele's computer have been of great importance for me, enabling me to complete this work. I am very grateful also to Dan-Olof Riska and John Beacom for the research projects we completed together, and for sharing with me their ideas and knowledge.

I would like to thank all my friends, which have supported and helped me in each moment, through all these years. Most of all, thanks to my "Rumanian sister" Luminita Todor and her wonderful family, which has always been there whenever I needed. Her support, from the very first moment we met in Jefferson Lab, through the classes we took together, till these very last stressful months, has been immeasurable. I would like to thank also Francesca and Dick McCleary, for supporting me in every moment even from such a long distance, after they moved to London. Thanks also to my friends Rama Balasubramanian, Jeff Waller, Gilles Quemener, Sheila Norman and Moira Piccirilli.

As last, but also as most important, I would like to thank my family and my fiance Michael. My family has always supported me, being at my side even if in fact living so far from me. During these four years, I have always known that I could count on them for any help I might have needed. Their annual visits made much more tolerable the big distance that was between us. Finally, I give my most grateful thanks to Michael, whose love, patience, understanding and support have made my life much easier and much more beautiful. I would have never been able to conclude this work without his secure presence at my side.

Table of Contents

List of Tables	x
List of Figures	xiv
1 Introduction	1
2 The Nuclear Interaction	6
2.1 Two-Nucleon Interactions	6
2.2 Three-Nucleon Interactions	10
3 Bound- and Scattering-State Wave Functions	12
3.1 The Bound-State Wave Functions	13
3.1.1 The Three-Nucleon Wave Function	14
3.1.2 The ^4He Wave Function	16
3.2 The Scattering-State Wave Functions	20
3.2.1 The Method for Scattering-State Wave Functions	21
3.2.2 Results for Three- and Four-Body Scattering Problems . .	22
4 The Nuclear Transition Operators	25
4.1 The Electromagnetic Transition Operators	26
4.1.1 Nuclear Current and Charge Operators	26
4.1.2 The Two-Body Current Operators	28
4.1.3 The Three-Body Exchange Current Associated with S-wave Pion Rescattering	35
4.1.4 Two-Body Charge Operators	38
4.1.5 Δ -Isobar Components in the Wave Functions: the TCO Method	40
4.1.6 Electromagnetic Δ -Currents	44
4.2 The Weak Transition Operators	46
4.2.1 The Nuclear Weak Current and Charge Operators	47
4.2.2 Two-Body Weak Vector Current and Charge Operators . .	49

4.2.3	Two-Body Weak Axial Current Operators	50
4.2.4	Two-Body Weak Axial Charge Operators	51
4.2.5	Weak Δ -Contributions	53
5	Trinucleon Form Factors	55
5.1	Electron-Scattering from Nuclei	55
5.2	Calculation Details	60
5.3	Results	65
5.3.1	Nucleons Only	65
5.3.2	Nucleons and Δ 's	71
6	The ^3He Threshold Electrodintegration	76
6.1	The $^3\text{He}(\bar{e}, e')pd$ Reaction at Threshold	77
6.2	Calculation	81
6.3	Results	82
7	The hep Reaction	87
7.1	The hep Cross Section and Astrophysical S -factor	89
7.1.1	The Transition Amplitude	90
7.1.2	The Multipole Expansion	92
7.1.3	The Cross Section	93
7.2	Calculation	95
7.2.1	Monte Carlo Calculation of Matrix Elements	95
7.2.2	Calculation of the Cross Section	98
7.3	Results	101
7.3.1	Results for the S -factor	101
7.3.2	The 3S_1 and 3P_0 Captures	104
7.3.3	Implications for the Super-Kamiokande Solar Neutrino Spectrum	107
8	Conclusions	110
	Vita	120

List of Tables

I	Trinucleons binding energies in MeV corresponding to the AV14, AV18, AV14/UVIII and AV18/UIX Hamiltonian models. The PHH results for the AV14 potential are compared with those calculated by solving the Faddeev equations in configuration- (F/R) and in momentum-space (F/P). Also we compare the PHH and the GFMC results when the AV18/UIX potential model is used. The GFMC statistical errors are shown in parenthesis.	17
II	Binding energies in MeV of ${}^4\text{He}$ calculated with the CHH method using the AV18 and AV18/UIX and the older AV14 and AV14/UVIII potential models. Also listed are the corresponding “exact” GFMC results [4] and the experimental value. The GFMC statistical errors are shown in parenthesis.	20
III	Predictions obtained from the AV18/UIX Hamiltonian model with the PHH method for the nd and pd doublet and quartet scattering lengths a_2 and a_4	22
IV	Singlet a_s and triplet a_t S-wave scattering lengths (fm) for $n\,{}^3\text{H}$ scattering calculated with the AV14 and $p\,{}^3\text{He}$ scattering calculated with the AV18, AV18/UIX and the older AV14/UVIII potential models. The $n\,{}^3\text{H}$ Faddeev results and the $p\,{}^3\text{He}$ experimental values are also listed.	23
V	The wave function normalization ratios $\langle\Psi_{N+\Delta} \Psi_{N+\Delta}\rangle/\langle\Psi \Psi\rangle$ obtained for the bound three- and four-nucleon systems, when the TCO calculation is based on the AV28Q interaction. The purely nucleonic CHH wave functions $ \Psi\rangle$ correspond to the AV18/UIX Hamiltonian model.	44
VI	Cumulative and normalized contributions to the ${}^3\text{H}$ and ${}^3\text{He}$ r.m.s. charge radii. in fm, compared with the experimental data.	72

VII	Individual contributions from the different components of the nuclear electromagnetic current operator to the ${}^3\text{H}$ and ${}^3\text{He}$ magnetic moments and their μ_S and μ_V combinations, in nuclear magnetons (n.m.). Note that, because of isospin-symmetry breaking components present in the PHH ${}^3\text{H}$ and ${}^3\text{He}$ wave functions, purely isoscalar (isovector) currents give non vanishing contributions to the μ_V (μ_S) combination. The contributions to μ_S due to the $\pi\pi_S$ and $2\text{-}\Delta$ currents and those to μ_V due to the SO2+LL currents are very small and are not listed.	74
VIII	Cumulative and normalized contributions to the ${}^3\text{H}$ and ${}^3\text{He}$ magnetic moments and their μ_S and μ_V combinations, in nuclear magnetons (n.m.), compared with the experimental data.	75
IX	Cumulative and normalized contributions to the ${}^3\text{H}$ and ${}^3\text{He}$ r.m.s. magnetic radii, in fm, compared with the experimental data. . . .	75
X	Contributions to the Gamow-Teller (GT) matrix element of tritium β -decay, obtained with the PHH trinucleon wave functions corresponding to the AV18/UIX Hamiltonian model. The rows labelled "one-body NR" and "one-body RC" list the contributions associated with the single-nucleon axial current operators of Eq. (137) and Eq. (138), respectively, while the row labelled "mesonic" lists the sum of the contributions due to the π -, ρ -, and $\rho\pi$ -exchange axial current operators of Eqs. (142)–(144). The rows labelled " Δ - g_A^* " and " Δ - \bar{g}_A " list the contributions arising from the one-body Δ -currents of Eqs. (150) and (151), respectively. The row labelled " Δ -renormalization" lists the contributions associated with renormalization corrections to the "nucleonic" matrix element of $j_i^{(1)}(\mathbf{q}; A)$, due to the presence of Δ -admixture in the wave functions. The cumulative result reproduces the "experimental value" 0.957 for the GT matrix element [12], once the change in the wave functions normalization due to the presence of Δ -components is taken into account.	99
XI	The values of the $N \rightarrow \Delta$ axial coupling constant g_A^* in units of g_A , when the Δ -isobar degrees of freedom are treated in perturbation theory (PT), or in the context of a TCO calculation based on the AV28Q interaction. The purely nucleonic CHH wave functions correspond to the AV18/UIX Hamiltonian model.	99

- XII The *hep* *S*-factor, in units of 10^{-20} keV b, calculated with CHH wave functions corresponding to the AV18/UIX Hamiltonian model, at $p^3\text{He}$ c.m. energies $E=0, 5,$ and 10 keV. The rows labelled “one-body” and “full” list the contributions obtained by retaining the one-body only and both one- and many-body terms in the nuclear weak current. The contributions due the $^3\text{S}_1$ channel only and all S- and P-wave channels are listed separately. 102
- XIII Contributions of the S- and P-wave capture channels to the *hep* *S*-factor at zero $p^3\text{He}$ c.m. energy in 10^{-20} keV b. The results correspond to the AV18/UIX, AV18 and AV14/UVIII Hamiltonian models. 103
- XIV Cumulative contributions to the reduced matrix elements (RMEs) $\overline{C}_1(q; A), \overline{L}_1(q; A), \overline{E}_1(q; A)$ and $\overline{M}_1(q; V)$ in $^3\text{S}_1$ capture at zero $p^3\text{He}$ c.m. energy. The momentum transfer q is 19.2 MeV/c, and the results correspond to the AV18/UIX Hamiltonian model. The row labelled “one-body” lists the contributions associated with the operators in Eq. (135) for the weak axial charge $\rho(A)$, Eq. (136) for the weak axial current $\mathbf{j}(A)$, and Eq. (133) for the weak vector current $\mathbf{j}(V)$; the row labelled “mesonic” lists the results obtained by including, in addition, the contributions associated with the operators in Eqs. (145)–(147) for $\rho(A)$, Eqs. (142)–(144) for $\mathbf{j}(A)$, and Eqs. (88)–(89) for $\mathbf{j}(V)$, with the substitutions $\tau_{i,z} \rightarrow \tau_{i,\pm}$ and $(\boldsymbol{\tau}_i \times \boldsymbol{\tau}_j)_z \rightarrow (\boldsymbol{\tau}_i \times \boldsymbol{\tau}_j)_\pm$ (see Subsection 4.2.2); finally, the row labelled “ Δ ” lists the results obtained by also including the contributions of the operators in Eqs. (152)–(153) for $\rho(A)$, Eqs. (150)–(151) for $\mathbf{j}(A)$, and Eqs. (154)–(155) for $\mathbf{j}(V)$. The Δ contributions in both $\rho(A)$ and $\mathbf{j}(A)$ are calculated with the TCO method, and take into account the change in normalization of the wave functions due to the presence of Δ -components. Those in $\mathbf{j}(V)$ are calculated in perturbation theory. Note that the RMEs are purely imaginary and in $\text{fm}^{3/2}$ units. 105

- XV Cumulative contributions, at momentum transfers $q=0$ and 19.2 MeV/c, to the reduced matrix elements (RMEs) $\overline{L}_1(q; A)$ and $\overline{E}_1(q; A)$ of the weak axial current in 3S_1 capture at zero $p^3\text{He}$ c.m. energy. The results correspond to the AV18/UIX Hamiltonian model. Notations as in Table XIV for “one-body”, “mesonic” and “ Δ -TCO”, which there was labelled “ Δ ”. Finally, the row labelled “ Δ -PT” lists the results obtained by including the contributions of the operator in Eq. (150), calculated in perturbation theory (PT). The Δ -TCO results also take into account the change in normalization of the wave functions due to the presence of Δ -components. Note that the RMEs are purely imaginary and in $\text{fm}^{3/2}$ units. . . 106
- XVI Cumulative contributions to the reduced matrix elements (RMEs) $\overline{C}_0(q; A)$ and $\overline{L}_0(q; A)$ in 3P_0 capture at zero $p^3\text{He}$ c.m. energy. The momentum transfer q is 19.2 MeV/c. and the results correspond to the AV18/UIX Hamiltonian model. Notations as in Table XIV. Note that the RMEs are purely imaginary and in $\text{fm}^{3/2}$ units. . . 107

List of Figures

1	The Fujita and Miyazawa two-pion-exchange three-nucleon interaction diagram. Thin, thick, and dashed lines denote, respectively, nucleons, Δ -isobars and pions.	11
2	Differential cross section $\sigma(\theta)$ as function of the c.m. scattering angle θ , at c.m. energy of 1.2 MeV. The experimental data are taken from Ref. [48]. The long-dashed and solid lines correspond, respectively, to the CHH calculations with the AV18 and AV18/UIX Hamiltonian models.	24
3	Feynman diagram representation of the $\rho\pi\gamma$ and $\omega\pi\gamma$ transition operators. Solid, dashed, thick-dashed and wavy lines denote respectively nucleons, pions, vector-mesons and photons.	30
4	(a) OBE Feynman diagram representation; (b) Feynman diagram representation of the two-body currents associated with meson-exchange. Solid, dashed and wavy lines denote respectively nucleons, mesons and photons.	33
5	Feynman diagram representation of the three-nucleon two-pion exchange interaction. Solid and dashed lines denote respectively nucleons and pions. The dashed circle corresponds to the $\pi\pi NN$ vertex.	36
6	Feynman diagram representation of the three-nucleon exchange current operators. Solid, dashed and wavy lines denote respectively nucleons, pions and photons. The dashed circle corresponds to the $\pi\pi NN$ vertex.	37
7	Feynman diagram representation of the $NN \rightarrow N\Delta$ and $NN \rightarrow \Delta\Delta$ transition interactions due to one pion exchange. Solid, thick-solid, and dashed lines denote nucleons, Δ -isobars, and pions, respectively.	41
8	Transition correlation functions $u^{\sigma\tau II}(r)$, $u^{t\tau II}(r)$, etc. obtained for the AV28Q model [77], and perturbation theory equivalents $u^{\sigma\tau II,PT}(r)$, $u^{t\tau II,PT}(r)$, etc.	43
9	$N\Delta$ -transition two-body currents due to pion exchange.	46

10	Elastic scattering in one-photon exchange approximation. Solid, thick-solid and wavy lines denote respectively electrons, hadrons and photons.	56
11	Diagrammatic representation of operators included in $j(\Delta)$ due to one-body currents $j^{(1)}(N \rightarrow \Delta)$, $j^{(1)}(\Delta \rightarrow \Delta)$, etc., transition correlations $U^{N\Delta}$, $U^{\Delta\Delta}$, and corresponding Hermitian conjugates. Wavy, thin, thick, dashed and cross-dashed lines denote photons, nucleons, Δ -isobars and transition correlations $U^{BB'}$ and $U^{BB'\dagger}$, respectively.	62
12	Diagrammatic representation of operators included in $j(\Delta)$ due to two-body currents $j^{(2)}(NN \rightarrow N\Delta)$, $j^{(2)}(NN \rightarrow \Delta N)$, etc., transition correlations $U^{N\Delta}$, $U^{\Delta\Delta}$, and corresponding Hermitian conjugates. Wavy, thin, thick, dashed and cross-dashed lines denote photons, nucleons, Δ -isobars and transition correlations $U^{BB'}$ and $U^{BB'\dagger}$, respectively.	63
13	Diagrams associated with connected three-body terms, which are neglected in the present work. Wavy, thin, thick, dashed, cross-dashed and dotted lines denote photons, nucleons, Δ -isobars, transition correlations $U^{BB'}$ and $U^{BB'\dagger}$, and the two-body current $j^{(2)}(NN \rightarrow NN)$, respectively.	64
14	The magnetic form factors of ^3H and ^3He , obtained with single-nucleon currents (1-N), and with inclusion of two-nucleon current ((1+2)-N) and $\pi\pi_S$ three-nucleon (TOT-N(D)) current contributions, are compared with data (shaded area) from Amroun <i>et al.</i> [105]. Theoretical results correspond to the AV18/UIX PHH wave functions, and employ the dipole parametrization (including the Galster factor for $G_E(q_\mu^2)$) for the nucleon electromagnetic form factors. Note that the Sachs form factor $G_E^V(q_\mu^2)$ is used in the model-independent isovector two-body currents obtained from the charge-independent part of the AV18 interaction. Also shown are the total results corresponding to the Gari-Krümpelmann parametrization [106] of the nucleon electromagnetic form factor (TOT-N(GK)).	66

15	Individual contributions to the $F_M^S(q_\mu)$ and $F_M^V(q_\mu)$ combinations. Eq. (196), of the ^3H and ^3He magnetic form factors, obtained with the dipole parametrization of the nucleon electromagnetic form factors. The sign of each contribution is given in parenthesis. Note that, because of isospin-symmetry breaking components present in the ^3H and ^3He wave functions, the purely isovector PS, V and $\pi\pi_S$ currents (purely isoscalar $\rho\pi\gamma$ current) give non vanishing contributions to the $F_M^S(q_\mu)$ ($F_M^V(q_\mu)$) combination. However as the $\pi\pi_S$ ($\rho\pi\gamma$) contribution is very small, is not shown.	68
16	The $F_M^S(q_\mu)$ and $F_M^V(q_\mu)$ combinations of the ^3H and ^3He magnetic form factors, obtained with single-nucleon currents (1-N), and with inclusion of two-nucleon current ((1+2)-N) and $\pi\pi_S$ three-nucleon current (TOT-N) contributions, are compared with data (shaded area) from Amroun <i>et al.</i> [105]. The dipole parametrization is used for the nucleon electromagnetic form factors.	69
17	The charge form factors of ^3H and ^3He , obtained with a single-nucleon charge operator (1-N) and with inclusion of two-nucleon charge operator contributions (TOT-N), are compared with data (shaded area) from Amroun <i>et al.</i> [105]. Note that the 1-N results also include the Darwin-Foldy and spin-orbit corrections. Theoretical results correspond to the AV18/UIX PHH wave functions, and employ the dipole parametrization of the nucleon electromagnetic form factors.	70
18	Individual contributions to the $F_C^S(q_\mu)$ and $F_C^V(q_\mu)$ combinations. Eq. (200), of the ^3H and ^3He charge form factors, obtained with the dipole parametrization of the nucleon electromagnetic form factors. The sign of each combination is given in parenthesis. Note that, because of isospin-symmetry breaking components present in the ^3H and ^3He wave functions, the purely isovector $\omega\pi\gamma$ (isoscalar $\rho\pi\gamma$) charge operator gives a non vanishing contribution to the $F_C^S(q_\mu)$ ($F_C^V(q_\mu)$) combination.	71
19	The magnetic form factors of ^3H and ^3He , obtained with single-nucleon currents (1-N), and with inclusion of two- and three-nucleon current (TOT-N) and Δ (TOT-(N+ Δ)) contributions. . .	73
20	The single-nucleon contribution to the $F_M^S(q_\mu)$ and $F_M^V(q_\mu)$ combination of the ^3H and ^3He magnetic form factors is compared with the 1- Δ and 2- Δ contributions, associated respectively with diagrams of Fig. 11 and 12.	74
21	Kinematic and coordinate system for scattering of polarized electrons from a polarized target.	77

22	The longitudinal and transverse response functions of ${}^3\text{He}$, obtained with the AV18/UIX Hamiltonian model and one-body only (dashed lines) or both one- and two-body (solid lines) charge and current operators, are compared with the data of Ref. [111] at excitation energies below the ppn breakup threshold.	82
23	The longitudinal (R_L), longitudinal-transverse ($R_{LT'}$), transverse (R_T) and transverse-transverse ($R_{T'}$) response functions of ${}^3\text{He}$, obtained with the AV18/UIX Hamiltonian model and one-body only (thick dashed lines) or both one- and two-body (thick solid lines) charge and current operators, are displayed at a fixed excitation energy of 1 MeV for three-momentum transfers in the range 0–5 fm^{-1} . In R_L and $R_{LT'}$ we show the contributions associated with the (dominant) S-wave pd scattering states, while in R_T and $R_{T'}$ both S- and P-wave contributions are shown.	85
24	The inclusive cross section, and the $A_{LT'}$ and $A_{T'}$ asymmetries, obtained with the AV18/UIX Hamiltonian model and one-body only (dashed lines) or both one- and two-body (solid lines) charge and current operators, are displayed for ${}^3\text{He}$ at a fixed excitation energy of 1 MeV for three-momentum transfers in the range 0–5 fm^{-1} . The results in PWIA (dotted lines) are also shown. The incident electron energy is 4 GeV, and the electron scattering angle is in the range 0–14°.	86
25	The SSM solar neutrino energy spectrum. The continuum neutrino fluxes are given in $\text{cm}^{-2} \text{sec}^{-1} \text{MeV}^{-1}$, the lines in $\text{cm}^{-2} \text{sec}^{-1}$. . .	88
26	Schematic representation of the hep reaction.	90
27	Diagrammatic representation of the operators included in $O(\Delta)$, due to the one-body current and charge operators, to the transition correlations $U^{N\Delta}$ and $U^{\Delta\Delta}$ and the corresponding Hermitian conjugates. Thin, thick, dashed and cross-dashed lines denote, respectively, nucleons, Δ -isobars, and transition correlations $U^{BB'}$ and $U^{BB'\dagger}$	97
28	Electron energy spectrum for the ratio between the Super-Kamiokande 825-days data and the expectation based on unoscillated ${}^8\text{B}$ neutrinos [24]. The data are taken from Ref. [23]. The 5 curves from the bottom to the top correspond respectively to no hep contribution (dotted line), $\alpha=2.2$, 4.4, 10, 20, with α defined in Eq. (273).	109

Chapter 1

Introduction

In a non-relativistic approach to the study of the structure and dynamics of few-body nuclei, these are seen as systems of particles, the nucleons, interacting among themselves and, eventually, with external electroweak probes¹. Although based on a very simple and old idea, this approach has quite a remarkable success in describing many nuclear properties [1]. The first condition for such a success is the development of accurate models for the interaction among the nucleons in a nucleus. The nuclear Hamiltonian is written as sum of a non-relativistic kinetic energy term and two- and three-nucleon interactions. The main features of the nucleon-nucleon (NN) interaction are a long-range part due to one-pion-exchange (OPE), an intermediate-range attraction and a short-range repulsion. While the OPE long-range part is well known, the more complicated intermediate- and short-range components can be either modelled using heavy-meson-exchange mechanisms (like in the CD Bonn interaction [2]), or parametrized in terms of suitable functions and operators (like in the Argonne v_{18} (AV18) interaction [3]). The coupling constants and cutoff masses at the mesonic vertices in the first case, or the function parameters in the second case are then determined by fitting the large body of NN experimental data, not only deuteron properties, but also pp and np scattering data at laboratory energies below $\simeq 400$ MeV, where the scattering is predominantly elastic. The AV18 and CD Bonn interactions are

¹The journal model for this thesis is Physical Review C

able to describe the NN database with a χ^2 per datum of almost 1. A nuclear Hamiltonian which includes only two-nucleon interaction is however unable to reproduce the low-lying energy spectra of nuclei with $A \leq 8$ [4, 5]. A possible solution to this problem is to go beyond two-nucleon interactions and introduce three-nucleon interactions. A way of constructing these three-nucleon interactions makes them arise from the internal structure of the nucleon. The long-range part of the interaction can be obtained with the following mechanism: the exchanged pion between two nucleons excites one of them into its lowest excited state, the Δ -resonance. The Δ -resonance can then decay again into a nucleon, exchanging a pion with a third nucleon. In the Urbana-type models (for instance, the Urbana IX (UIX) [6]), the long-range part is given by this two-pion-exchange three-nucleon interaction, while the short-range part is constructed in a pure phenomenological way. The strengths of the long- and short-range components of the interaction are then fitted to reproduce the experimental values of the ${}^3\text{H}$ binding energy and nuclear matter equilibrium density. The full non-relativistic nuclear Hamiltonian AV18/UIX has then been found able to describe with good accuracy the low-lying energy spectra of systems with $A \leq 8$ [4, 5]. These models for the two- and three-nucleon interactions, their derivation and their explicit expressions, are briefly reviewed in Chapter 2.

The strong correlations between the nucleon spatial and internal degrees of freedom (spin and isospin) induced by the nuclear interaction make the solution of the Schrödinger equation a challenging task, even for the three- and four-body nuclei. However, the recent remarkable progress in both methods and computational facilities now allow us to make reliable calculations for ground and scattering states of light nuclei. We have considered in particular the so-called correlated hyperspherical harmonics (CHH) method [7, 8, 9, 10, 11]. The wave function is expanded on a basis of hyperspherical harmonic functions, multiplied by appropriate correlation factors, which are introduced to account for the correlations induced by the NN interaction. Appropriate variational principles are then applied to obtain the unknown coefficients of the expansion. Although variational, and in principle limited by the maximum number of basis functions included in the

expansion, the CHH method has achieved high accuracy in describing the three- and four-body bound and scattering states. We review the method in Chapter 3.

The approach described so far would be interesting, but of rather limited utility, if it could be tested only comparing the theoretical and experimental binding energies of few-body nuclei. In fact, many experimental results are available over a wide range of energies, from the few keV of astrophysical interest to the hundreds of MeV measured in electron-scattering experiments. Since in these processes nuclei interact with external electroweak probes, it is necessary to develop realistic models for the nuclear current and charge operators. In fact, the construction of such models has proven to be essential in the study of low-energy electroweak processes [1]. In our model, the nuclear transition operator consists of one- and many-body components. The one-body term, the so-called “impulse approximation”, arises in the simplest picture in which the electroweak probe interacts with the individual protons and neutrons inside the nucleus. This is, however, certainly incomplete: as discussed above, the nuclear interaction is mediated, at long-range, by pion-exchange and seems to be rather well reproduced even at intermediate- and short-range by heavy-meson exchanges. These exchanged particles can themselves interact with the external electroweak probe, and this leads to the introduction of many-body currents. In the electromagnetic case, the leading two-body terms of the current operator are required by gauge invariance, and can be linked to the model of the NN interaction by the continuity equation. Constructing these terms to explicitly satisfy current conservation with the given NN interaction leaves no free parameters in their expressions. In the weak case, instead, the axial current operator is not conserved and, as such, is inherently model dependent. This model dependence of its many-body components can be reduced by constraining them to reproduce measured weak transitions, for example by fitting the Gamow-Teller matrix element in tritium β -decay [12]. Finally, an important aspect of the current is that the external electroweak probe can excite the internal degrees of freedom of the nucleon, specifically its lowest excitation, the Δ -resonance. Our approach has been extended to include these additional contributions arising from Δ -excitation [13, 14], consistently with the model for

the long-range part of the three-nucleon interaction. These Δ -contributions have been found rather small in the electromagnetic case [13], but very important in weak processes [12, 14]. The model for the nuclear transition operator is reviewed in Chapter 4.

Within this approach, we have investigated three processes: elastic electron-scattering from ^3H and ^3He [13], electrodisintegration of ^3He at threshold [15], and $p\ ^3\text{He}$ weak capture reaction [14, 16]. For the first process, there is a large body of experimental results, and a thorough comparison between theory and experiment can highlight what, in our approach, needs to be improved and refined. We have calculated the trinucleon form factors on a wide range of momentum transfer q (from 0 up to 7 fm^{-1}), and static properties like magnetic moments, and magnetic and charge radii. While the ^3H and ^3He charge form factors and static properties, and the ^3H magnetic form factor are quite well reproduced, our calculation fails to predict the ^3He magnetic form factor in the first diffraction region ($q \geq 3 - 4\text{ fm}^{-1}$). This discrepancy persists even in the more refined picture of the nucleus, where Δ -isobar degrees of freedom are included. This has led, on the theoretical side, to speculations about the need of a more refined model for the three-nucleon interaction, and, on the experimental side, to plan for new more accurate measurements of the ^3He magnetic form factor at $q \geq 3\text{ fm}^{-1}$ [17]. These results for the trinucleon elastic form factors are presented in Chapter 5, together with definitions for the observables of interest and details of the calculation.

A comparison between theory and experiment can also be performed in the case of the threshold electrodisintegration of ^3He [15], although here the available experimental results have rather large errors. Generally, good agreement has been found between measured and calculated observables, when both one- and two-body contributions are included in the electromagnetic charge and current operators. Indeed, the calculation in impulse approximation fails completely to reproduce the experimental results, further reemphasizing the importance of including many-body contributions in the transition operators. We review this calculation in Chapter 6.

Unlike the above processes, there are no direct experimental results for the $p^3\text{He}$ weak capture reaction, known also as the *hep* reaction—the *hep* cross section is too small to be measured experimentally. However, there has been recently a revival of interest in this process [18, 19, 20, 21, 22], spurred by the Super-Kamiokande (SK) measurement of the energy spectrum of electrons recoiling from scattering with solar neutrinos [23]. Over most of the spectrum, a suppression $\simeq 0.5$ is observed relative to the standard-solar-model (SSM) predictions [24]. Above 14 MeV, however, there is an apparent excess of events. The *hep* process is the only source of solar neutrinos with energies larger than about 15 MeV—their end-point energy is about 19 MeV. The discrepancies between the measured spectrum and SSM predictions have led to question the reliability of the calculations from which the SSM derives its *hep* neutrino flux estimate [25]. The calculation of the *hep* reaction is rather delicate, since the S-wave capture induced by the one-body axial current is suppressed, and consequently many-body axial currents and P-wave contributions are highly enhanced. Within the approach described so-far, we have performed a calculation of the *hep* reaction, using accurate CHH wave functions, obtained from the AV18/UIX Hamiltonian model, and including all possible transitions between the S- and P-wave initial state capture channels and the ^4He final state. The chief conclusion of this study [14, 16] is that the *hep* reaction cross section is enhanced by a factor of $\simeq 4.5$ respect to the SSM prediction, and 40 % of the total calculated value arises from the P-wave contributions, which were neglected, or at least not sufficiently appreciated, in previous studies [21, 25]. The main aspects of this calculation, together with a discussion of the results and their implications, are given in Chapter 7. Conclusions and final remarks are given in Chapter 8.

Chapter 2

The Nuclear Interaction

In the simplest picture, the nucleus is considered as a system of interacting neutrons and protons. In a non-relativistic framework, the Hamiltonian is given by:

$$H = \sum_i \frac{\mathbf{p}_i^2}{2m} + \sum_{i < j} v_{ij} + \sum_{i < j < k} V_{ijk} + \cdots \quad (1)$$

where the nucleons interact via two-, three-, and possibly many-body interactions. In this Chapter we briefly describe some of the dominant features of the two- and three-nucleon potential models, focusing on the Argonne v_{14} [26] and v_{18} [3] two-nucleon and Urbana VIII [27] and IX [6] three-nucleon interactions.

2.1 Two-Nucleon Interactions

The two-nucleon (NN) interaction has an extraordinarily rich structure, as has been recognized for quite a long time. It is described in terms of the nucleon's spin ($\frac{1}{2}\boldsymbol{\sigma}$) and isospin ($\frac{1}{2}\boldsymbol{\tau}$), where both $\boldsymbol{\sigma}$ and $\boldsymbol{\tau}$ are Pauli matrices. The former variable represents the intrinsic angular momentum (spin) of the nucleon, while the latter is a convenient representation for its two charge states—the proton and neutron. The generalized Pauli principle in this framework requires that two-nucleon states be antisymmetric with respect to the simultaneous exchange of the nucleons' space, spin, and isospin coordinates. The main part of the NN interaction is isospin-conserving and can be written as linear combinations of

components proportional to the two isoscalars, 1 and $\boldsymbol{\tau}_i \cdot \boldsymbol{\tau}_j$. However, isospin-symmetry-breaking terms are also present in the NN interaction: in fact, they are necessary to reproduce with good accuracy simultaneously both pp and np low-energy scattering data. We will return to this point later.

It is well known that the long-range component of the NN interaction is due to one-pion-exchange (OPE). If isospin-symmetry-breaking terms are ignored, it is given, at long distances, by:

$$v_{ij}^{\text{OPE}} = \frac{f_{\pi NN}^2}{4\pi} \frac{m_\pi}{3} \left[Y_\pi(r_{ij}) \boldsymbol{\sigma}_i \cdot \boldsymbol{\sigma}_j + T_\pi(r_{ij}) S_{ij} \right] \boldsymbol{\tau}_i \cdot \boldsymbol{\tau}_j, \quad (2)$$

$$Y_\pi(r_{ij}) = \frac{e^{-m_\pi r_{ij}}}{m_\pi r_{ij}} \quad (3)$$

$$T_\pi(r_{ij}) = \left[1 + \frac{3}{m_\pi r_{ij}} + \frac{3}{(m_\pi r_{ij})^2} \right] \frac{e^{-m_\pi r_{ij}}}{m_\pi r_{ij}}, \quad (4)$$

where m_π is the mass of the exchanged pion, $f_{\pi NN}$ is the πNN coupling constant and

$$S_{ij} \equiv 3 \boldsymbol{\sigma}_i \cdot \hat{\mathbf{r}}_{ij} \boldsymbol{\sigma}_j \cdot \hat{\mathbf{r}}_{ij} - \boldsymbol{\sigma}_i \cdot \boldsymbol{\sigma}_j \quad (5)$$

is the tensor operator, $\hat{\mathbf{r}}_{ij}$ being the relative distance between particles i and j . At distances comparable to the inverse pion mass ($1/m_\pi \approx 1.4$ fm), OPE leads to a large tensor component in the NN interaction. In nuclear systems, then, the spatial and spin degrees of freedom are strongly correlated, and hence nuclear few- and many-body problems can be quite different from systems where the dominant interaction is independent of the particles internal quantum numbers (spin and isospin), such as the Coulomb interaction in atomic and molecular problems.

At moderate and short distances, the NN interaction is much more complicated. In this region, heavy-meson-exchanges and/or subnucleonic degrees of freedom all play a role, and the interaction models can be quite different, ranging from one-boson-exchange (OBE) models to models with explicit two-pion-exchanges (TPE) to purely phenomenological parametrizations. The models are then fit to reproduce the available NN experimental data. The Argonne v_{14} [26] interaction model (AV14), in particular, falls in the last category of purely phenomenological

parametrization and is parametrized as:

$$v_{ij}(r) = \sum_p [v_p^{\text{OPE}}(r) + v_p^I(r) + v_p^S(r)] O_{ij}^p, \quad (6)$$

where O_{ij}^p is the set of 14 operators given by

$$O_{ij}^p = [1, \boldsymbol{\sigma}_i \cdot \boldsymbol{\sigma}_j, S_{ij}, (\mathbf{L} \cdot \mathbf{S})_{ij}, \mathbf{L}_{ij}^2, \mathbf{L}_{ij}^2 \boldsymbol{\sigma}_i \cdot \boldsymbol{\sigma}_j, (\mathbf{L} \cdot \mathbf{S})_{ij}^2] \otimes [1, \boldsymbol{\tau}_i \cdot \boldsymbol{\tau}_j] \quad (7)$$

Here \mathbf{L} is the relative orbital angular momentum and \mathbf{S} the spin of the pair. The first eight of these operators (those not involving two powers of the momentum) are unique, in the sense that all such operators are implicitly contained in any realistic NN interaction model. The primary motivation for the choice of the higher-order terms is convenience in few- and many-body calculations: for example, the \mathbf{L}^2 terms do not contribute in relative S-waves. This set of 14 operators provide sufficient freedom to fit the phase-shift and mixing angle parameters of the 14 singlet and triplet relative S-, P-, D- and F-waves.

The three radial functions of Eq. (6) are the long-range OPE part and the intermediate- and short-range parts $v_p^I(r)$ and $v_p^S(r)$. The $v_p^{\text{OPE}}(r)$ function contributes only for the operators

$$[\boldsymbol{\sigma}_i \cdot \boldsymbol{\sigma}_j, S_{ij}] \otimes \boldsymbol{\tau}_i \cdot \boldsymbol{\tau}_j \quad (8)$$

as discussed above, and it is given by Eqs. (2)-(4), where Y_π and T_π are calculated using $f_{\pi NN}^2/4\pi = 0.081$ (for the AV14) and are multiplied by smooth Gaussian cutoffs that make them vanish at $r = 0$. The $v_p^I(r)$ are parametrized as functions proportional to T_π^2 , defined in Eqs. (2)-(4), and consequently of two-pion-exchange range. The $v_p^S(r)$ are short-range Woods-Saxon functions. The parameters of the Woods-Saxon functions, as well as the coefficient for $v_p^I(r)$, are adjusted to reproduce the deuteron properties and np scattering data up to 400 MeV.

Before the early nineties, all the different NN interaction models, the AV14 as well as the available models based on OBE or TPE mechanisms, produced a qualitatively similar picture of the NN interaction, consisting of OPE at long range, an intermediate-range attraction and a short-range repulsion. However,

quantitatively, all these models were somewhat different. There were several reasons for this, chief among them was that they were in fact not all fit to the same data set. For example, models fit to np data, like the AV14, did not precisely fit the experimental pp data if only electromagnetic corrections were introduced.

When in the early nineties high quality phase shift analyses of the pp and np data became available from the Nijmegen and VPI groups [28, 29, 30, 31, 32, 33, 34], several new NN interaction models were constructed to reproduce this improved experimental database. As most important consequence, all the new generation NN interaction models which are still in use today give a quantitatively similar picture of the NN interaction.

Among these new models, the Argonne v_{18} (AV18) interaction [3] follows basically along the lines of its predecessor, the AV14. In fact, it can be expressed as the sum of a charge-independent (CI) and a charge-symmetry-breaking (CSB) part. The former has the same 14 operators components of the AV14, although there are some differences: (i) the charged and neutral pion mass splitting is taken into account; (ii) the Nijmegen partial-wave analysis has found very little difference between the coupling constants $f_{\pi^0 NN}$ and $f_{\pi^\pm NN}$, and therefore $f_{\pi NN}$ is chosen to be charge-independent; its value ($f_{\pi NN}^2/4\pi=0.075$) is somewhat smaller than in the AV14; (iii) the electromagnetic interaction, specified along with the strong interaction, and treated up to order α^2 , α being the fine structure constant, consists of one- and two-photon Coulomb terms, Darwin-Foldy and vacuum polarization contributions, and magnetic moment interactions [35].

The CSB term has three charge-dependent and one charge-asymmetric operators: these four operators are the minimal requirement in order to provide a precise fit of the np and pp database simultaneously. They are given by:

$$O_{ij}^{p=15\dots18} = T_{ij} \cdot \boldsymbol{\sigma}_i \cdot \boldsymbol{\sigma}_j T_{ij} \cdot S_{ij} T_{ij} \cdot (\tau_{i,z} + \tau_{j,z}) \quad (9)$$

where the isotensor operator is defined as

$$T_{ij} = 3\tau_{i,z}\tau_{j,z} - \boldsymbol{\tau}_i \cdot \boldsymbol{\tau}_j \quad (10)$$

With a total of 40 adjustable parameters, the AV18 interaction is able to reproduce the NN database with a χ^2 per degree of freedom near one. Note that this large

number of parameters is a feature common to all the interaction models of the past decade.

2.2 Three-Nucleon Interactions

All the two-nucleon interactions which contain non-localities only at the level of two powers of the relative momentum (\mathbf{p}^2 or \mathbf{L}^2), as in the case of the AV14 and AV18, have been found to yield nearly identical results for the triton binding energy, 7.62 ± 0.01 MeV as compared to the experimental value of 8.48 MeV [36]. Furthermore, the equilibrium density of nuclear matter is overpredicted. One way to solve this discrepancy is to include three-nucleon interactions in the nuclear Hamiltonian.

A simple model for the three-nucleon interactions makes them arise from the internal structure of the nucleon. Since all degrees of freedom other than the nucleons have been integrated out, the presence of nuclear resonances, such as the Δ -resonance, induces three-body forces. The long-range term involving the intermediate excitation of a Δ -isobar, via pion exchanges, is illustrated in Fig. 1. The two-pion-exchange three-nucleon interaction (2π TNI) was originally written down by Fujita and Miyazawa [37]:

$$V_{ijk}^{2\pi} = A_{2\pi} \left[\{X_{ij} \cdot X_{ik}\} \{\boldsymbol{\tau}_i \cdot \boldsymbol{\tau}_j, \boldsymbol{\tau}_i \cdot \boldsymbol{\tau}_k\} + \frac{1}{4} [X_{ij} \cdot X_{ik}] [\boldsymbol{\tau}_i \cdot \boldsymbol{\tau}_j, \boldsymbol{\tau}_i \cdot \boldsymbol{\tau}_k] \right] . \quad (11)$$

where

$$A_{2\pi} = \left(\frac{f_{\pi N \Delta}}{m_\pi} \right)^2 \left(\frac{f_{\pi N N}}{m_\pi} \right)^2 \frac{1}{m - m_\Delta} . \quad (12)$$

$$X_{ij} = Y_\pi(r_{ij}) \boldsymbol{\sigma}_i \cdot \boldsymbol{\sigma}_j + T_\pi(r_{ij}) S_{ij} . \quad (13)$$

$f_{\pi N \Delta}$, m , and m_Δ are respectively the $\pi N \Delta$ coupling constant, the nucleon and the Δ masses and $\{\dots\}$ ($[\dots]$) denote the anticommutators (commutators). This interaction has been found to be attractive in light nuclei.

The Urbana models for the three-nucleon interactions, the older Urbana VIII [27] (UVIII) and the more recent Urbana IX [6] (UIX), are written as the sum of the 2π TNI plus a phenomenological shorter-range term of the form:

$$V_{ijk}^R = U_0 T_\pi^2(r_{ij}) T_\pi^2(r_{ik}) \quad . \quad (14)$$

This term is of two-pion-exchange range on each of the two legs, and is meant to simulate the dispersive effects which are required when integrating out Δ -isobar degrees of freedom. This phenomenological short-range term is repulsive, and is here taken to be independent of spin and isospin.

The constants $A_{2\pi}$ and U_0 in Eqs. (11) and (14) are adjusted to reproduce the triton binding energy in “exact” Green’s function Monte Carlo (GFMC) calculations [4], and the nuclear matter equilibrium density in variational calculations based on operator-chain expansion [38]. Recent GFMC calculations based on the AV18/UIX Hamiltonian model have been shown to provide a reasonable description of the low-energy spectra and charge radii of nuclei with $A \leq 8$ [4, 5].

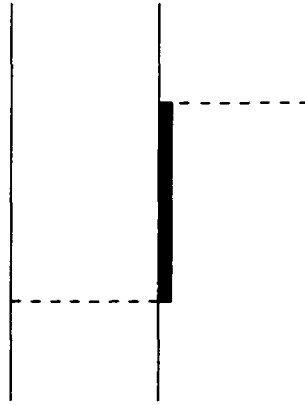


FIG. 1: The Fujita and Miyazawa two-pion-exchange three-nucleon interaction diagram. Thin, thick, and dashed lines denote, respectively, nucleons, Δ -isobars and pions.

Chapter 3

Bound- and Scattering-State Wave Functions

Given a model for the nuclear Hamiltonian, the next step consists in obtaining the nuclear bound and scattering states, and in comparing the calculated observables with the available experimental data. Although the nuclear interaction models described in the previous Chapter are quite simple to write down, the solution of the Schrödinger equation, even for the three- and four-nucleon systems, is a very challenging task. This is mainly due to the strong correlation between the spatial and internal degrees of freedom (spin and isospin) of the nucleons present in these interactions.

Several techniques have been developed through the years to solve this problem and intense effort continues to go on for their implementation. For the three-nucleon system, there is a long history of numerical methods: one of the most established one is the Faddeev method. The basic idea of this technique is to rewrite the Schrödinger equation as a sum of three equations in which (for two-nucleon interactions at least) only one pair interacts at a time. The resulting equations are solved in either momentum- or coordinate-space. The Faddeev (and Faddeev-Yakubovsky) methods have been applied to solve the bound as well as the scattering states of three- and, recently, four-nucleon systems [39, 40, 41]. While these techniques are in principle “exact”, their implementation, particularly

in momentum-space, is difficult when the Coulomb interaction is present, such as, for example, in the pd and $p^3\text{He}$ scattering channels. In fact, at this point in time, we are not aware of any Faddeev calculation for the $p^3\text{He}$ scattering problem.

Techniques based on quantum Monte Carlo methods have been also developed to solve the problem of few-body nuclei, with mass number $A \leq 8$ [4, 5], and are currently being extended to treat systems with $A = 9$. These are the variational Monte Carlo (VMC) and the Green's function Monte Carlo (GFMC) techniques. The VMC is an approximate variational method that uses Monte Carlo techniques to perform the spatial integrations. The GFMC method, on the other hand, employs Monte Carlo techniques to evaluate the imaginary-time path integrals relevant for a light nucleus. It typically uses the VMC wave functions as a starting point, and cools them in order to measure ground-state observables.

More recently, the few-body systems with $A \leq 4$ have also been studied with a variational technique known as the correlated-hyperspherical-harmonics (CHH) method, developed by Kievsky, Viviani, and Rosati [7, 8, 9, 10, 11, 15, 42, 43, 44, 45, 46, 47]. This method consists in expanding the wave function over a basis of hyperspherical harmonic functions multiplied by correlation factors. Although variational and in principle limited by the maximum number of basis functions kept in the expansion, this technique has achieved high accuracy in describing the three- and four-body bound and scattering states. In fact, we have used this method to calculate the ^3H , ^3He and ^4He wave functions and the pd and $p^3\text{He}$ scattering-state wave functions at energies below deuteron and ^3He breakup thresholds, respectively.

This Chapter is divided into two Sections: in Section 3.1 we review the CHH method for the bound state problem, while in Section 3.2 we describe the CHH method for the scattering problem.

3.1 The Bound-State Wave Functions

In this Section, we describe the main features of the CHH method, when applied to calculate the trinucleon wave functions in Subsection 3.1.1, and the α -particle

wave function in Subsection 3.1.2.

3.1.1 The Three-Nucleon Wave Function

The wave function Ψ of a three-nucleon system with total angular momentum JJ_z and total isospin TT_z can be decomposed as

$$\Psi = \sum_{i=1}^3 \psi(\mathbf{x}_i, \mathbf{y}_i) . \quad (15)$$

where the amplitude $\psi(\mathbf{x}_i, \mathbf{y}_i)$ is a function of the Jacobi coordinates $\mathbf{x}_i = \mathbf{r}_j - \mathbf{r}_k$ and $\mathbf{y}_i = (\mathbf{r}_j + \mathbf{r}_k - 2\mathbf{r}_i) / \sqrt{3}$, i, j, k being a cyclic permutation of 1,2,3. To ensure the overall antisymmetry of Ψ , the amplitude $\psi(\mathbf{x}_i, \mathbf{y}_i)$ is antisymmetric with respect to exchange of nucleons j and k , and is expressed as [8, 9]

$$\psi(\mathbf{x}_i, \mathbf{y}_i) = \sum_{\alpha} F_{\alpha} \Phi_{\alpha}(x_i, y_i) \mathcal{Y}_{\alpha}(j, k; i) . \quad (16)$$

$$\mathcal{Y}_{\alpha}(j, k; i) = \left\{ \left[Y_{\ell_{\alpha}}(\hat{\mathbf{x}}_i) \otimes Y_{L_{\alpha}}(\hat{\mathbf{y}}_i) \right]_{\Lambda_{\alpha}} \otimes \left[S_{\alpha}^{jk} \otimes s^i \right]_{S_{\alpha}} \right\}_{JJ_z} \left[T_{\alpha}^{jk} \otimes t^i \right]_{TT_z} . \quad (17)$$

where each channel α is specified by the orbital angular momenta ℓ_{α} , L_{α} and Λ_{α} , the spin (isospin) S_{α}^{jk} (T_{α}^{jk}) of pair jk and the total spin S_{α} . Orbital and spin angular momenta are coupled, in the LS -coupling scheme, to give total angular momenta JJ_z . The correlation factor F_{α} takes into account the strong state dependent correlations induced by the NN interaction. Two different forms have been employed for F_{α} :

$$F_{\alpha} = f_{\alpha}(r_{jk}) \equiv f_{\alpha}(x_i) , \quad (18)$$

$$F_{\alpha} = f_{\alpha}(r_{jk}) g_{\alpha}(r_{ij}) g_{\alpha}(r_{ik}) . \quad (19)$$

In the first case, the wave function includes correlation effects only between nucleons j and k in the active pair, while in the second case, the wave function includes in addition correlation effects between these and the spectator nucleon i . Traditionally, the method is known as pair-correlated hyperspherical harmonics (PHH) method when the first choice of the correlation factor is employed. For

realistic soft-core potentials, like the AV14 or AV18, the convergence pattern with respect to the number of basis functions appears to be somewhat faster in the PHH expansion than in the CHH one. This is not true in the case of the α -particle. Therefore, we have used the PHH expansion to solve the three-body problem and the CHH one in the study of the α -particle.

The (channel-dependent) correlation functions $f_\alpha(r_{jk})$ are obtained with the following procedure: when two of the nucleons are close to each other and far removed from the others, it is expected that their wave function will be predominantly influenced by their mutual interaction. The radial wave function for two particles in state $\beta = j_\beta l_\beta S_\beta^k T_\beta^k$ is then obtained from solutions of two-body Schrödinger-like equations

$$\sum_{\beta'} [T_{\beta,\beta'}(r) + v_{\beta,\beta'}(r) + \lambda_{\beta,\beta'}(r)] f_{\beta'}(r) = 0 . \quad (20)$$

$T_{\beta,\beta'}$ and $v_{\beta,\beta'}$ are the kinetic and potential energy operators.

$$T_{\beta,\beta'} = \frac{\hbar^2}{m} \left[\frac{\partial^2}{\partial r^2} + \frac{2}{r} \frac{\partial}{\partial r} - \frac{l_\beta(l_\beta + 1)}{r^2} \right] \delta_{\beta,\beta'} . \quad (21)$$

$$v_{\beta,\beta'} = \langle \beta | v_{jk} | \beta' \rangle \quad (22)$$

and v_{jk} is the NN interaction. The term $\lambda_{\beta,\beta'}(r)$ in Eq. (20) simulates the effect of the interaction of the active pair with the remaining particles in the system and is chosen to be of the simple form

$$\lambda_{\beta,\beta'}(r) = \lambda_\beta^0 e^{-\gamma r} \delta_{\beta,\beta'} , \quad (23)$$

where λ_β^0 and γ are two parameters that allow $f_\beta(r)$ to satisfy appropriate boundary conditions. For more details, see Refs. [7, 8].

Next, we introduce the hyperspherical coordinates ρ and ϕ_i , defined as

$$\rho = \sqrt{x_i^2 + y_i^2} , \quad \cos \phi_i = x_i / \rho . \quad (24)$$

Note that the hyper-radius ρ is independent on the permutation i considered. The dependence of $\Phi_\alpha(x_i, y_i)$ on ρ and ϕ_i is then made explicit by writing

$$\Phi_\alpha(x_i, y_i) = \sum_{n=0}^{M_\alpha} \frac{u_n^\alpha(\rho)}{\rho^{5/2}} Z_n^\alpha(\phi_i) , \quad (25)$$

$$Z_n^\alpha(\phi_i) = N_n^{\ell_\alpha, L_\alpha} (\cos \phi_i)^{\ell_\alpha} (\sin \phi_i)^{L_\alpha} P_n^{\ell_\alpha + \frac{1}{2}, L_\alpha + \frac{1}{2}}(\cos 2\phi_i) . \quad (26)$$

where $N_n^{\ell_\alpha, L_\alpha}$ are normalization factors, $P_n^{\alpha, \beta}$ are Jacobi polynomials and n is a non-negative integer, $n = 0, \dots, M_\alpha$, M_α being the selected number of basis functions in channel α . The complete wave function is then written as

$$\Psi = \sum_{ijk \text{ cyclic}} \sum_{\alpha} f_{\alpha}(x_i) \mathcal{Y}_{\alpha}(j, k; i) \sum_{n=0}^{M_{\alpha}} \frac{u_n^{\alpha}(\rho)}{\rho^{5/2}} Z_n^{\alpha}(\phi_i) . \quad (27)$$

The Rayleigh-Ritz variational principle,

$$\langle \delta_u \Psi | H - E | \Psi \rangle = 0 . \quad (28)$$

is used to determine the hyper-radial functions $u_n^{\alpha}(\rho)$ in Eq. (27). Carrying out the variation $\delta_u \Psi$ with respect to the functions $u_n^{\alpha}(\rho)$, the following equation is easily derived:

$$\sum_{ijk \text{ cyclic}} \langle f_{\alpha}(x_i) \mathcal{Y}_{\alpha}(j, k; i) Z_n^{\alpha}(\phi_i) | H - E | \Psi \rangle |_{\Omega} = 0 . \quad (29)$$

where Ω denotes the angular variables ϕ_i , $\hat{\mathbf{x}}_i$ and $\hat{\mathbf{y}}_i$. Performing the integration over Ω and spin-isospin sums (as implicitly understood by the notation $\langle \dots \rangle |_{\Omega}$) leads to a set of coupled second order differential equations for the $u_n^{\alpha}(\rho)$, which is then solved by standard numerical techniques [7, 8].

The binding energies in MeV of the $A=3$ nuclei obtained with the PHH method from the AV14, AV18, AV14/UIVIII and AV18/UIX Hamiltonians are listed in Table I [9]. Also listed in Table I are results calculated with converged configuration-space [40] and momentum-space [41] Faddeev wave functions for the AV14, and with the GFMC method [4] for the AV18/UIX potential model. The binding energies obtained with the various methods are in excellent agreement with each other, typically within 10 keV or less.

3.1.2 The ^4He Wave Function

The CHH approach has also been applied to the four-nucleon problem [10, 11, 46]. When studying the ^4He nucleus, it is convenient to consider the two sets of

TABLE I: Trinucleons binding energies in MeV corresponding to the AV14, AV18, AV14/UVIII and AV18/UIX Hamiltonian models. The PHH results for the AV14 potential are compared with those calculated by solving the Faddeev equations in configuration- (F/R) and in momentum-space (F/P). Also we compare the PHH and the GFMC results when the AV18/UIX potential model is used. The GFMC statistical errors are shown in parenthesis.

Model	Method	B(^3H)	B(^3He)
AV14	PHH	7.683	7.032
	F/R	7.670	7.014
	F/P	7.680	-
AV18	PHH	7.640	6.930
AV14/UVIII	PHH	8.47	7.73
AV18/UIX	PHH	8.49	7.75
	GFMC	8.47(1)	7.71(1)
expt.		8.48	7.72

Jacobi coordinates, which correspond to the partitions 1+3 and 2+2. The Jacobi variables corresponding to the partition 1+3 are defined as

$$\mathbf{x}_{Ap} = \mathbf{r}_j - \mathbf{r}_i . \quad (30)$$

$$\mathbf{y}_{Ap} = \sqrt{4/3}(\mathbf{r}_k - \mathbf{R}_{ij}) . \quad (31)$$

$$\mathbf{z}_{Ap} = \sqrt{3/2}(\mathbf{r}_l - \mathbf{R}_{ijk}) . \quad (32)$$

while those corresponding to the partition 2+2 are defined as

$$\mathbf{x}_{Bp} = \mathbf{r}_j - \mathbf{r}_i . \quad (33)$$

$$\mathbf{y}_{Bp} = \sqrt{2}(\mathbf{R}_{kl} - \mathbf{R}_{ij}) . \quad (34)$$

$$\mathbf{z}_{Bp} = \mathbf{r}_l - \mathbf{r}_k . \quad (35)$$

where \mathbf{R}_{ij} (\mathbf{R}_{kl}) and \mathbf{R}_{ijk} denote the center-of-mass positions of particles ij (kl) and ijk , respectively. The wave function Ψ is then expanded as

$$\Psi = \sum_p \left[\psi_A(\mathbf{x}_{Ap}, \mathbf{y}_{Ap}, \mathbf{z}_{Ap}) + \psi_B(\mathbf{x}_{Bp}, \mathbf{y}_{Bp}, \mathbf{z}_{Bp}) \right] , \quad (36)$$

where the index p runs over the even permutations of particles $ijkl$.

The procedure is similar to the one used for the three-nucleon problem and the amplitudes ψ_A and ψ_B are expanded as

$$\psi_A(\mathbf{x}_{Ap}, \mathbf{y}_{Ap}, \mathbf{z}_{Ap}) = \sum_{\alpha} F_{\alpha,p} \phi_{\alpha}^A(x_{Ap}, y_{Ap}, z_{Ap}) Y_{\alpha,p}^A, \quad (37)$$

$$\psi_B(\mathbf{x}_{Bp}, \mathbf{y}_{Bp}, \mathbf{z}_{Bp}) = \sum_{\alpha} F_{\alpha,p} \phi_{\alpha}^B(x_{Bp}, y_{Bp}, z_{Bp}) Y_{\alpha,p}^B, \quad (38)$$

where

$$\begin{aligned} Y_{\alpha,p}^A &= \left\{ \left[[Y_{\ell_{1\alpha}}(\hat{\mathbf{z}}_{Ap}) Y_{\ell_{2\alpha}}(\hat{\mathbf{y}}_{Ap})]_{\ell_{12\alpha}} Y_{\ell_{3\alpha}}(\hat{\mathbf{x}}_{Ap}) \right]_{L_{\alpha}} \left[[[s_i s_j]_{S_{a\alpha}} s_k]_{S_{b\alpha}} s_l \right]_{S_{\alpha}} \right\}_{JJ_z} \\ &\times \left[[[t_i t_j]_{T_{a\alpha}} t_k]_{T_{b\alpha}} t_l \right]_{TT_z}. \end{aligned} \quad (39)$$

$$\begin{aligned} Y_{\alpha,p}^B &= \left\{ \left[[Y_{\ell_{1\alpha}}(\hat{\mathbf{z}}_{Bp}) Y_{\ell_{2\alpha}}(\hat{\mathbf{y}}_{Bp})]_{\ell_{12\alpha}} Y_{\ell_{3\alpha}}(\hat{\mathbf{x}}_{Bp}) \right]_{L_{\alpha}} \left[[s_i s_j]_{S_{a\alpha}} [s_k s_l]_{S_{b\alpha}} \right]_{S_{\alpha}} \right\}_{JJ_z} \\ &\times \left[[t_i t_j]_{T_{a\alpha}} [t_k t_l]_{T_{b\alpha}} \right]_{TT_z}. \end{aligned} \quad (40)$$

Here a channel α is specified by: orbital angular momenta $\ell_{1\alpha}$, $\ell_{2\alpha}$, $\ell_{3\alpha}$, $\ell_{12\alpha}$, and L_{α} ; spin angular momenta $S_{a\alpha}$, $S_{b\alpha}$, and S_{α} ; isospins $T_{a\alpha}$ and $T_{b\alpha}$. The total orbital and spin angular momenta and cluster isospins are then coupled to the assigned JJ_z and TT_z . The overall antisymmetry of the wave function Ψ is ensured by requiring that both ψ_A and ψ_B change sign under the exchange $i \rightleftharpoons j$.

The correlation factors $F_{\alpha,p}$ is written, similarly to Eq. (19), as product of correlation functions, that are obtained from solutions of two-body Schrödinger-like equations, as discussed in the previous Subsection and, in more details, in Ref. [10].

The radial amplitudes ϕ_{α}^A and ϕ_{α}^B are further expanded as

$$\phi_{\alpha}^A(x_{Ap}, y_{Ap}, z_{Ap}) = \sum_{n,m} \frac{u_{nm}^{\alpha}(\rho)}{\rho^4} z_{Ap}^{\ell_{1\alpha}} y_{Ap}^{\ell_{2\alpha}} x_{Ap}^{\ell_{3\alpha}} X_{nm}^{\alpha}(\phi_{2p}^A, \phi_{3p}) . \quad (41)$$

$$\phi_{\alpha}^B(x_{Bp}, y_{Bp}, z_{Bp}) = \sum_{n,m} \frac{u_{nm}^{\alpha}(\rho)}{\rho^4} z_{Bp}^{\ell_{1\alpha}} y_{Bp}^{\ell_{2\alpha}} x_{Bp}^{\ell_{3\alpha}} X_{nm}^{\alpha}(\phi_{2p}^B, \phi_{3p}) , \quad (42)$$

where the magnitudes of the Jacobi variables have been replaced by the hyper-spherical coordinates, which in the four-body case are given by:

$$\rho = \sqrt{x_{Ap}^2 + y_{Ap}^2 + z_{Ap}^2} = \sqrt{x_{Bp}^2 + y_{Bp}^2 + z_{Bp}^2} , \quad (43)$$

$$\cos \phi_{3p} = x_{Ap}/\rho = x_{Bp}/\rho . \quad (44)$$

$$\cos \phi_{2p}^A = y_{Ap}/(\rho \sin \phi_{3p}) . \quad (45)$$

$$\cos \phi_{2p}^B = y_{Bp}/(\rho \sin \phi_{3p}) . \quad (46)$$

As in the three-body case, the hyper-radius is independent of the permutation p considered.

Finally, the hyper-angle functions X_{nm}^α consist of the product of Jacobi polynomials

$$X_{nm}^\alpha(\beta, \gamma) = N_{nm}^\alpha (\sin \beta)^{2m} P_n^{K_{2\alpha}, \ell_{3\alpha} + \frac{1}{2}}(\cos 2\beta) P_m^{\ell_{1\alpha} + \frac{1}{2}, \ell_{2\alpha} + \frac{1}{2}}(\cos 2\gamma) , \quad (47)$$

where the indices m and n run, in principle, over all non-negative integers, $K_{2\alpha} = \ell_{1\alpha} + \ell_{2\alpha} + 2m + 2$, and N_{nm}^α are normalization factors [10].

Once the expansions for the radial amplitudes ϕ^A and ϕ^B are inserted into Eqs. (37) and (38), the wave function Ψ can schematically be written as

$$\Psi = \sum_{\alpha nm} \frac{z_{nm}^\alpha(\rho)}{\rho^4} Z_{nm}^\alpha(\rho, \Omega) . \quad (48)$$

where $z(\rho)$ stands for either $u(\rho)$ or $w(\rho)$ (yet to be determined), depending on whether channel α is constructed with partitions 1+3 or 2+2, and the factor Z_{nm}^α includes the dependence upon the hyper-radius ρ due to the correlation functions, and the angles and hyper-angles, denoted collectively by Ω .

Again, the Rayleigh-Ritz variational principle given in Eq. (28) is used to determine the hyper-radial functions $z_{nm}^\alpha(\rho)$ in Eq. (48) and ground-state energy E : the procedure is exactly the same as in the three-body problem.

The present status of ^4He [10, 46] binding-energy calculations with the CHH method is summarized in Table II. The binding energies calculated with the CHH

method using the AV18 or AV18/UIX Hamiltonian models are within 1.5 % of corresponding GFMC results [4], and of the experimental value (when the three-nucleon interaction is included). The agreement between the CHH and GFMC results is less satisfactory when the AV14 or AV14/UVIII models are considered, presumably because of slower convergence of the CHH expansions for the AV14 interaction. This interaction has tensor components which do not vanish at the origin.

TABLE II: Binding energies in MeV of ${}^4\text{He}$ calculated with the CHH method using the AV18 and AV18/UIX and the older AV14 and AV14/UVIII potential models. Also listed are the corresponding “exact” GFMC results [4] and the experimental value. The GFMC statistical errors are shown in parenthesis.

Model	CHH	GFMC
AV18	24.01	24.1(1)
AV18/UIX	27.89	28.3(1)
AV14	23.98	24.2(2)
AV14/UVIII	27.50	28.3(2)
expt.	28.3	

3.2 The Scattering-State Wave Functions

The PHH and CHH methods have also been used to calculate the wave functions in three- and four-body scattering problems. The three-body scattering problem has been studied with the PHH method both below and above deuteron breakup threshold [8, 9, 45], while for the four-body scattering problem, only the $p\,{}^3\text{He}$ and $n\,{}^3\text{H}$ systems have been studied, below breakup. We discuss here the application of the method to the pd (nd) and $p\,{}^3\text{He}$ ($n\,{}^3\text{H}$) cases, below the deuteron and ${}^3\text{He}$ (${}^3\text{H}$) breakup threshold.

In Subsection 3.2.1 we describe the technique for the scattering-state wave function, and in Subsection 3.2.2 we present some results for the three- and four-body problems.

3.2.1 The Method for Scattering-State Wave Functions

The wave function $\Psi_{1+A}^{LSJJ_z}$, having incoming orbital angular momentum L and channel spin S ($S = 1/2, 3/2$ for Nd and $S = 0, 1$ for $p^3\text{He}$ and $n^3\text{H}$) coupled to total JJ_z , is expressed as

$$\Psi_{1+A}^{LSJJ_z} = \Psi_c^{JJ_z} + \Psi_a^{LSJJ_z}, \quad (49)$$

where Ψ_c vanishes in the limit of large intercluster separation, and hence describes the system in the region where the particles are close to each other and their mutual interactions are large. In the asymptotic region, where intercluster interactions are negligible, $\Psi_a^{LSJJ_z}$, in the $p+A$ -cluster case, is written as

$$\begin{aligned} \Psi_a^{LSJJ_z} = & \sum_i \sum_{L'S'} \left[[s_i \otimes \phi_A]_{S'} \otimes Y_{L'}(\hat{\mathbf{r}}_{pA}) \right]_{JJ_z} \\ & \times \left[\delta_{LL'} \delta_{SS'} \frac{F_{L'}(pr_{pA})}{pr_{pA}} + R_{LS,L'S'}^J(p) \frac{G_{L'}(pr_{pA})}{pr_{pA}} g(r_{pA}) \right], \end{aligned} \quad (50)$$

where ϕ_A , \mathbf{r}_{pA} and p are respectively the A -cluster wave function, the proton and A -cluster relative distance and magnitude of the relative momentum. The functions F_L and G_L are the regular and irregular Coulomb functions, respectively. Note that for nd and $n^3\text{H}$ scattering, $F_L(x)/x$ and $G_L(x)/x$ are to be replaced by the regular and irregular spherical Bessel functions. The function $g(r_{pA})$ modifies the $G_L(pr_{pA})$ at small r_{pA} by regularizing it at the origin, and $g(r_{pA}) \rightarrow 1$ as $r_{pA} \geq 10 - 12$ fm, thus not affecting the asymptotic behavior of $\Psi_{1+A}^{LSJJ_z}$. Finally, the real parameters $R_{LS,L'S'}^J(p)$ are the R -matrix elements which determine phase-shifts and (for coupled channels) mixing angles at the energy $p^2/(2\mu)$, μ being the $1+A$ reduced mass. Of course, the sum over $L'S'$ is over all values compatible with a given J and parity.

The “core” wave function Ψ_c is expanded in the same PHH or CHH basis as discussed in Subsections 3.1.1 and 3.1.2. Both the matrix elements $R_{LS,L'S'}^J(p)$ and the hyper-radial functions occurring in the expansion of Ψ_c are determined applying the Kohn variational principle, which states that the functional

$$[R_{LS,L'S'}^J(p)] = R_{LS,L'S'}^J(p) - \langle \Psi_{1+A}^{L'S'JJ_z} | H - E_A - \frac{p^2}{2\mu} | \Psi_{1+A}^{LSJJ_z} \rangle \quad (51)$$

has to be stationary with respect to variations in the $R_{LS,L'S'}^J$ and the hyper-radial functions. Here $E_A = -2.225$ MeV is the deuteron energy in the three-body problem and $E_A = -7.72$ MeV ($E_A = -8.48$ MeV) is the ${}^3\text{He}$ (${}^3\text{H}$) energy in the four-body problem.

3.2.2 Results for Three- and Four-Body Scattering Problems

To check the validity of the CHH approach for the scattering problem, phase-shifts and mixing angles for nd scattering at energies below the three-body breakup threshold obtained from the AV14 have been compared with the corresponding Faddeev-Yakubovsky results [47]. The agreement between these two techniques has been found excellent, thus establishing the high accuracy of the CHH method for the scattering problem. It is important to reemphasize that this scheme, in contrast to momentum-space Faddeev methods, permits the straightforward inclusion of Coulomb distortion effects in the pd channel. Therefore, the results for pd elastic scattering are presumably as accurate as those for nd scattering.

Several results have been obtained in the last few years for the scattering observables of the three-body problem. Here we only list in Table III the nd and pd doublet and quartet scattering lengths predicted by the AV18/UIX model, which are found to be in excellent agreement with the available experimental values.

TABLE III: Predictions obtained from the AV18/UIX Hamiltonian model with the PHH method for the nd and pd doublet and quartet scattering lengths a_2 and a_4 .

	a_2 (fm)		a_4 (fm)	
	PHH	expt.	PHH	expt.
nd	0.63	0.65 ± 0.04	6.33	6.35 ± 0.02
pd	-0.02		13.7	

A similar comparison between the CHH and Faddeev-Yakubovsky methods

can be done for the four-body problem, comparing the singlet and triplet scattering lengths for the $n^3\text{H}$ zero-energy scattering problem calculated with the AV14. These results are given in Table IV. Also listed there, are the $p^3\text{He}$ singlet and triplet scattering lengths predicted by the AV18, AV18/UIX and the older AV14/UVIII models, compared with the corresponding experimental values. The latter, however, have rather large errors. In fact, these $p^3\text{He}$ data have been extrapolated to zero energy from measured data taken above 1 MeV, and therefore could suffer also of large systematic uncertainties.

The lowest energy measurements for $p^3\text{He}$ elastic scattering have been taken at a center-of-mass (c.m.) energy of 1.2 MeV, and consist in differential cross section $\sigma(\theta)$ [48] and proton analyzing power $A_p(\theta)$ [49] data (θ is the c.m. scattering angle). The theoretical prediction for $\sigma(\theta)$ obtained from the AV18 and AV18/UIX interactions, is compared with the corresponding experimental data in Fig. 2. Inspection of the figure shows that the differential cross section calculated with the AV18/UIX model is in excellent agreement with the data, except at backward angles, where the experimental cross section is slightly underpredicted. A detailed study of $p^3\text{He}$ elastic scattering is currently underway [50].

TABLE IV: Singlet a_s and triplet a_t S-wave scattering lengths (fm) for $n^3\text{H}$ scattering calculated with the AV14 and $p^3\text{He}$ scattering calculated with the AV18, AV18/UIX and the older AV14/UVIII potential models. The $n^3\text{H}$ Faddeev results and the $p^3\text{He}$ experimental values are also listed.

Method	Model	$n^3\text{H}$		$p^3\text{He}$	
		a_s	a_t	a_s	a_t
CHH	AV14	4.32	3.80		
Faddeev	AV14	4.31	3.79		
CHH	AV18			12.9	10.0
CHH	AV18/UIX			11.5	9.13
CHH	AV14/UVIII				9.24
	expt.			10.8 ± 2.6	8.1 ± 0.5
					10.2 ± 1.5

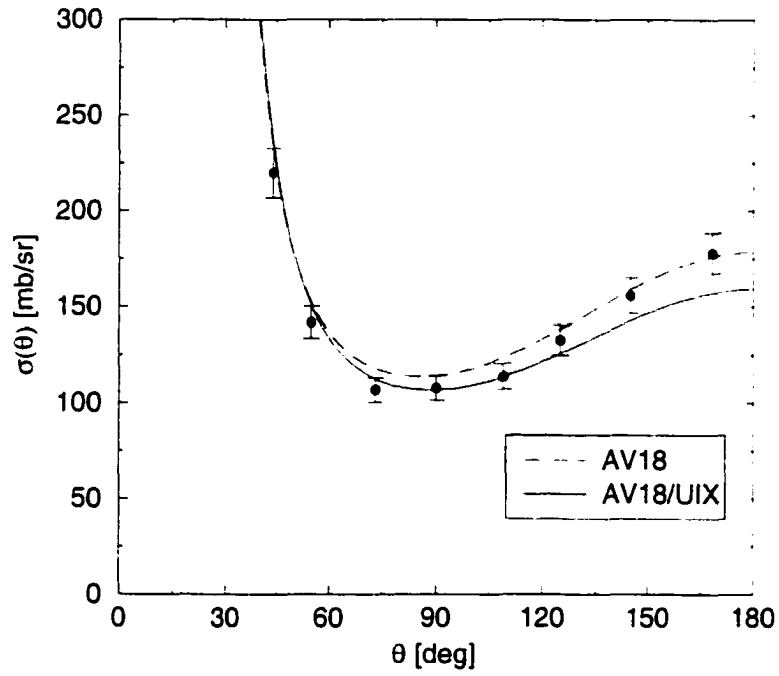


FIG. 2: Differential cross section $\sigma(\theta)$ as function of the c.m. scattering angle θ , at c.m. energy of 1.2 MeV. The experimental data are taken from Ref. [48]. The long-dashed and solid lines correspond, respectively, to the CHH calculations with the AV18 and AV18/UIX Hamiltonian models.

Chapter 4

The Nuclear Transition Operators

In studying processes where the structure of the nucleus is investigated using electromagnetic or weak probes, the construction of a realistic model for the nuclear electroweak current and charge operators becomes a fundamental aspect of the calculation. When such studies are carried out in the simplest picture of the nucleus, a non-relativistic many-body theory of interacting nucleons, the electroweak current and charge operators are expressed in terms of those associated with the individual protons and neutrons, the so-called “impulse approximation” (IA) (we will refer to these also as “one-body” operators). Such a description, however, is certainly incomplete. As already discussed in Chapter 2, the NN interaction is mediated, at long distances, by pion-exchange, and seems to be rather well described by a boson-exchange picture even at intermediate- and short-range. Thus the electroweak probe can interact with these exchanged particles, and this leads to the introduction of effective many-body current and charge operators. It should be realized that these many-body operators arise, as does the NN interaction itself, as a consequence of the elimination of the mesonic degrees of freedom from the nuclear state vector. Clearly, such an approach is justified only at energies below the threshold for meson (specifically, pion) production, since above this threshold these non-nucleonic degrees of freedom have to be explicitly included in the state vector.

Although very successful in giving a quantitative prediction of many nuclear

observables [1], this picture of the nucleus has to be considered greatly simplified. The nucleons, which are taken as effective constituents of the nucleus, are in fact composite particles (clusters of quark and gluons, in quantum chromodynamics), and the electromagnetic and weak probes can therefore excite their internal degrees of freedom. To investigate the contribution from these processes, we have included in our approach the lowest excitation of the nucleon, the Δ -resonance [13, 14]. Although these Δ -contributions have been found to be rather small in the electromagnetic case [13], they are very important in weak processes, especially in the *hep* reaction [14, 16, 25, 51]. We will return to these issues in more detail below and in the next Chapters.

This Chapter is divided into two main parts: in the first one, we describe the electromagnetic current and charge operators, in the second we discuss the model for the weak transition operator, both its vector and axial-vector components.

4.1 The Electromagnetic Transition Operators

In this section we describe the model for the electromagnetic current and charge operators. First, we discuss the model when only nucleonic degrees of freedom are considered (Subsections 4.1.1–4.1.4). In the second part of this Section, we describe the extended model wave function and current operators that include Δ -isobar degrees of freedom (Subsections 4.1.5 and 4.1.6).

4.1.1 Nuclear Current and Charge Operators

The nuclear current and charge operators are expanded into a sum of one-, two- and, in the case of the current, three-body terms:

$$\mathbf{j}(\mathbf{q}) = \sum_i \mathbf{j}_i^{(1)}(\mathbf{q}) + \sum_{i < j} \mathbf{j}_{ij}^{(2)}(\mathbf{q}) + \sum_{i < j < k} \mathbf{j}_{ijk}^{(3)}(\mathbf{q}) , \quad (52)$$

$$\rho(\mathbf{q}) = \sum_i \rho_i^{(1)}(\mathbf{q}) + \sum_{i < j} \rho_{ij}^{(2)}(\mathbf{q}) , \quad (53)$$

where \mathbf{q} is the momentum transfer. The one-body operators $\mathbf{j}^{(1)}$ and $\rho^{(1)}$ have the standard expressions obtained from a non-relativistic reduction of the covariant

single-nucleon current, and are given by

$$\mathbf{j}_i^{(1)}(\mathbf{q}) = \frac{1}{2m} \epsilon_i \left\{ \mathbf{p}_i \cdot e^{i\mathbf{q} \cdot \mathbf{r}_i} \right\} - \frac{i}{2m} \mu_i \mathbf{q} \times \boldsymbol{\sigma}_i e^{i\mathbf{q} \cdot \mathbf{r}_i} , \quad (54)$$

$$\rho_i^{(1)}(\mathbf{q}) = \rho_{i, \text{NR}}^{(1)}(\mathbf{q}) + \rho_{i, \text{RC}}^{(1)}(\mathbf{q}) , \quad (55)$$

where $\{\dots, \dots\}$ denotes the anticommutator, and

$$\rho_{i, \text{NR}}^{(1)}(\mathbf{q}) = \epsilon_i e^{i\mathbf{q} \cdot \mathbf{r}_i} , \quad (56)$$

$$\begin{aligned} \rho_{i, \text{RC}}^{(1)}(\mathbf{q}) = & \left(\frac{1}{\sqrt{1 + q_\mu^2/4m^2}} - 1 \right) \epsilon_i e^{i\mathbf{q} \cdot \mathbf{r}_i} \\ & - \frac{i}{4m^2} (2\mu_i - \epsilon_i) \mathbf{q} \cdot (\boldsymbol{\sigma}_i \times \mathbf{p}_i) e^{i\mathbf{q} \cdot \mathbf{r}_i} . \end{aligned} \quad (57)$$

The following definitions have been introduced:

$$\epsilon_i \equiv \frac{1}{2} \left[G_E^S(q_\mu^2) + G_E^V(q_\mu^2) \tau_{i,z} \right] , \quad (58)$$

$$\mu_i \equiv \frac{1}{2} \left[G_M^S(q_\mu^2) + G_M^V(q_\mu^2) \tau_{i,z} \right] , \quad (59)$$

and \mathbf{p} , $\boldsymbol{\sigma}$, and $\boldsymbol{\tau}$ are the nucleon's momentum, Pauli spin and isospin operators, respectively. The two terms proportional to $1/m^2$ in $\rho_{i, \text{RC}}^{(1)}$ are the well known Darwin-Foldy and spin-orbit relativistic corrections [52, 53], respectively. The $G_{E/M}^{S/V}(q_\mu^2)$ are the electric/magnetic (E/M) isoscalar/isovector (S/V) form factors of the nucleon, taken as function of the four-momentum transfer

$$q_\mu^2 = \mathbf{q}^2 - \omega^2 > 0 . \quad (60)$$

where, for example, the energy transfer $\omega = \sqrt{\mathbf{q}^2 + m_T^2} - m_T$ for elastic scattering on a target of mass m_T initially at rest in the lab. These form factors are related to the standard Pauli and Dirac form factors by:

$$G_E^{S/V}(q_\mu^2) = F_1^{S/V}(q_\mu^2) - \frac{q_\mu^2}{4m^2} F_2^{S/V}(q_\mu^2) , \quad (61)$$

$$G_M^{S/V}(q_\mu^2) = F_1^{S/V}(q_\mu^2) + F_2^{S/V}(q_\mu^2) . \quad (62)$$

and are normalized as

$$\begin{aligned} G_E^S(0) &= G_E^V(0) = 1 , \\ G_M^S(0) &= 0.880 \mu_N , \\ G_M^V(0) &= 4.706 \mu_N , \end{aligned} \quad (63)$$

μ_N being the nuclear magneton (n.m.). The q_μ -dependence is constrained by analyzing electron-proton and electron-deuteron scattering data. While the proton electric and magnetic form factors are experimentally fairly well known over a wide range of momentum transfers, there is significant uncertainty in the neutron form factors, particularly the electric one, which are obtained from model-dependent analyses of ed data. Until this uncertainty in the detailed behaviour of the electromagnetic form factors of the nucleon is narrowed, quantitative predictions of electro-nuclear observables at high momentum transfers will remain rather tentative.

In the next Subsections we describe: (i) the two-body nuclear current operators; (ii) the three-body nuclear current operators associated with S-wave pion rescattering; (iii) the two-body nuclear charge operators; (iv) the inclusion of Δ -isobar components in the wave functions, and (v) the Δ -isobar current operators.

4.1.2 The Two-Body Current Operators

Two-body electromagnetic current operators have conventionally been derived as the non-relativistic limit of Feynman diagrams, in which the meson-baryon couplings have been obtained from either effective chiral Lagrangians [54] or semi-empirical models for the off-shell pion-nucleon amplitude [55]. These methods of constructing effective current operators, however, do not address the problem of how to model the composite structure of the hadrons in the phenomenological meson-baryon vertices. This structure is often parametrized in terms of form factors. For the electromagnetic case, however, gauge invariance actually puts constraints on these form factors by linking the divergence of the two-body currents to the commutator of the charge operator with the NN interaction. The latter contains form factors too, but these are determined phenomenologically by fitting NN data. Thus the continuity equation reduces the model dependence of the two-body currents by relating them to the form of the interaction. This point of view has been emphasized by Riska and collaborators [56, 57, 58, 59, 60] and others [61, 62, 63], and is adopted in the treatment of two-body currents that we

discuss here. We will refer to it as the so-called Riska-prescription.

The electromagnetic current operator must satisfy the continuity equation

$$\mathbf{q} \cdot \mathbf{j}(\mathbf{q}) = [H, \rho(\mathbf{q})] \quad . \quad (64)$$

where the Hamiltonian H includes two- and three-nucleon interactions and is given in Eq. (1). To lowest order in $1/m$, the continuity equation (64) separates into separate continuity equations for the one-, two-, and many-body current operators

$$\mathbf{q} \cdot \mathbf{j}_i^{(1)}(\mathbf{q}) = \left[\frac{\mathbf{p}_i^2}{2m} \cdot \rho_{i,\text{NR}}^{(1)}(\mathbf{q}) \right] \quad , \quad (65)$$

$$\mathbf{q} \cdot \mathbf{j}_{ij}^{(2)}(\mathbf{q}) = \left[v_{ij} \cdot \rho_{i,\text{NR}}^{(1)}(\mathbf{q}) + \rho_{j,\text{NR}}^{(1)}(\mathbf{q}) \right] \quad . \quad (66)$$

and a similar equation involving three-nucleon currents and interactions.

The one-body current in Eq. (54) is easily shown to satisfy Eq. (65). The isospin- and momentum-dependence of the two- and three-nucleon interactions, however, lead to non-vanishing commutators with the non-relativistic one-body charge operator, and thus link the longitudinal part of the corresponding two- and three-body currents to the form of these interactions. At the moment we will limit our discussion to two-body currents: the investigation of three-body current operators is presented in Subsections 4.1.3 and 4.1.6.

The two-body current operator has been separated into model-independent (MI) and model-dependent (MD) terms. The former are constructed to explicitly satisfy current conservation with a given interaction model, and are determined from the interaction model itself (in the present case, the AV14 or the charge-independent part of the AV18 model) following the Riska-prescription: the latter are the purely transverse currents associated with the $\rho\pi\gamma$ and $\omega\pi\gamma$ electromagnetic couplings of Fig. 3, and are therefore unconstrained by the NN interaction.

Their explicit expressions are [1]

$$\begin{aligned} \mathbf{j}_{\rho\pi\gamma}(\mathbf{k}_i, \mathbf{k}_j) = & i \frac{f_{\pi NN} g_{\rho NN} G_{\rho\pi\gamma}(q_\mu^2)}{m_\pi m_\rho} \boldsymbol{\tau}_i \cdot \boldsymbol{\tau}_j \mathbf{k}_i \times \mathbf{k}_j \\ & \left[\frac{\boldsymbol{\sigma}_i \cdot \mathbf{k}_i}{(k_i^2 + m_\pi^2)(k_j^2 + m_\rho^2)} f_\pi(k_i) f_\rho(k_j) \right] \end{aligned}$$

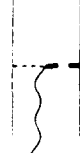


FIG. 3: Feynman diagram representation of the $\rho\pi\gamma$ and $\omega\pi\gamma$ transition operators. Solid, dashed, thick-dashed and wavy lines denote respectively nucleons, pions, vector-mesons and photons.

$$-\frac{\sigma_j \cdot \mathbf{k}_j}{(k_i^2 + m_\rho^2)(k_j^2 + m_\pi^2)} f_\rho(k_i) f_\pi(k_j) \Big] . \quad (67)$$

$$\begin{aligned} j_{\omega\pi\gamma}(\mathbf{k}_i, \mathbf{k}_j) = & i \frac{f_{\pi NN} g_{\omega NN} G_{\omega\pi\gamma}(q_\mu^2)}{m_\omega m_\pi} \mathbf{k}_i \times \mathbf{k}_j \\ & \left[\tau_{i,z} \frac{\sigma_i \cdot \mathbf{k}_i}{(k_i^2 + m_\pi^2)(k_j^2 + m_\omega^2)} f_\pi(k_i) f_\omega(k_j) \right. \\ & \left. - \tau_{j,z} \frac{\sigma_j \cdot \mathbf{k}_j}{(k_i^2 + m_\omega^2)(k_j^2 + m_\pi^2)} f_\omega(k_i) f_\pi(k_j) \right] . \end{aligned} \quad (68)$$

where \mathbf{k}_i and \mathbf{k}_j are the fractional momenta delivered to nucleons i and j with $\mathbf{q} = \mathbf{k}_i + \mathbf{k}_j$, m_π , m_ρ and m_ω are the pion, ρ -meson and ω -meson masses, respectively, and $g_{\rho NN}$ and $g_{\omega NN}$ are the vector ρNN and ωNN couplings. The q_μ -dependence of the transition form factors $G_{\rho\pi\gamma}(q_\mu^2)$ and $G_{\omega\pi\gamma}(q_\mu^2)$ is modeled, using vector-dominance, as:

$$G_{\rho\pi\gamma}(q_\mu^2) = g_{\rho\pi\gamma} / (1 + q_\mu^2 / m_\omega^2) . \quad (69)$$

$$G_{\omega\pi\gamma}(q_\mu^2) = g_{\omega\pi\gamma} / (1 + q_\mu^2 / m_\rho^2) . \quad (70)$$

The values of $G_{\rho\pi\gamma}(q_\mu^2)$ and $G_{\omega\pi\gamma}(q_\mu^2)$ at the photon point are known to be $G_{\rho\pi\gamma}(0) = g_{\rho\pi\gamma} = 0.56$, Ref. [64], and $G_{\omega\pi\gamma}(0) = g_{\omega\pi\gamma} = 0.68$, Ref. [55], from the measured widths of the $\rho \rightarrow \pi\gamma$ and $\omega \rightarrow \pi\gamma$ decays.

Finally, $f_\pi(k)$, $f_\rho(k)$ and $f_\omega(k)$ are monopole form factors introduced to take into account the composite nature of nucleons and mesons. They are given by:

$$f_\alpha(k) = \frac{\Lambda_\alpha^2 - m_\alpha^2}{\Lambda_\alpha^2 + k^2} . \quad (71)$$

with $\alpha = \pi, \rho, \omega$. The cutoff parameters Λ_π , Λ_ρ and Λ_ω in these form factors are not known. We use the values $\Lambda_\pi = 3.8 \text{ fm}^{-1}$ and $\Lambda_\rho = \Lambda_\omega = 6.3 \text{ fm}^{-1}$ obtained from studies of the deuteron electromagnetic form factors, in particular the B-structure function [65].

The MI two-body currents are obtained using the Riska-prescription. In this approach it is assumed that for a given NN interaction v_{NN} , the isospin-dependent central (v^τ), spin-spin ($v^{\sigma\tau}$) and tensor ($v^{t\tau}$) components can be attributed to exchanges of “ π -like” pseudoscalar (PS) and “ ρ -like” vector (V) mesons. Working in momentum-space, we have

$$v_{NN}(k) = [v^\tau(k) + v^{\sigma\tau}(k)\boldsymbol{\sigma}_i \cdot \boldsymbol{\sigma}_j + v^{t\tau}(k)S_{ij}(\mathbf{k})]\boldsymbol{\tau}_i \cdot \boldsymbol{\tau}_j, \quad (72)$$

where $v^\tau(k)$, $v^{\sigma\tau}(k)$ and $v^{t\tau}(k)$ are related to their configuration-space correspondents by the relations:

$$v^\tau(k) = 4\pi \int_0^\infty r^2 dr j_0(kr) v^\tau(r), \quad (73)$$

$$v^{\sigma\tau}(k) = \frac{4\pi}{k^2} \int_0^\infty r^2 dr [j_0(kr) - 1] v^{\sigma\tau}(r), \quad (74)$$

$$v^{t\tau}(k) = \frac{4\pi}{k^2} \int_0^\infty r^2 dr j_2(kr) v^{t\tau}(r). \quad (75)$$

The factor $j_0(kr) - 1$ in the expression for $v^{\sigma\tau}(k)$ ensures that its volume integral vanishes. The tensor operator in momentum-space is

$$S_{ij}(\mathbf{k}) = k^2(\boldsymbol{\sigma}_i \cdot \boldsymbol{\sigma}_j) - 3(\boldsymbol{\sigma}_i \cdot \mathbf{k})(\boldsymbol{\sigma}_j \cdot \mathbf{k}). \quad (76)$$

At intermediate and long range, the v^τ , $v^{\sigma\tau}$ and $v^{t\tau}$ interactions can be obtained by π -meson and ρ -meson exchanges. The πNN and ρNN effective Lagrangians are:

$$\mathcal{L}_{\pi NN} = -\frac{f_{\pi NN}}{m_\pi} \bar{\psi} \gamma^5 \gamma^\mu \boldsymbol{\tau} \psi \cdot \partial_\mu \boldsymbol{\pi}, \quad (77)$$

$$\mathcal{L}_{\rho NN} = g_{\rho NN} \bar{\psi} \left[\left(\gamma^\mu - \frac{\kappa_\rho}{2m} \sigma^{\mu\nu} \partial_\nu \right) \boldsymbol{\rho}_\mu \right] \cdot \boldsymbol{\tau} \psi \quad (78)$$

where ψ , $\boldsymbol{\pi}$ and $\boldsymbol{\rho}$ are the $T = 1/2$ nucleon and the $T = 1$ pion and ρ -meson fields, respectively. The Bjorken and Drell conventions are used for the γ -matrices

and the metric tensor $g^{\sigma\tau}$ [66]. $f_{\pi NN}$, $g_{\rho NN}$ and κ_ρ are the pseudovector πNN , the vector and tensor ρNN coupling constants, respectively. For example, in the CD-Bonn OBE model [2] the values for these couplings are: $f_\pi^2/4\pi = 0.075$, $g_\rho^2/4\pi = 0.84$, $\kappa_\rho = 6.1$. By performing a non-relativistic reduction of the Feynman diagram of Fig. 4(a), with π - and ρ -meson exchange, one obtains:

$$v_{NN}^{\pi,\rho}(k) = \left[v_{\rho S}(k) + [v_\pi(k) + 2v_\rho(k)]k^2(\boldsymbol{\sigma}_i \cdot \boldsymbol{\sigma}_j) - [v_\pi(k) - v_\rho(k)]S_{ij}(\mathbf{k}) \right] (\boldsymbol{\tau}_i \cdot \boldsymbol{\tau}_j) . \quad (79)$$

with

$$v_\pi(k) = -\frac{f_{\pi NN}^2}{3m_\pi^2} \frac{f_\pi^2(k)}{k^2 + m_\pi^2} . \quad (80)$$

$$v_\rho(k) = -\frac{g_{\rho NN}^2(1 + \kappa_\rho)^2}{12m^2} \frac{f_\rho^2(k)}{k^2 + m_\rho^2} . \quad (81)$$

$$v_{\rho S} = g_{\rho NN}^2 \frac{f_\rho^2(k)}{k^2 + m_\rho^2} . \quad (82)$$

and $f_\pi(k)$ ($f_\rho(k)$) denotes πNN (ρNN) monopole form factors as defined in Eq. (71). In the CD-Bonn potential the cutoff parameters are $\Lambda_\pi = 8.61 \text{ fm}^{-1}$ and $\Lambda_\rho = 6.64 \text{ fm}^{-1}$. By comparison of Eqs. (72) and (79), we have:

$$v_\pi(k) \rightarrow v_{PS}(k) = [v^{\sigma\tau}(k) - 2v^{t\tau}(k)]/3 . \quad (83)$$

$$v_\rho(k) \rightarrow v_V(k) = [v^{\sigma\tau}(k) + v^{t\tau}(k)]/3 . \quad (84)$$

$$v_{\rho S}(k) \rightarrow v_{VS}(k) = v^\tau(k) . \quad (85)$$

Even though the AV14 and AV18 are not OBE models, the functions $v_{PS}(k)$ and, to a less extent, $v_V(k)$ and $v_{VS}(k)$ projected out from their v^τ , $v^{\sigma\tau}$, and $v^{t\tau}$ components are quite similar to those of π - and ρ -meson exchanges in Eqs. (80)–(82) (with cutoff masses of order 5 fm^{-1}), as shown in Refs. [67, 68].

The “ π -like” (PS) and “ ρ -like” (V) currents are then obtained in two steps: first, minimal substitution $\partial_\mu \rightarrow \partial_\mu \pm iA_\mu$ in the Lagrangians of Eqs. (77) and (78), and in the free π -meson and ρ -meson Lagrangians leads to the expressions (for π -like as an example):

$$\mathcal{L}_{\pi\gamma NN} = -\frac{f_{\pi NN}}{m_\pi} \bar{\psi} \gamma^5 \gamma^\mu A_\mu (\boldsymbol{\tau} \times \boldsymbol{\pi})_z \psi , \quad (86)$$

$$\mathcal{L}_{\pi\pi\gamma} = -A_\mu (\boldsymbol{\pi} \times \partial^\mu \boldsymbol{\pi})_z . \quad (87)$$

Then, the PS and V MI two-body currents are calculated performing a non-relativistic reduction of the Feynman amplitudes of Fig. 4(b).

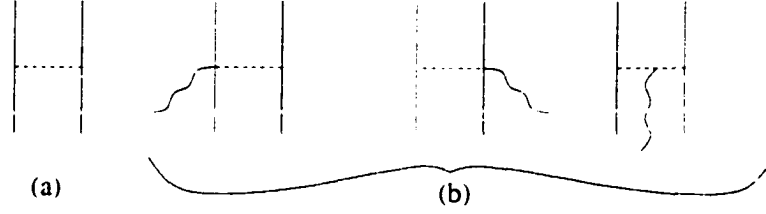


FIG. 4: (a) OBE Feynman diagram representation: (b) Feynman diagram representation of the two-body currents associated with meson-exchange. Solid, dashed and wavy lines denote respectively nucleons, mesons and photons.

The momentum-space expressions for these currents are:

$$\begin{aligned} \mathbf{j}_{ij}^{(2)}(\mathbf{k}_i, \mathbf{k}_j; \text{PS}) &= 3i G_E^V(q_\mu^2)(\boldsymbol{\tau}_i \times \boldsymbol{\tau}_j)_z \\ &\quad \left[v_{PS}(k_j) \boldsymbol{\sigma}_i (\boldsymbol{\sigma}_j \cdot \mathbf{k}_j) - v_{PS}(k_i) \boldsymbol{\sigma}_j (\boldsymbol{\sigma}_i \cdot \mathbf{k}_i) \right. \\ &\quad \left. + \frac{\mathbf{k}_i - \mathbf{k}_j}{k_i^2 - k_j^2} [v_{PS}(k_i) - v_{PS}(k_j)] (\boldsymbol{\sigma}_i \cdot \mathbf{k}_i) (\boldsymbol{\sigma}_j \cdot \mathbf{k}_j) \right]. \end{aligned} \quad (88)$$

$$\begin{aligned} \mathbf{j}_{ij}^{(2)}(\mathbf{k}_i, \mathbf{k}_j; V) &= -3i G_E^V(q_\mu^2)(\boldsymbol{\tau}_i \times \boldsymbol{\tau}_j)_z \left[v_V(k_j) \boldsymbol{\sigma}_i \times (\boldsymbol{\sigma}_j \times \mathbf{k}_j) - v_V(k_i) \boldsymbol{\sigma}_j \times (\boldsymbol{\sigma}_i \times \mathbf{k}_i) \right. \\ &\quad - \frac{v_V(k_i) - v_V(k_j)}{k_i^2 - k_j^2} [(\mathbf{k}_i - \mathbf{k}_j) (\boldsymbol{\sigma}_i \times \mathbf{k}_i) \cdot (\boldsymbol{\sigma}_j \times \mathbf{k}_j) \\ &\quad + (\boldsymbol{\sigma}_i \times \mathbf{k}_i) \boldsymbol{\sigma}_j \cdot (\mathbf{k}_i \times \mathbf{k}_j) + (\boldsymbol{\sigma}_j \times \mathbf{k}_j) \boldsymbol{\sigma}_i \cdot (\mathbf{k}_i \times \mathbf{k}_j)] \\ &\quad \left. + \frac{1}{3} \frac{\mathbf{k}_i - \mathbf{k}_j}{k_i^2 - k_j^2} [v_{VS}(k_i) - v_{VS}(k_j)] \right]. \end{aligned} \quad (89)$$

Configuration-space expressions are obtained from

$$\mathbf{j}_{ij}^{(2)}(\mathbf{q}; a) = \int d\mathbf{x} e^{i\mathbf{q} \cdot \mathbf{x}} \int \frac{d\mathbf{k}_i}{(2\pi)^3} \frac{d\mathbf{k}_j}{(2\pi)^3} e^{i\mathbf{k}_i \cdot (\mathbf{r}_i - \mathbf{x})} e^{i\mathbf{k}_j \cdot (\mathbf{r}_j - \mathbf{x})} \mathbf{j}_{ij}^{(2)}(\mathbf{k}_i, \mathbf{k}_j; a). \quad (90)$$

where $a = \text{PS}$ or V . Techniques to carry out the Fourier transforms above are discussed in Ref. [67].

We reemphasize: (i) the PS and V two-body currents have no free parameters and, by construction, satisfy the continuity equation with the given realistic interaction (here the AV14 or the charge-independent part of AV18 model); (ii) the

continuity equation requires the same form factor be used to describe the electromagnetic structure of the hadrons in the longitudinal part of the current operator and in the charge operator, while it places no restrictions on the electromagnetic form factors which may be used in the transverse parts of the current. Ignoring this ambiguity, the form factor $G_E^V(q_\mu^2)$ is used in the PS and V currents operators, in line with the “minimal” requirements of current conservation.

There are additional two-body currents associated with the momentum dependence of the interaction, but their construction is less straightforward. A procedure similar to that used to derive the PS and V currents has been generalized to the case of the currents from spin-orbit components of the interaction [69]. It consists, in essence, of attributing these to exchanges of σ -like and ω -like mesons for the isospin-independent terms, and to ρ -like mesons for the isospin-dependent ones. The explicit form of the resulting currents, denoted as SO, can be found in Refs. [68, 69]. The two-body currents from the quadratic momentum dependence of the interaction are obtained by minimal substitution $\mathbf{p}_i \rightarrow \mathbf{p}_i - \frac{1}{2} [G_E^S(q_\mu^2) + G_E^V(q_\mu^2)\tau_{i,z}] \mathbf{A}(\mathbf{r}_i)$, $\mathbf{A}(\mathbf{r}_i)$ being the vector potential, into the corresponding components. In the case of the AV14 and AV18 model, the p^2 -dependence is via \mathbf{L}^2 and $(\mathbf{L} \cdot \boldsymbol{\sigma}_1 \mathbf{L} \cdot \boldsymbol{\sigma}_2 + \text{h.c.})$ terms, and the associated currents are denoted respectively as LL and SO2 [67, 68].

We note that the SO, LL and SO2 currents are fairly short-ranged, and have both isoscalar and isovector terms. Their contribution to isovector observables is found to be numerically much smaller than that due to the leading PS (π -like) current. However, these currents give non-negligible corrections to isoscalar observables, such as the deuteron magnetic moment and B-structure function [65]. Finally it is worth emphasizing that, while the Riska-prescription is not unique, it has nevertheless been shown to provide, at low and moderate values of momentum transfer, a satisfactory description of most observables where the isovector two-body currents play a large (if not dominant) role, such as the deuteron threshold electrodisintegration [65], the neutron and proton radiative captures on protons and deuterons at low energies [65, 68], and the magnetic moments and form factors of the trinucleons [13], as will be shown in Chapter 5.

4.1.3 The Three-Body Exchange Current Associated with S-wave Pion Rescattering

In this Subsection we describe the three-body exchange current which corresponds to the main nonresonant two-pion exchange three-nucleon interaction. Although this term is not included in the Urbana VIII and IX interactions, it should be included in any complete three-nucleon interaction model, as it is implied by effective Lagrangians for the pion-nucleon system. Ignoring this inconsistency, in the present work we study the effects of the current operators associated with this three-nucleon interaction.

The isospin odd “large” component of the S-wave pion-nucleon (πN) scattering amplitude at low energy and momentum transfer may be described by the effective interaction [70]:

$$\mathcal{L}_{\pi\pi NN} = -\frac{1}{4\bar{f}_\pi^2} \bar{\psi} \gamma^\mu \boldsymbol{\tau} \cdot \boldsymbol{\psi} \boldsymbol{\pi} \times \partial_\mu \boldsymbol{\pi} . \quad (91)$$

Here \bar{f}_π is the pion decay constant ($\simeq 93$ MeV). This effective Lagrangian implies the “Weinberg-Tomozawa” relation for the isospin odd combination of the πN S-wave scattering lengths a_1, a_3 :

$$\lambda_2 = \frac{1}{6} \left(1 + \frac{m_\pi}{m} \right) (a_1 - a_3) = \frac{1}{16\pi} \left(\frac{m_\pi}{\bar{f}_\pi} \right)^2 , \quad (92)$$

which agrees well with the experimental scattering length values. Combined with the pseudovector πNN effective Lagrangian of Eq. (77), this effective Lagrangian gives rise to the three-body interaction:

$$\begin{aligned} V_S = & -\frac{1}{4m} \frac{1}{\bar{f}_\pi^2} \left(\frac{f_{\pi NN}}{m_\pi} \right)^2 \sum_{ijk \text{ cyclic}} \boldsymbol{\tau}_i \cdot \boldsymbol{\tau}_j \times \boldsymbol{\tau}_k \frac{\boldsymbol{\sigma}_i \cdot \mathbf{k}_i \boldsymbol{\sigma}_k \cdot \mathbf{k}_k}{D_i D_k} \\ & \times \left\{ \boldsymbol{\sigma}_j \cdot \mathbf{k}_i \times \mathbf{k}_k + \frac{i}{2} [\mathbf{k}_i \cdot [\mathbf{P}_i - \mathbf{P}_j] - \mathbf{k}_k \cdot [\mathbf{P}_k - \mathbf{P}_j]] \right\} . \end{aligned} \quad (93)$$

diagrammatically shown in Fig. 5. Here we have defined $\mathbf{P}_i \equiv \mathbf{p}'_i + \mathbf{p}_i$ and \mathbf{p}'_i being the initial and final momentum of nucleon i , respectively. The denominator factors D_i are defined as

$$D_i = \mathbf{k}_i^2 + m_\pi^2 . \quad (94)$$

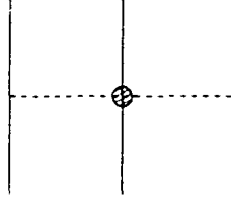


FIG. 5: Feynman diagram representation of the three-nucleon two-pion exchange interaction. Solid and dashed lines denote respectively nucleons and pions. The dashed circle corresponds to the $\pi\pi.NN$ vertex.

The derivative coupling in the Lagrangian of Eq. (91) leads to an electromagnetic contact term, that can be constructed by minimal substitution, and has the expression

$$\mathcal{L}_{\pi\pi\gamma NN} = -\frac{1}{4\bar{f}_\pi^2} \bar{\psi} \gamma^\mu A_\mu [\phi_z(\boldsymbol{\tau} \cdot \boldsymbol{\pi}) - \tau_z \boldsymbol{\pi}^2] \psi. \quad (95)$$

Together with the effective Lagrangians of Eqs. (86) and (87), this procedure gives rise to the following set of three-nucleon exchange current operators shown in Fig. 6: (a) a contact current at the S-wave rescattering vertex, (b) two contact currents at the two accompanying pseudovector πNN vertices and (c) two pion current terms.

The explicit expressions for these are correspondingly:

$$\begin{aligned} \mathbf{j}_{ijk}^a(\mathbf{q}) = & \frac{i}{8m} \frac{1}{\bar{f}_\pi^2} \left(\frac{f_{\pi NN}}{m_\pi} \right)^2 [\boldsymbol{\tau}_k \times (\boldsymbol{\tau}_j \times \boldsymbol{\tau}_i) + \boldsymbol{\tau}_i \times (\boldsymbol{\tau}_j \times \boldsymbol{\tau}_k)]_z \\ & \frac{(\boldsymbol{\sigma}_i \cdot \mathbf{k}_i)(\boldsymbol{\sigma}_k \cdot \mathbf{k}_k)}{D_i D_k} [\boldsymbol{\sigma}_j \times (\mathbf{q} - \mathbf{k}_i - \mathbf{k}_k) - i\mathbf{P}_j], \end{aligned} \quad (96)$$

$$\begin{aligned} \mathbf{j}_{ijk}^b(\mathbf{q}) = & \frac{i}{4m} \frac{1}{\bar{f}_\pi^2} \left(\frac{f_{\pi NN}}{m_\pi} \right)^2 [\boldsymbol{\tau}_i \times (\boldsymbol{\tau}_j \times \boldsymbol{\tau}_k)]_z \frac{\boldsymbol{\sigma}_i(\boldsymbol{\sigma}_k \cdot \mathbf{k}_k)}{D_k D_i'} \\ & \left\{ [\boldsymbol{\sigma}_j \cdot (\mathbf{k}_i - \mathbf{q}) \times \mathbf{k}_k] + \frac{i}{2} [\mathbf{k}_i \cdot [\mathbf{P}_i - \mathbf{P}_j] \right. \\ & \left. - \mathbf{k}_k \cdot [\mathbf{P}_k - \mathbf{P}_j] - 2m\omega + \mathbf{q} \cdot \mathbf{P}_j] \right\} + (i \rightleftharpoons k), \end{aligned} \quad (97)$$

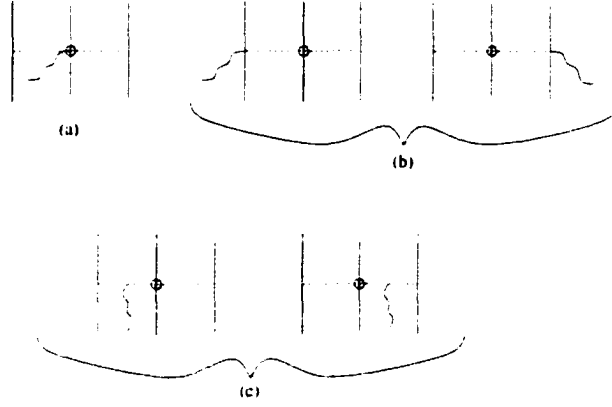


FIG. 6: Feynman diagram representation of the three-nucleon exchange current operators. Solid, dashed and wavy lines denote respectively nucleons, pions and photons. The dashed circle corresponds to the $\pi\pi NN$ vertex.

$$\begin{aligned}
 \mathbf{j}_{ijk}^c(\mathbf{q}) = & -\frac{i}{4m} \frac{1}{f_\pi^2} \left(\frac{f_{\pi NN}}{m_\pi} \right)^2 [\boldsymbol{\tau}_i \times (\boldsymbol{\tau}_j \times \boldsymbol{\tau}_k)]_z \frac{(\boldsymbol{\sigma}_i \cdot \mathbf{k}_i)(\boldsymbol{\sigma}_k \cdot \mathbf{k}_k)}{D_i D_k} \frac{2\mathbf{k}_i - \mathbf{q}}{D_i'} \\
 & \left\{ [\boldsymbol{\sigma}_j \cdot (\mathbf{k}_i - \mathbf{q}) \times \mathbf{k}_k] + \frac{i}{2} [\mathbf{k}_i \cdot [\mathbf{P}_i - \mathbf{P}_j] \right. \\
 & \left. - \mathbf{k}_k \cdot [\mathbf{P}_k - \mathbf{P}_j] - 2m\omega + \mathbf{q} \cdot \mathbf{P}_j] \right\} + (i \rightleftharpoons k) .
 \end{aligned} \tag{98}$$

In these exchange current operators, the fractions of the total momentum transfer \mathbf{q} imparted to the three nucleons are denoted \mathbf{k}_i respectively, so that $\mathbf{q} = \mathbf{k}_1 + \mathbf{k}_2 + \mathbf{k}_3$. The denominator factors D_i are defined in Eq. (94), while the denominator factors D_i' are defined as

$$D_i' = (\mathbf{q} - \mathbf{k}_i)^2 + m_\pi^2 . \tag{99}$$

The combined three-nucleon exchange current operator $\mathbf{j}^a + \mathbf{j}^b + \mathbf{j}^c$ satisfies the continuity equation with the three-nucleon interaction V_S of Eq. (93). These two-pion exchange three-nucleon currents will be labelled as $\pi\pi_S$ in Chapter 5.

4.1.4 Two-Body Charge Operators

While the MI two-body currents are linked to the form of NN interaction via the continuity equation, the most important two-body charge operators are model dependent and may be viewed as relativistic corrections. They fall into two classes: the first class includes those effective operators that represent non-nucleonic degrees of freedom, such as nucleon-antinucleon pairs or nucleon-resonances, and which arise when these degrees of freedom are eliminated from the state vector; to the second class belong those dynamical exchange charge effects that would appear even in a description explicitly including non-nucleonic excitations in the state vector, such as the $\rho\pi\gamma$ and $\omega\pi\gamma$ transition couplings. The proper forms of the former operators depend on the method of eliminating the non-nucleonic degrees of freedom [65, 71, 72]. There are nevertheless rather clear indications for the relevance of two-body charge operators from the failure of calculations based on the one-body operator in Eq. (55) in predicting the charge form factors of the three- and four-nucleon systems [13, 73], and the deuteron A-structure function and tensor polarization observable [65].

The two-body model used in the present work consists of the π -, ρ - and ω -meson exchange charge operators, as well as of the $\rho\pi\gamma$ and $\omega\pi\gamma$ charge transition couplings. The former are derived by considering the low-energy limit of the relativistic Born diagrams associated with the virtual meson photoproduction amplitude. The $\rho\pi\gamma$ and $\omega\pi\gamma$ operators are the leading corrections obtained in a non-relativistic reduction of the corresponding Feynman diagrams of Fig. 3. To reduce their model dependence, the π - and ρ -meson-exchange charge operators, the former of which gives by far the dominant contribution, are constructed using the PS (π -like) and V (ρ -like) components projected out of the isospin-dependent spin-spin and tensor terms of the interaction [73]. The resulting two-body operators are denoted as PS and V, and are here obtained from either the AV14 or the charge-independent part of the AV18. The momentum-space expressions of the PS, V, ω , $\rho\pi\gamma$ and $\omega\pi\gamma$ charge operators, $\rho_{ij}^{(2)}(\mathbf{k}_i, \mathbf{k}_j; \text{PS})$, $\rho_{ij}^{(2)}(\mathbf{k}_i, \mathbf{k}_j; \text{V})$,

$\rho_{ij}^{(2)}(\mathbf{k}_i, \mathbf{k}_j; \omega)$, $\rho_{\rho\pi\gamma}(\mathbf{k}_i, \mathbf{k}_j)$ and $\rho_{\omega\pi\gamma}(\mathbf{k}_i, \mathbf{k}_j)$ respectively, are:

$$\begin{aligned} \rho_{ij}^{(2)}(\mathbf{k}_i, \mathbf{k}_j; \text{PS}) = & -\frac{3}{2m} \left[\left[F_1^S(q_\mu^2) \boldsymbol{\tau}_i \cdot \boldsymbol{\tau}_j + F_1^V(q_\mu^2) \tau_{j,z} \right] v_{PS}(k_j) \boldsymbol{\sigma}_i \cdot \mathbf{q} \boldsymbol{\sigma}_j \cdot \mathbf{k}_j \right. \\ & \left. + \left[F_1^S(q_\mu^2) \boldsymbol{\tau}_i \cdot \boldsymbol{\tau}_j + F_1^V(q_\mu^2) \tau_{i,z} \right] v_{PS}(k_i) \boldsymbol{\sigma}_i \cdot \mathbf{k}_i \boldsymbol{\sigma}_j \cdot \mathbf{q} \right]. \quad (100) \end{aligned}$$

$$\begin{aligned} \rho_{ij}^{(2)}(\mathbf{k}_i, \mathbf{k}_j; V) = & -\frac{3}{2m} \left[\left[F_1^S(q_\mu^2) \boldsymbol{\tau}_i \cdot \boldsymbol{\tau}_j + F_1^V(q_\mu^2) \tau_{j,z} \right] \right. \\ & \times v_V(k_j) (\boldsymbol{\sigma}_i \times \mathbf{q}) \cdot (\boldsymbol{\sigma}_j \times \mathbf{k}_j) \\ & + \left[F_1^S(q_\mu^2) \boldsymbol{\tau}_i \cdot \boldsymbol{\tau}_j + F_1^V(q_\mu^2) \tau_{i,z} \right] \\ & \left. \times v_V(k_i) (\boldsymbol{\sigma}_j \times \mathbf{q}) \cdot (\boldsymbol{\sigma}_i \times \mathbf{k}_i) \right]. \quad (101) \end{aligned}$$

$$\begin{aligned} \rho_{ij}^{(2)}(\mathbf{k}_i, \mathbf{k}_j; \omega) = & \frac{g_{\omega NN}^2}{8m^3} \left[\left[F_1^S(q_\mu^2) (\boldsymbol{\tau}_i \cdot \boldsymbol{\tau}_j) + F_1^V(q_\mu^2) \tau_{i,z} \right] \right. \\ & \times \frac{(\boldsymbol{\sigma}_i \times \mathbf{q}) \cdot (\boldsymbol{\sigma}_j \times \mathbf{k}_j)}{k_j^2 + m_\omega^2} f_\omega(k_j) \\ & + \left[F_1^S(q_\mu^2) (\boldsymbol{\tau}_i \cdot \boldsymbol{\tau}_j) + F_1^V(q_\mu^2) \tau_{j,z} \right] \\ & \left. \times \frac{(\boldsymbol{\sigma}_j \times \mathbf{q}) \cdot (\boldsymbol{\sigma}_i \times \mathbf{k}_i)}{k_i^2 + m_\omega^2} f_\omega(k_i) \right]. \quad (102) \end{aligned}$$

$$\begin{aligned} \rho_{\rho\pi\gamma}(\mathbf{k}_i, \mathbf{k}_j) = & -\frac{f_{\pi NN} g_{\rho NN} (1 + \kappa_\rho)}{2m_\pi m_\rho m} G_{\rho\pi\gamma}(q_\mu^2) \boldsymbol{\tau}_i \cdot \boldsymbol{\tau}_j \\ & \left[\frac{\boldsymbol{\sigma}_i \cdot \mathbf{k}_i (\boldsymbol{\sigma}_j \times \mathbf{k}_j) \cdot (\mathbf{k}_i \times \mathbf{k}_j)}{(k_i^2 + m_\pi^2)(k_j^2 + m_\rho^2)} f_\pi(k_i) f_\rho(k_j) \right. \\ & \left. - \frac{\boldsymbol{\sigma}_j \cdot \mathbf{k}_j (\boldsymbol{\sigma}_i \times \mathbf{k}_i) \cdot (\mathbf{k}_i \times \mathbf{k}_j)}{(k_i^2 + m_\rho^2)(k_j^2 + m_\pi^2)} f_\rho(k_i) f_\pi(k_j) \right]. \quad (103) \end{aligned}$$

$$\begin{aligned} \rho_{\omega\pi\gamma}(\mathbf{k}_i, \mathbf{k}_j) = & -\frac{f_{\pi NN} g_{\omega NN}}{2m_\pi m_\omega m} G_{\omega\pi\gamma}(q_\mu^2) \\ & \left[\tau_{i,z} \frac{\boldsymbol{\sigma}_i \cdot \mathbf{k}_i (\boldsymbol{\sigma}_j \times \mathbf{k}_j) \cdot (\mathbf{k}_i \times \mathbf{k}_j)}{(k_i^2 + m_\pi^2)(k_j^2 + m_\omega^2)} f_\pi(k_i) f_\omega(k_j) \right. \\ & \left. - \tau_{j,z} \frac{\boldsymbol{\sigma}_j \cdot \mathbf{k}_j (\boldsymbol{\sigma}_i \times \mathbf{k}_i) \cdot (\mathbf{k}_i \times \mathbf{k}_j)}{(k_i^2 + m_\omega^2)(k_j^2 + m_\pi^2)} f_\omega(k_i) f_\pi(k_j) \right]. \quad (104) \end{aligned}$$

where $F_1^{S/V}(q_\mu^2)$ are the standard Dirac and Pauli form factors, m is the nucleon mass and v_{PS} and v_V are given in Eqs. (83) and (84). Coupling constants and cutoff parameters are discussed in Subsection 4.1.2.

We note finally that in the pion (as well as vector meson) charge operators there are additional contributions due to the energy dependence of the pion propagator and direct coupling of the photon to the exchanged pion (ρ -meson). However, these operators give rise to non-local isovector contributions which are expected to provide only small corrections to the leading local terms. For example these operators would only contribute to the isovector combination of the ^3He and ^3H charge form factors, which is anyway a factor of three smaller than the isoscalar. Thus they are neglected in the present model.

4.1.5 Δ -Isobar Components in the Wave Functions: the TCO Method

When Δ -isobar degrees of freedom are considered, the nuclear wave function is written as

$$\Psi_{N+\Delta} = \Psi(NNN \dots) + \Psi^{(1)}(NN\Delta \dots) + \Psi^{(2)}(N\Delta\Delta \dots) + \dots \quad (105)$$

where Ψ is that part of the total wave function consisting only of nucleons, the term $\Psi^{(1)}$ is the component in which a single nucleon has been converted into a Δ -isobar, and so on. The nuclear two-body interaction is taken as

$$v_{ij} = v_{ij}(NN \rightarrow NN) + [v_{ij}(NN \rightarrow N\Delta) + v_{ij}(NN \rightarrow \Delta\Delta) + \text{H.c.}] \quad (106)$$

where $v_{ij}(NN \rightarrow NN)$ is the nuclear interaction studied in Chapter 2, and the transition interactions $v_{ij}(NN \rightarrow N\Delta)$ and $v_{ij}(NN \rightarrow \Delta\Delta)$ are responsible for generating Δ -isobar admixtures in the wave function. The long-range part of v_{ij} is due to pion-exchange. In an effective Lagrangian approach, the $\pi N\Delta$ vertex interaction is written as:

$$\mathcal{L}_{\pi N\Delta} = \frac{f_{\pi N\Delta}}{m_\pi} \bar{\psi}^\mu \mathbf{T} \psi \cdot \partial_\mu \boldsymbol{\pi} + \text{H.c.} \quad (107)$$

where ψ^μ is the isospin-spin 3/2 field of the Δ . \mathbf{T} is the isospin-transition operator which convert the nucleon into a Δ isobar, and $f_{\pi N\Delta}$ is the $\pi N\Delta$ coupling constant. The non-relativistic reduction of the Feynman amplitudes in Fig. 7 leads to $NN \rightarrow N\Delta$ and $NN \rightarrow \Delta\Delta$ interactions $v_{ij}(NN \rightarrow N\Delta)$ and $v_{ij}(NN \rightarrow \Delta\Delta)$ of the form:

$$v_{ij}(NN \rightarrow N\Delta) = \left[v^{\sigma\tau II}(r_{ij}) \boldsymbol{\sigma}_i \cdot \mathbf{S}_j + v^{t\tau II}(r_{ij}) S_{ij}^{II} \right] \boldsymbol{\tau}_i \cdot \mathbf{T}_j, \quad (108)$$

$$v_{ij}(\Delta\Delta \rightarrow \Delta\Delta) = \left[v^{\sigma\tau III}(r_{ij}) \mathbf{S}_i \cdot \mathbf{S}_j + v^{t\tau III}(r_{ij}) S_{ij}^{III} \right] \mathbf{T}_i \cdot \mathbf{T}_j. \quad (109)$$

Here, \mathbf{S}_i is the spin-transition operator, and S_{ij}^{II} and S_{ij}^{III} are tensor operators in which, respectively, the Pauli spin operators of either particle i or j , and both particles i and j are replaced by corresponding spin-transition operators. The functions $v^{\sigma\tau II}(r)$, etc., are given by:

$$v^{\sigma\tau\alpha}(r) = \frac{(ff)_\alpha}{4\pi} \frac{m_\pi}{3} \frac{e^{-x}}{x} C(x), \quad (110)$$

$$v^{t\tau\alpha}(r) = \frac{(ff)_\alpha}{4\pi} \frac{m_\pi}{3} \left(1 + \frac{3}{x} + \frac{3}{x^2} \right) \frac{e^{-x}}{x} C^2(x), \quad (111)$$

where $\alpha = \text{II, III}$, $x \equiv m_\pi r$, $(ff)_\alpha = f_{\pi NN} f_{\pi N\Delta}$, $f_{\pi N\Delta} f_{\pi N\Delta}$, for $\alpha = \text{II, III}$, respectively, and the cutoff function $C(x) = 1 - e^{-\lambda x^2}$. In the Argonne v_{28Q} [77] (AV28Q) interaction, which contains explicit N and Δ degrees of freedom, $f_{\pi N\Delta} = (6\sqrt{2}/5)f_{\pi NN}$, as obtained in the quark model, and $\lambda = 4.09$.

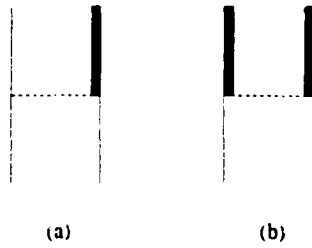


FIG. 7: Feynman diagram representation of the $NN \rightarrow N\Delta$ and $NN \rightarrow \Delta\Delta$ transition interactions due to one pion exchange. Solid, thick-solid, and dashed lines denote nucleons, Δ -isobars, and pions, respectively.

The short- and intermediate-range parts of v_{ij} , influenced by more complex dynamics, are constrained by fitting NN scattering data at lab energy ≤ 400 MeV and deuteron properties [26], as earlier discussed in Chapter 2.

Once the NN , $N\Delta$ and $\Delta\Delta$ interactions have been determined, the problem is reduced to solving the N - Δ coupled-channel Schrödinger equation. In principle, at least for the $A=3$ systems, Faddeev and hyperspherical-harmonics techniques can be used (and, indeed, Faddeev methods have been used in the past [74, 75]) to this end, although the large number of N - Δ channels involved makes the practical implementation of these methods difficult. A somewhat simpler approach consists of a generalization of the correlation operator technique [76], which has proven very useful in the variational theory of light nuclei, particularly in the context of variational Monte Carlo calculations [4, 27]. In the transition correlation operator (TCO) approach, as this method is known [25], the nuclear wave function is written as

$$\Psi_{N+\Delta} = \left[\mathcal{S} \prod_{i < j} (1 + U_{ij}^{\text{TR}}) \right] \Psi . \quad (112)$$

where Ψ is the purely nucleonic component, \mathcal{S} is the symmetrizer, and the transition operators U_{ij}^{TR} convert NN pairs into $N\Delta$ and $\Delta\Delta$ pairs. The latter are defined as

$$U_{ij}^{\text{TR}} = U_{ij}^{N\Delta} + U_{ij}^{\Delta N} + U_{ij}^{\Delta\Delta} . \quad (113)$$

with $U_{ij}^{N\Delta}$ and $U_{ij}^{\Delta\Delta}$ given in Eqs. (108)-(109), where the functions $v^{\sigma\tau\alpha}$ and $v^{t\tau\alpha}$ are replaced by transition correlation functions $u^{\sigma\tau\alpha}$ and $u^{t\tau\alpha}$, respectively, yet to be determined. In the present study the Ψ is taken from CHH solutions of the AV14/UVIII or AV18/UIX Hamiltonians with nucleons only interactions, while the transition correlation functions $u^{\sigma\tau\alpha}$ etc. are obtained solving the two-body bound and low-energy scattering-state problem with the AV28Q interaction. The correlation functions $u^{\sigma\tau II}(r)$, etc. are shown in Fig. 8.

The validity of the approximation inherent to Eq. (112) was discussed at length in the original work [25], and has been reviewed more recently in Ref. [13]. Here we only note that: (i) since the correlation functions $u^{\sigma\tau II}(r)$, etc. are short-ranged (see Fig. 8), they are expected to have a rather weak dependence on A ; this should allow us to use correlation functions obtained solving a two-body problem also for processes involving three and four nucleons. (ii) The AV28Q interaction provided an excellent description of the NN database available in the early eighties, but

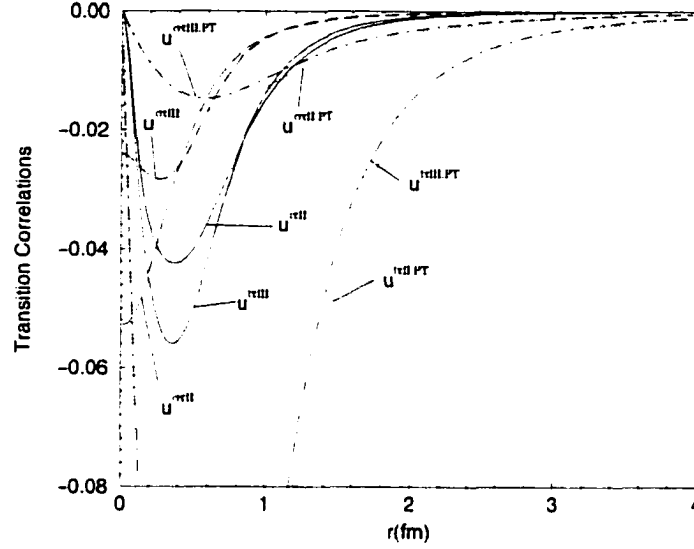


FIG. 8: Transition correlation functions $u^{\sigma\tau II}(r)$, $u^{\tau\tau II}(r)$, etc. obtained for the AV28Q model [77], and perturbation theory equivalents $u^{\sigma\tau II,PT}(r)$, $u^{\tau\tau II,PT}(r)$, etc.

no attempt has been made to refit this model to the more recent and much more extensive Nijmegen database [78].

We finally note that the normalization of the full wave function $\Psi_{N+\Delta}$ in the TCO approach can be written:

$$\begin{aligned} \langle \Psi_{N+\Delta} | \Psi_{N+\Delta} \rangle &= \langle \Psi | 1 + \sum_{i < j} [2 U_{ij}^{\Delta N \dagger} U_{ij}^{\Delta N} + U_{ij}^{\Delta \Delta \dagger} U_{ij}^{\Delta \Delta}] \\ &\quad + \sum_{i < j, k \neq i, j} [U_{ij}^{\Delta N \dagger} U_{ik}^{\Delta N} + U_{ij}^{N \Delta \dagger} U_{kj}^{N \Delta}] | \Psi \rangle + \dots \end{aligned} \quad (114)$$

where we have retained two- and three-body contributions. The wave function normalization ratios $\langle \Psi_{N+\Delta} | \Psi_{N+\Delta} \rangle / \langle \Psi | \Psi \rangle$, obtained for the bound three- and four-nucleon systems, are listed in Table V. Thus, the probability P_Δ of Δ -components in the nuclear wave function is about 2 % and 6 % in three- and four-body nuclei, respectively. As a comparison, $P_\Delta = 0.5$ % in the deuteron [26, 77].

TABLE V: The wave function normalization ratios $\langle \Psi_{N+\Delta} | \Psi_{N+\Delta} \rangle / \langle \Psi | \Psi \rangle$ obtained for the bound three- and four-nucleon systems, when the TCO calculation is based on the AV28Q interaction. The purely nucleonic CHH wave functions $|\Psi\rangle$ correspond to the AV18/UIX Hamiltonian model.

Model	${}^3\text{H}$	${}^3\text{He}$	${}^4\text{He}$
AV28Q	1.0238	1.0234	1.0650

The more traditional way of estimating the importance of the Δ -isobar degrees of freedom in electroweak observables, is the so-called first-order perturbation theory (PT). In such an approach, the Δ -isobar admixtures in the wave functions are generated via

$$\Psi^{(1)} = \frac{1}{m - m_\Delta} \sum_{i < j} [v_{ij}(NN \rightarrow N\Delta) + v_{ij}(NN \rightarrow \Delta N)] \Psi . \quad (115)$$

$$\Psi^{(2)} = \frac{1}{2(m - m_\Delta)} \sum_{i < j} v_{ij}(NN \rightarrow \Delta\Delta) \Psi . \quad (116)$$

where the Δ -isobar kinetic energy contributions in the denominators of Eqs. (115) and (116) have been neglected (static Δ approximation).

When compared to the TCO approach, the PT approximation produces $N\Delta$ and $\Delta\Delta$ admixtures that are too large at short distances, and therefore leads to a substantial overprediction of the effects associated with Δ isobars in electroweak observables [25], as can be seen in Fig. 8.

4.1.6 Electromagnetic Δ -Currents

In a full description in which also Δ -isobar degrees of freedom are included, the one-body current is written as

$$\mathbf{j}_i^{(1)}(\mathbf{q}) = \sum_{B, B' = N, \Delta} \mathbf{j}_i(\mathbf{q}; B \rightarrow B') . \quad (117)$$

where $\mathbf{j}_i(\mathbf{q}; N \rightarrow N)$ is the nucleonic current component given in Eq. (54) and

$$\mathbf{j}_i(\mathbf{q}; N \rightarrow \Delta) = -\frac{i}{2m} G_{\gamma N\Delta}(q_\mu^2) e^{i\mathbf{q} \cdot \mathbf{r}_i} \mathbf{q} \times \mathbf{S}_i T_{i,z} , \quad (118)$$

$$\mathbf{j}_i(\mathbf{q}; \Delta \rightarrow \Delta) = -\frac{i}{24m} G_{\gamma\Delta\Delta}(q_\mu^2) e^{i\mathbf{q}\cdot\mathbf{r}_i} \mathbf{q} \times \boldsymbol{\Sigma}_i (1 + \Theta_{i,z}) . \quad (119)$$

Here $\boldsymbol{\Sigma}$ ($\boldsymbol{\Theta}$) is the Pauli operator for the Δ spin 3/2 (isospin 3/2), and the expression for $\mathbf{j}_i(\mathbf{q}; \Delta \rightarrow N)$ is obtained from that for $\mathbf{j}_i(\mathbf{q}; N \rightarrow \Delta)$ by replacing the transition spin and isospin operators by their Hermitian conjugates. The $N\Delta$ -transition and Δ electromagnetic form factors, respectively $G_{\gamma N\Delta}$ and $G_{\gamma\Delta\Delta}$, are parametrized as

$$G_{\gamma N\Delta}(q_\mu^2) = \frac{\mu_{\gamma N\Delta}}{(1 + q_\mu^2/\Lambda_{N\Delta,1}^2)^2 \sqrt{1 + q_\mu^2/\Lambda_{N\Delta,2}^2}} . \quad (120)$$

$$G_{\gamma\Delta\Delta}(q_\mu^2) = \frac{\mu_{\gamma\Delta\Delta}}{(1 + q_\mu^2/\Lambda_{\Delta\Delta}^2)^2} . \quad (121)$$

The $N\Delta$ -transition magnetic moment $\mu_{\gamma N\Delta}$ is taken equal to 3 n.m., as obtained from an analysis of γN data in the Δ -resonance region [79]; this analysis also gives $\Lambda_{N\Delta,1} = 0.84$ GeV and $\Lambda_{N\Delta,2} = 1.2$ GeV. The value used for the Δ magnetic moment $\mu_{\gamma\Delta\Delta}$ is 4.35 n.m. by averaging results of a soft-photon analysis of pion-proton bremsstrahlung data near the Δ^{++} resonance [80], and $\Lambda_{\Delta\Delta} = 0.84$ GeV as in the dipole parametrization of the nucleon form factor. In principle, N to Δ excitation can also occur via an electric quadrupole transition. Its contribution, however, has been ignored, since the associated pion photoproduction amplitude is found to be experimentally small at resonance [81]. Also neglected is the Δ convection current.

The $N\Delta$ -transition two-body currents are written as

$$\mathbf{j}_{ij}^{(2)}(\mathbf{q}) = \sum'_{B_i, B_j = N, \Delta} \sum'_{B'_i, B'_j = N, \Delta} \mathbf{j}_{ij}(\mathbf{q}; B_i B_j \rightarrow B'_i B'_j) . \quad (122)$$

where the prime over the summation symbols indicates that terms involving more than a single Δ have been neglected in the present study. The $NN \rightarrow NN$ two-body terms have already been discussed. The two-body terms involving at most a single Δ are explicitly given by

$$\begin{aligned} \mathbf{j}_{ij}(\mathbf{q}; NN \rightarrow N\Delta) = & (\boldsymbol{\tau}_i \times \mathbf{T}_j)_z \left[\left[\boldsymbol{\sigma}_i (\mathbf{S}_j \cdot \hat{\mathbf{r}}_{ij}) e^{i\mathbf{q}\cdot\mathbf{r}_i} + (\boldsymbol{\sigma}_i \cdot \hat{\mathbf{r}}_{ij}) \mathbf{S}_j e^{i\mathbf{q}\cdot\mathbf{r}_j} \right] h(r_{ij}) \right. \\ & \left. + e^{i\mathbf{q}\cdot\mathbf{R}_{ij}} (\boldsymbol{\sigma}_i \cdot \nabla_i) (\mathbf{S}_j \cdot \nabla_j) \hat{\mathbf{r}}_{ij} \bar{h}(r_{ij}) \right] , \end{aligned} \quad (123)$$

where $\mathbf{r}_{ij} = \mathbf{r}_i - \mathbf{r}_j$, $\mathbf{R}_{ij} = (\mathbf{r}_i + \mathbf{r}_j)/2$, and the functions $h(r)$ and $\bar{h}(r)$ are defined, respectively, as

$$h(r) \equiv - \left(\frac{f_{\pi NN} f_{\pi N\Delta}}{4\pi} \right) \frac{1}{x^2} (1+x) e^{-x}, \quad (124)$$

$$\bar{h}(r) \equiv \left(\frac{f_{\pi NN} f_{\pi N\Delta}}{4\pi} \right) \frac{1}{m_\pi^2} \int_{-\frac{1}{2}}^{+\frac{1}{2}} dz e^{-iz\mathbf{q}\cdot\mathbf{r}} e^{-rL(z)}, \quad (125)$$

with $x = m_\pi r$ and $L(z) = [m_\pi^2 + q^2(1/4 - z^2)]^{1/2}$. Terms explicitly proportional to \mathbf{q} in Eq. (123) have been dropped, since in applications only the transverse components of $\mathbf{j}(\mathbf{q})$ occur. The three terms in Eq. (123) are associated with diagrams (a), (b) and (c) in Fig. 9, respectively, and can be obtained from the well known expression of the two-body nucleonic currents due to pion-exchange by replacing $\boldsymbol{\sigma}_j$ and $\boldsymbol{\tau}_j$ with \mathbf{S}_j and \mathbf{T}_j , respectively.

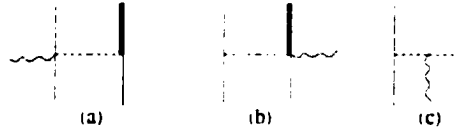


FIG. 9: $N\Delta$ -transition two-body currents due to pion exchange.

To account for the hadron compositeness, form factors must be introduced at the πNN and $\pi N\Delta$ vertices. In the case of $v_{ij}(NN \rightarrow N\Delta)$ interaction, an r -space Gaussian cutoff has been used. However, for the $j(NN \rightarrow N\Delta)$ above it has been found convenient to introduce monopole form factors given in Eq. (71) with $\alpha = \pi$ and $\Lambda_\pi = 4.56 \text{ fm}^{-1}$. This value for Λ_π is consistent with that obtained from the tensor component of $v_{ij}(NN \rightarrow N\Delta)$. Finally, the expression in Eq. (123) is multiplied by the isovector form factor $G_E^V(q_\mu^2)$.

4.2 The Weak Transition Operators

We describe here the model for the weak current and charge operators. As for the electromagnetic case, in the first part we discuss the model when only nucleonic degrees of freedom are included. In the second part we describe the Δ -isobar contributions.

4.2.1 The Nuclear Weak Current and Charge Operators

The nuclear weak current and charge operators have polar-vector/scalar (V) and axial-vector/pseudoscalar (A) components

$$\mathbf{j}_{\pm}(\mathbf{q}) = \mathbf{j}_{\pm}(\mathbf{q}; V) + \mathbf{j}_{\pm}(\mathbf{q}; A) . \quad (126)$$

$$\rho_{\pm}(\mathbf{q}) = \rho_{\pm}(\mathbf{q}; V) + \rho_{\pm}(\mathbf{q}; A) . \quad (127)$$

where \mathbf{q} is the momentum transfer, and the subscripts \pm denote charge raising (+) or lowering (-) isospin indices. Each component, in turn, consists of one-, two-, and many-body terms that operate on the nucleon degrees of freedom:

$$\mathbf{j}(\mathbf{q}; a) = \sum_i \mathbf{j}_i^{(1)}(\mathbf{q}; a) + \sum_{i < j} \mathbf{j}_{ij}^{(2)}(\mathbf{q}; a) + \dots . \quad (128)$$

$$\rho(\mathbf{q}; a) = \sum_i \rho_i^{(1)}(\mathbf{q}; a) + \sum_{i < j} \rho_{ij}^{(2)}(\mathbf{q}; a) + \dots . \quad (129)$$

where $a=V, A$ and the isospin indices have been suppressed to simplify the notation. The one-body operators $\mathbf{j}_i^{(1)}$ and $\rho_i^{(1)}$ have the standard expressions obtained from a non-relativistic reduction of the covariant single-nucleon V and A currents, and are listed below for convenience. The V-charge operator is written as

$$\rho_i^{(1)}(\mathbf{q}; V) = \rho_{i, \text{NR}}^{(1)}(\mathbf{q}; V) + \rho_{i, \text{RC}}^{(1)}(\mathbf{q}; V) . \quad (130)$$

with

$$\rho_{i, \text{NR}}^{(1)}(\mathbf{q}; V) = \tau_{i, \pm} e^{i\mathbf{q} \cdot \mathbf{r}_i} , \quad (131)$$

$$\rho_{i, \text{RC}}^{(1)}(\mathbf{q}; V) = -i \frac{(2\mu^v - 1)}{4m^2} \tau_{i, \pm} \mathbf{q} \cdot (\boldsymbol{\sigma}_i \times \mathbf{p}_i) e^{i\mathbf{q} \cdot \mathbf{r}_i} . \quad (132)$$

The V-current operator is expressed as

$$\mathbf{j}_i^{(1)}(\mathbf{q}; V) = \frac{1}{2m} \tau_{i, \pm} \{ \mathbf{p}_i \cdot e^{i\mathbf{q} \cdot \mathbf{r}_i} \} - i \frac{\mu^v}{2m} \tau_{i, \pm} \mathbf{q} \times \boldsymbol{\sigma}_i e^{i\mathbf{q} \cdot \mathbf{r}_i} , \quad (133)$$

where μ^v is the isovector nucleon magnetic moment ($\mu^v = 4.709$ n.m.). Finally, the isospin raising and lowering operators are defined as

$$\tau_{i, \pm} \equiv (\tau_{i, x} \pm i \tau_{i, y})/2 . \quad (134)$$

The term proportional to $1/m^2$ in $\rho_{i,RC}^{(1)}(\mathbf{q}; V)$ is the well known [52, 53] spin-orbit relativistic correction. The vector charge and current operators above are simply obtained from the corresponding isovector electromagnetic operators of Eqs. (54)-(59), by the replacement $\tau_{i,z}/2 \rightarrow \tau_{i,\pm}$, in accordance with the conserved-vector-current (CVC) hypothesis. The q_μ -dependence of the nucleon's vector form factors (and, in fact, axial-vector form factors below) has been ignored, since in this work we are interested in weak processes involving very small momentum transfers. For this same reason, the Darwin-Foldy relativistic correction proportional to $q^2/(8m^2)$ in $\rho_{i,RC}^{(1)}(\mathbf{q}; V)$ has also been neglected.

The A-charge operator is given, to leading order, by

$$\rho_i^{(1)}(\mathbf{q}; A) = -\frac{g_A}{2m} \tau_{i,\pm} \boldsymbol{\sigma}_i \cdot \{\mathbf{p}_i \cdot e^{i\mathbf{q}\cdot\mathbf{r}_i}\} . \quad (135)$$

while the A-current operator considered in the present work includes leading and next-to-leading order corrections in an expansion in powers of p/m , i.e.

$$\mathbf{j}_i^{(1)}(\mathbf{q}; A) = \mathbf{j}_{i,NR}^{(1)}(\mathbf{q}; A) + \mathbf{j}_{i,RC}^{(1)}(\mathbf{q}; A) . \quad (136)$$

with

$$\mathbf{j}_{i,NR}^{(1)}(\mathbf{q}; A) = -g_A \tau_{i,\pm} \boldsymbol{\sigma}_i e^{i\mathbf{q}\cdot\mathbf{r}_i} . \quad (137)$$

$$\begin{aligned} \mathbf{j}_{i,RC}^{(1)}(\mathbf{q}; A) &= \frac{g_A}{4m^2} \tau_{i,\pm} \left(\boldsymbol{\sigma}_i \{\mathbf{p}_i^2, e^{i\mathbf{q}\cdot\mathbf{r}_i}\} - \{\boldsymbol{\sigma}_i \cdot \mathbf{p}_i, \mathbf{p}_i \cdot e^{i\mathbf{q}\cdot\mathbf{r}_i}\} \right. \\ &\quad \left. - \frac{1}{2} \boldsymbol{\sigma}_i \cdot \mathbf{q} \{\mathbf{p}_i \cdot e^{i\mathbf{q}\cdot\mathbf{r}_i}\} - \frac{1}{2} \mathbf{q} \{\boldsymbol{\sigma}_i \cdot \mathbf{p}_i, e^{i\mathbf{q}\cdot\mathbf{r}_i}\} + i \mathbf{q} \times \mathbf{p}_i e^{i\mathbf{q}\cdot\mathbf{r}_i} \right) \\ &\quad - \frac{g_P}{2m m_\mu} \tau_{i,\pm} \mathbf{q} \boldsymbol{\sigma}_i \cdot \mathbf{q} e^{i\mathbf{q}\cdot\mathbf{r}_i} . \end{aligned} \quad (138)$$

The axial coupling constant g_A is taken to be [82] 1.2654 ± 0.0042 , by averaging values obtained, respectively, from the beta asymmetry in the decay of polarized neutrons (1.2626 ± 0.0033 [83, 84]) and the half-lives of the neutron and superallowed $0^+ \rightarrow 0^+$ transitions, i.e. $[2ft(0^+ \rightarrow 0^+)/ft(n) - 1] = 1.2681 \pm 0.0033$ [82]. The last term in Eq. (138) is the induced pseudoscalar contribution (m_μ is the

muon mass), for which the coupling constant g_P is taken as [85] $g_P = -6.78 g_A$. Note that in the limit $q=0$, the expressions for $\rho_{i, NR}^{(1)}(\mathbf{q}; V)$ and $\mathbf{j}_{i, NR}^{(1)}(\mathbf{q}; A)$ reduce to the familiar Fermi and Gamow-Teller operators.

In the next five Subsections we describe: (i) the two-body V-current and V-charge operators, required by the CVC hypothesis; (ii) the two-body A-current and A-charge operators due to π - and ρ -meson exchanges, and the $\rho\pi$ mechanism; (iii) the V and A current and charge operators associated with excitation of Δ -isobar resonances [14].

4.2.2 Two-Body Weak Vector Current and Charge Operators

The weak vector (V) current and charge operators are derived from the corresponding electromagnetic operators by making use of the CVC hypothesis, which for two-body terms implies

$$\left[\frac{1}{2} (\tau_{i,a} + \tau_{j,a}) \cdot \mathbf{j}_{ij,z}^{(2)}(\mathbf{q}; \gamma) \right] = i \epsilon_{a,b} \mathbf{j}_{ij,b}^{(2)}(\mathbf{q}; V) . \quad (139)$$

where $\mathbf{j}_{ij,z}^{(2)}(\mathbf{q}; \gamma)$ are the isovector (charge-conserving) two-body electromagnetic currents, and $a, b = x, y, z$ are isospin Cartesian components. A similar relation holds between the electromagnetic charge operators and its weak vector counterparts. The charge-raising or lowering weak vector current (or charge) operators are then simply obtained from the linear combinations

$$\mathbf{j}_{ij,\pm}^{(2)}(\mathbf{q}; V) = \mathbf{j}_{ij,x}^{(2)}(\mathbf{q}; V) \pm i \mathbf{j}_{ij,y}^{(2)}(\mathbf{q}; V) . \quad (140)$$

Using Eq. (139), it is easy to see that the two-body vector current and charge operators are simply obtained from the corresponding isovector electromagnetic terms by making the substitutions $\tau_{i,z} \rightarrow \tau_{i,\pm}$ and $(\boldsymbol{\tau}_i \times \boldsymbol{\tau}_j)_z \rightarrow (\boldsymbol{\tau}_i \times \boldsymbol{\tau}_j)_{\pm}$ in Eqs. (67)-(68), (88)-(89) and (100)-(101). Here we have defined

$$(\boldsymbol{\tau}_i \times \boldsymbol{\tau}_j)_{\pm} \equiv (\boldsymbol{\tau}_i \times \boldsymbol{\tau}_j)_x \pm i(\boldsymbol{\tau}_i \times \boldsymbol{\tau}_j)_y . \quad (141)$$

Although our model for the MI electromagnetic current operator includes PS (“ π -like”), V (“ ρ -like”), SO, LL and SO2 currents, as already discussed in Section 4.1.2, we included in the weak vector current operator only the PS and V components, which are expected to give the leading contributions, as already verified in the electromagnetic case.

Among the MD terms of the weak vector current operator, the $\omega\pi\gamma$ contribution has been found negligible, while the Δ -currents have been found to give the largest MD contribution, which, however, is still small respect to that due to the leading MI terms. For the Δ -contributions, see Subsection 4.2.5.

Finally, the weak vector charge operator consists only of the “ π -like” and “ ρ -like” terms, already discussed in Section 4.1.4, which were found to give the largest two-body contributions.

4.2.3 Two-Body Weak Axial Current Operators

In contrast to the electromagnetic case, the axial current operator is not conserved. Its two-body components cannot be linked to the NN interaction and, in this sense, should be viewed as model dependent. Among the two-body axial current operators, the leading term is that associated with excitation of Δ -isobar resonances. We defer its discussion to Section 4.2.5. In the present Section we present the two-body axial current operators due to π - and ρ -meson exchanges (the πA and ρA currents, respectively), and the $\rho\pi$ -transition mechanism (the $\rho\pi A$ current). Their individual contributions have been found numerically far less important than those from Δ -excitation currents in studies of weak transitions involving light nuclei [12, 14, 51]. These studies [12, 14, 51] have also found that the πA and ρA current contributions interfere destructively, making their combined contribution almost entirely negligible. These conclusions are confirmed in the present work.

The πA , ρA , and $\rho\pi A$ current operators were first described in a systematic way by Chemtob and Rho [55]. Their derivation has been given in a number of articles, including the original reference mentioned above and the more recent

review by Towner [86]. Their momentum-space expressions are :

$$\begin{aligned} \mathbf{j}_{ij}^{(2)}(\mathbf{k}_i, \mathbf{k}_j; \pi A) &= -\frac{g_A}{2m} (\boldsymbol{\tau}_i \times \boldsymbol{\tau}_j)_{\pm} v_{\pi}(k_j) \boldsymbol{\sigma}_i \times \mathbf{k}_j \boldsymbol{\sigma}_j \cdot \mathbf{k}_j \\ &+ \frac{g_A}{m} \tau_{j,\pm} v_{\pi}(k_j) (\mathbf{q} + i \boldsymbol{\sigma}_i \times \mathbf{P}_i) \boldsymbol{\sigma}_j \cdot \mathbf{k}_j + (i \rightleftharpoons j) . \end{aligned} \quad (142)$$

$$\begin{aligned} \mathbf{j}_{ij}^{(2)}(\mathbf{k}_i, \mathbf{k}_j; \rho A) &= \frac{g_A}{2m} (\boldsymbol{\tau}_i \times \boldsymbol{\tau}_j)_{\pm} v_{\rho}(k_j) \left[\mathbf{q} \boldsymbol{\sigma}_i \cdot (\boldsymbol{\sigma}_j \times \mathbf{k}_j) + i(\boldsymbol{\sigma}_j \times \mathbf{k}_j) \times \mathbf{P}_i \right. \\ &\quad \left. - [\boldsymbol{\sigma}_i \times (\boldsymbol{\sigma}_j \times \mathbf{k}_j)] \times \mathbf{k}_j \right] \\ &+ \frac{g_A}{m} \tau_{j,\pm} v_{\rho}(k_j) \left[(\boldsymbol{\sigma}_j \times \mathbf{k}_j) \times \mathbf{k}_j - i[\boldsymbol{\sigma}_i \times (\boldsymbol{\sigma}_j \times \mathbf{k}_j)] \times \mathbf{P}_i \right] \\ &+ (i \rightleftharpoons j) . \end{aligned} \quad (143)$$

$$\begin{aligned} \mathbf{j}_{ij}^{(2)}(\mathbf{k}_i, \mathbf{k}_j; \rho \pi A) &= -\frac{g_A}{m} g_{\rho}^2 (\boldsymbol{\tau}_i \times \boldsymbol{\tau}_j)_{\pm} \frac{f_{\rho}(k_i)}{k_i^2 + m_{\rho}^2} \frac{f_{\pi}(k_j)}{k_j^2 + m_{\pi}^2} \boldsymbol{\sigma}_j \cdot \mathbf{k}_j \\ &\times \left[(1 + \kappa_{\rho}) \boldsymbol{\sigma}_i \times \mathbf{k}_i - i \mathbf{P}_i \right] + (i \rightleftharpoons j) . \end{aligned} \quad (144)$$

where the functions $v_{\pi}(k)$ and $v_{\rho}(k)$ have already been defined in Eqs. (80)–(81), and the monopole form factors are given in Eq. (71).

Note that the values used for the πNN and ρNN coupling constants and cutoff masses are the following: $f_{\pi}^2/4\pi = 0.075$, $g_{\rho}^2/4\pi = 0.5$, $\kappa_{\rho} = 6.6$, $\Lambda_{\pi} = 4.8 \text{ fm}^{-1}$, and $\Lambda_{\rho} = 6.8 \text{ fm}^{-1}$. The ρ -meson coupling constants are taken from the older Bonn OBE model [87], rather than from the more recent CD-Bonn interaction [2] ($g_{\rho}^2/4\pi = 0.81$ and $\kappa_{\rho} = 6.1$). This uncertainty has in fact essentially no impact on the results reported in the present work for two reasons. Firstly, the contribution from ρA currents, as already mentioned above, is very small. Secondly, the complete two-body axial current model, including the currents due to Δ -excitation discussed below, is constrained to reproduce the Gamow-Teller matrix element in tritium β -decay by appropriately tuning the value of the $N\Delta$ -transition axial coupling g_A^* . Hence changes in g_{ρ} and κ_{ρ} only require a slight readjustment of the g_A^* value.

4.2.4 Two-Body Weak Axial Charge Operators

The model for the two-body weak axial charge operators adopted here includes a term of pion-range as well as short-range terms associated with scalar- and

vector-meson exchanges [88]. The experimental evidence for the presence of these two-body axial charge mechanisms rests on studies of $0^+ \rightleftharpoons 0^-$ weak transitions, such as the processes $^{16}\text{N}(0^-, 120 \text{ keV}) \rightarrow ^{16}\text{O}(0^+)$ and $^{16}\text{O}(0^+) + \mu^- \rightarrow ^{16}\text{N}(0^-, 120 \text{ keV}) + \nu_\mu$, and first-forbidden β -decays in the lead region [89]. Shell-model calculations of these transitions suggest that the effective axial charge coupling of a bound nucleon may be enhanced by roughly a factor of two over its free nucleon value. There are rather strong indications that such an enhancement can be explained by two-body axial charge contributions [88].

The pion-range operator is taken as

$$\rho_{ij}^{(2)}(\mathbf{k}_i, \mathbf{k}_j; \pi A) = -i \frac{g_A}{4\bar{f}_\pi^2} (\boldsymbol{\tau}_i \times \boldsymbol{\tau}_j)_\pm \frac{f_\pi^2(k_i)}{k_i^2 + m_\pi^2} \boldsymbol{\sigma}_i \cdot \mathbf{k}_i + (i \rightleftharpoons j) , \quad (145)$$

where \bar{f}_π is the pion decay constant ($\bar{f}_\pi \simeq 93 \text{ MeV}$), \mathbf{k}_i is the momentum transfer to nucleon i , and $f_\pi(k)$ is the monopole form factor given by Eq. (71) with $\Lambda_\pi = 4.8 \text{ fm}^{-1}$. The structure and overall strength of this operator are determined by soft pion theorem and current algebra arguments [90, 91], and should therefore be viewed as “model independent”. It can also be derived, however, by considering nucleon-antinucleon pair contributions with pseudoscalar πNN coupling.

The short-range axial charge operators can be obtained in a “model-independent” way, consistently with the NN interaction model. The procedure is described in Ref. [88], and is similar to the Riska-prescription used to derive the “model-independent” electromagnetic currents. Here we consider the charge operators associated only with the central and spin-orbit components of the interaction, since they are expected to give the largest contributions, after the $\rho^{(2)}(\pi A)$ operator above. This expectation is in fact confirmed in the present study. The momentum-space expressions are given by

$$\rho_{ij}^{(2)}(\mathbf{k}_i, \mathbf{k}_j; sA) = \frac{g_A}{2m^2} [\tau_{i,\pm} \bar{v}^s(k_j) + \tau_{j,\pm} \bar{v}^{s\tau}(k_j)] \boldsymbol{\sigma}_i \cdot \mathbf{P}_i + (i \rightleftharpoons j) , \quad (146)$$

$$\begin{aligned} \rho_{ij}^{(2)}(\mathbf{k}_i, \mathbf{k}_j; vA) &= \frac{g_A}{2m^2} [\tau_{i,\pm} \bar{v}^v(k_j) + \tau_{j,\pm} \bar{v}^{v\tau}(k_j)] [\boldsymbol{\sigma}_i \cdot \mathbf{P}_j + i(\boldsymbol{\sigma}_i \times \boldsymbol{\sigma}_j) \cdot \mathbf{k}_j] \\ &- i \frac{g_A}{4m^2} (\boldsymbol{\tau}_i \times \boldsymbol{\tau}_j)_\pm \bar{v}^{v\tau}(k_j) \boldsymbol{\sigma}_i \cdot \mathbf{k}_i + (i \rightleftharpoons j) , \end{aligned} \quad (147)$$

where $\mathbf{P}_i = \mathbf{p}_i + \mathbf{p}'_i$, and

$$\bar{v}^\alpha(k) = 4\pi \int_0^\infty dr r^2 j_0(kr) \bar{v}^\alpha(r) . \quad (148)$$

with $\alpha=s, s\tau, v$, and $v\tau$. The following definitions have been introduced

$$\begin{aligned} \bar{v}^s(r) &= \frac{3}{4}v^c(r) + \frac{m^2}{2} \int_r^\infty dr' r' \left[v^b(r') - \frac{1}{2}v^{bb}(r') \right] \\ \bar{v}^v(r) &= \frac{1}{4}v^c(r) - \frac{m^2}{2} \int_r^\infty dr' r' \left[v^b(r') - \frac{1}{2}v^{bb}(r') \right] . \end{aligned} \quad (149)$$

where $v^c(r)$, $v^b(r)$ and $v^{bb}(r)$ are the isospin-independent central, spin-orbit, and $(\mathbf{L} \cdot \mathbf{S})^2$ components of the AV14 or AV18 interactions, respectively. The definitions for $\bar{v}^{s\tau}(r)$ and $\bar{v}^{v\tau}(r)$ can be obtained from those above, by replacing the isospin-independent $v^c(r)$, $v^b(r)$ and $v^{bb}(r)$ with the isospin-dependent $v^{c\tau}(r)$, $v^{b\tau}(r)$ and $v^{bb\tau}(r)$.

4.2.5 Weak Δ -Contributions

In this Subsection we review the weak current and charge operators associated with excitation of Δ isobars. A discussion of the TCO method used to include explicitly Δ -isobar degrees of freedom in the wave functions has been given in Subsection 4.1.5.

The axial current and charge operators associated with excitation of Δ isobars are modeled as

$$\mathbf{j}_i^{(1)}(\mathbf{q}; N \rightarrow \Delta, A) = -g_A^* T_{i,\pm} \mathbf{S}_i e^{i\mathbf{q} \cdot \mathbf{r}_i} , \quad (150)$$

$$\mathbf{j}_i^{(1)}(\mathbf{q}; \Delta \rightarrow \Delta, A) = -\bar{g}_A \Theta_{i,\pm} \Sigma_i e^{i\mathbf{q} \cdot \mathbf{r}_i} . \quad (151)$$

and

$$\rho_i^{(1)}(\mathbf{q}; N \rightarrow \Delta, A) = -\frac{g_A^*}{m_\Delta} T_{i,\pm} \mathbf{S}_i \cdot \mathbf{p}_i e^{i\mathbf{q} \cdot \mathbf{r}_i} , \quad (152)$$

$$\rho_i^{(1)}(\mathbf{q}; \Delta \rightarrow \Delta, A) = -\frac{\bar{g}_A}{2m_\Delta} \Theta_{i,\pm} \Sigma_i \cdot \{\mathbf{p}_i \cdot e^{i\mathbf{q} \cdot \mathbf{r}_i}\} . \quad (153)$$

where m_Δ is the Δ -isobar mass, Σ (Θ) is the Pauli operator for the Δ spin 3/2 (isospin 3/2), and $T_{i,\pm}$ and $\Theta_{i,\pm}$ are defined in analogy to Eq. (134). The

expression for $\mathbf{j}_i^{(1)}(\mathbf{q}; \Delta \rightarrow N, A)$ ($\rho_i^{(1)}(\mathbf{q}; \Delta \rightarrow N, A)$) is obtained from that for $\mathbf{j}_i^{(1)}(\mathbf{q}; N \rightarrow \Delta, A)$ ($\rho_i^{(1)}(\mathbf{q}; N \rightarrow \Delta, A)$) by Hermitian conjugation and replacing \mathbf{q} with $-\mathbf{q}$.

The coupling constants g_A^* and \bar{g}_A are not well known. In the quark-model, they are related to the axial coupling constant of the nucleon by the relations $g_A^* = (6\sqrt{2}/5)g_A$ and $\bar{g}_A = (1/5)g_A$. These values have often been used in the literature in the calculation of Δ -induced axial current contributions to weak transitions. However, given the uncertainties inherent to quark-model predictions, a more reliable estimate for g_A^* is obtained by determining its value phenomenologically to reproduce the measured Gamow-Teller matrix element in tritium β -decay [12]. This procedure is discussed in Chapter 7.

The $N \rightarrow \Delta$ and $\Delta \rightarrow \Delta$ weak vector currents are modeled, consistently with the CVC hypothesis, as

$$\mathbf{j}_i^{(1)}(\mathbf{q}; N \rightarrow \Delta, V) = -i \frac{\mu^*}{m} T_{i,\pm} \mathbf{q} \times \mathbf{S}_i e^{i\mathbf{q} \cdot \mathbf{r}_i} , \quad (154)$$

$$\mathbf{j}_i^{(1)}(\mathbf{q}; \Delta \rightarrow \Delta, V) = -i \frac{\bar{\mu}}{12m} \Theta_{i,\pm} \mathbf{q} \times \boldsymbol{\Sigma}_i e^{i\mathbf{q} \cdot \mathbf{r}_i} , \quad (155)$$

where $\mu^* \equiv \mu_{\gamma N\Delta} = 3$ n.m. and $\bar{\mu} \equiv \mu_{\gamma \Delta\Delta} = 4.35$ n.m., as given in Section 4.1.6.

Chapter 5

Trinucleon Form Factors

In the previous Chapters, we have described models for the nuclear Hamiltonian, practical computational methods for the accurate numerical calculation of wave functions, and models for the electroweak current and charge operators. A thorough testing of these models can be performed studying observables for which experimental results are available. Electron-scattering, in particular, provides an excellent tool for probing the electromagnetic structure of nuclei over a wide range of momentum transfer.

In this Chapter, we present results for the trinucleon elastic form factors, magnetic moments and magnetic and charge radii. These observables are defined in Section 5.1, while the Monte Carlo technique used to calculate them is reviewed in Section 5.2. Finally, in Section 5.3 we discuss our results, comparing them with the available experimental data.

5.1 Electron-Scattering from Nuclei

In the one-photon-exchange approximation the electron-scattering cross section involving a transition from an initial nuclear state $|J_i\rangle$ of spin J_i and rest mass m_i to a final nuclear state $|J_f\rangle$ of spin J_f , rest mass m_f and recoiling energy E_f

can be expressed in the laboratory frame as [1. 52. 92. 93]

$$\frac{d\sigma}{d\Omega} = 4\pi\sigma_M f_{\text{rec}}^{-1} \left[v_L F_L^2(q) + v_T F_T^2(q) \right] . \quad (156)$$

where

$$\sigma_M = \left(\frac{\alpha \cos\theta/2}{2\epsilon_i \sin^2\theta/2} \right)^2 . \quad (157)$$

$$v_L = \left(\frac{q_\mu^2}{q^2} \right)^2 . \quad (158)$$

$$v_T = \tan^2 \frac{\theta}{2} + \frac{q_\mu^2}{2q^2} . \quad (159)$$

and the recoil factor f_{rec} is given by

$$f_{\text{rec}} = 1 + \frac{\epsilon_f - \epsilon_i \cos\theta}{E_f} \simeq 1 + \frac{2\epsilon_i}{m_i} \sin^2 \frac{\theta}{2} . \quad (160)$$

The electron kinematical variables are defined in Fig. 10. θ is the angle between \mathbf{k}_i and \mathbf{k}_f , and q_μ^2 is defined in Eq. (60). The last expression for f_{rec} in Eq. (160)

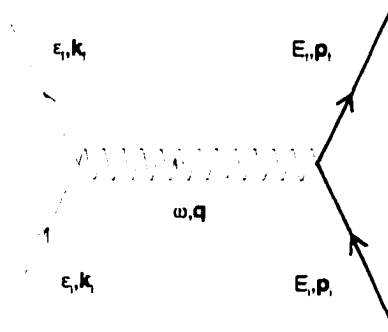


FIG. 10: Elastic scattering in one-photon exchange approximation. Solid, thick-solid and wavy lines denote respectively electrons, hadrons and photons.

is obtained by neglecting terms of order $(\omega/m_i)^2$ and higher, where

$$\frac{\omega}{m_i} = \frac{q_\mu^2 + m_f^2 - m_i^2}{2m_i^2} . \quad (161)$$

The nuclear structure information is contained in the longitudinal and transverse form factors denoted, respectively, by $F_L(q)$ and $F_T(q)$. By fixing q and ω and varying θ , it is possible to separate $F_L(q)$ from $F_T(q)$ in a procedure known as a Rosenbluth separation. Alternatively, by working at $\theta=180^\circ$ one ensures that only the transverse form factor contributes to the cross section and so may be isolated (in this case, we observe that the combination $\sigma_M \tan^2 \theta/2 \rightarrow (\alpha/2\epsilon_i)^2$ as $\theta \rightarrow 180^\circ$, and is therefore finite in this limit).

The longitudinal and transverse form factors are expressed in terms of reduced matrix elements of Coulomb (C), transverse electric (E), and transverse magnetic (M) multipole operators as [1, 52, 92, 93]

$$F_L^2(q) = \frac{1}{2J_i + 1} \sum_{J=0}^{\infty} |\langle J_f \| C_J(q) \| J_i \rangle|^2 . \quad (162)$$

$$F_T^2(q) = \frac{1}{2J_i + 1} \sum_{J=1}^{\infty} \left[|\langle J_f \| E_J(q) \| J_i \rangle|^2 + |\langle J_f \| M_J(q) \| J_i \rangle|^2 \right] . \quad (163)$$

where we have defined

$$C_{JM}(q) \equiv \int d\mathbf{x} j_J(qx) Y_{JM}(\hat{\mathbf{x}}) \rho(\mathbf{x}) . \quad (164)$$

$$E_{JM}(q) \equiv \frac{1}{q} \int d\mathbf{x} \left[\nabla \times j_J(qx) \mathbf{Y}_{J-1}^M(\hat{\mathbf{x}}) \right] \cdot \mathbf{j}(\mathbf{x}) . \quad (165)$$

$$M_{JM}(q) \equiv \int d\mathbf{x} j_J(qx) \mathbf{Y}_{J-1}^M(\hat{\mathbf{x}}) \cdot \mathbf{j}(\mathbf{x}) . \quad (166)$$

with

$$\mathbf{Y}_{JL}^M(\hat{\mathbf{x}}) \equiv \sum_{M_L, \mu} \langle LM_L, 1\mu | JM \rangle Y_{LM_L}(\hat{\mathbf{x}}) \hat{\mathbf{e}}_\mu . \quad (167)$$

$\hat{\mathbf{e}}_0 \equiv \hat{\mathbf{e}}_z$, and $\hat{\mathbf{e}}_{\pm 1} \equiv \mp(\hat{\mathbf{e}}_x \pm i\hat{\mathbf{e}}_y)/\sqrt{2}$. Here $\rho(\mathbf{x})$ and $\mathbf{j}(\mathbf{x})$ are the nuclear charge and current density operators, and $j_J(qx)$ are spherical Bessel functions. The reduced matrix elements in Eqs. (162)–(163) are related to the matrix elements of the Fourier transforms $\rho(\mathbf{q})$ and $\mathbf{j}(\mathbf{q})$, introduced in Chapter 4, via [1, 52]:

$$\begin{aligned} \langle J_f M_f | \rho(\mathbf{q}) | J_i M_i \rangle &= 4\pi \sum_{J=0}^{\infty} \sum_{M=-J}^J i^J Y_{JM}^*(\hat{\mathbf{q}}) \frac{\langle J_i M_i, JM | J_f M_f \rangle}{\sqrt{2J_f + 1}} \\ &\times \langle J_f \| C_J(q) \| J_i \rangle , \end{aligned} \quad (168)$$

$$\begin{aligned}
\langle J_f M_f | \hat{\mathbf{e}}_\lambda(\mathbf{q}) \cdot \mathbf{j}(\mathbf{q}) | J_i M_i \rangle &= -\sqrt{2\pi} \sum_{J=1}^{\infty} \sum_{M=-J}^J i^J \sqrt{2J+1} \mathcal{D}_{\lambda M}^J(-\phi_q, \theta_q, \phi_q) \\
&\times \frac{\langle J_i M_i, JM | J_f M_f \rangle}{\sqrt{2J_f+1}} \\
&\times \left[\lambda \langle J_f || M_J(q) || J_i \rangle + \langle J_f || E_J(q) || J_i \rangle \right]. \quad (169)
\end{aligned}$$

where $\lambda = \pm 1$. $\hat{\mathbf{e}}_\lambda(\mathbf{q})$ are the spherical components of the virtual photon transverse polarization vector, and the $\mathcal{D}_{\lambda M}^J$ are standard rotation matrices [93, 94]. The expressions above correspond to the virtual photon being absorbed at an angle θ_q , ϕ_q with respect to the quantization axis of the nuclear spins, the \hat{z} -axis. They can be obtained expressing the states quantized along \hat{z} as linear combinations of those quantized along $\hat{\mathbf{q}}$:

$$|J J_z\rangle_{\hat{z}} = \sum_{J'_z} D_{J'_z J_z}^J(-\phi_q, \theta_q, \phi_q) |J J'_z\rangle_{\hat{\mathbf{q}}}. \quad (170)$$

The more familiar expressions for the multipole expansion of the charge and current matrix elements are recovered by taking \mathbf{q} along the \hat{z} -axis, so that $Y_{JM}^*(\hat{\mathbf{q}}) \rightarrow \delta_{M,0} \sqrt{2J+1}/\sqrt{4\pi}$ and $\mathcal{D}_{\lambda M}^J(-\phi_q, \theta_q, \phi_q) \rightarrow \delta_{\lambda,M}$.

It is useful to consider the parity and time-reversal properties of the multipole operators [1, 52]. The scalar and polar vector character of, respectively, the charge and current density operators under parity transformations implies that C_{JM} and E_{JM} have parity $(-1)^J$, while M_{JM} has parity $(-1)^{J+1}$. The resulting selection rules are $\pi_i \pi_f = (-1)^J$ ($\pi_i \pi_f = (-1)^{J+1}$) for Coulomb and transverse electric (magnetic) transitions, where π_i and π_f are the parities of the initial and final states.

The Hermitian character of the operators $\rho(\mathbf{x})$ and $\mathbf{j}(\mathbf{x})$ as well as their transformation properties under time-reversal. $\rho(\mathbf{x}) \rightarrow \rho(\mathbf{x})$ and $\mathbf{j}(\mathbf{x}) \rightarrow -\mathbf{j}(\mathbf{x})$, can be shown to lead to the following relations:

$$\langle J_f || C_J(q) || J_i \rangle = (-1)^{J_f+J-J_i} \langle J_i || C_J(q) || J_f \rangle, \quad (171)$$

$$\langle J_f || E_J/M_J(q) || J_i \rangle = (-1)^{J_f+J-J_i+1} \langle J_i || E_J/M_J(q) || J_f \rangle. \quad (172)$$

These relations along with the parity selection rules stated above require, in particular, that elastic transitions, for which $J_f=J_i$, can only be induced by even- J

Coulomb and odd- J magnetic multipole operators.

In the case of elastic scattering from the ^3H and ^3He nuclei, for which $J_i = J_f = 1/2$, the only contributing multipoles are C_0 and M_1 , and from Eqs. (162) and (163), we obtain:

$$F_L^2(q) = \frac{1}{2} \left| \left\langle \frac{1}{2} \parallel C_0 \parallel \frac{1}{2} \right\rangle \right|^2 . \quad (173)$$

$$F_T^2(q) = \frac{1}{2} \left| \left\langle \frac{1}{2} \parallel M_1 \parallel \frac{1}{2} \right\rangle \right|^2 . \quad (174)$$

From Eqs. (168) and (169), we have that

$$\left| \left\langle \frac{1}{2} \parallel C_0 \parallel \frac{1}{2} \right\rangle \right|^2 = \frac{1}{2\pi} \left| \langle \Psi_+ | \rho(q\hat{\mathbf{z}}) | \Psi_+ \rangle \right|^2 . \quad (175)$$

$$\left| \left\langle \frac{1}{2} \parallel M_1 \parallel \frac{1}{2} \right\rangle \right|^2 = \frac{1}{\pi} \left| \langle \Psi_+ | j_x(q\hat{\mathbf{z}}) | \Psi_- \rangle \right|^2 . \quad (176)$$

where we have set \mathbf{q} along the spin-quantization axis (the z -axis). $\Psi_{+/-}$ denote the normalized trinucleon wave functions with total angular momentum projection $J_z = \pm 1/2$, respectively, and $j_x(q\hat{\mathbf{z}})$ is the x -component of the current operator.

Finally it can be shown [1, 93] that, for $q \rightarrow 0$

$$\left\langle \frac{1}{2} \parallel C_0(q) \parallel \frac{1}{2} \right\rangle \simeq \frac{Z}{\sqrt{2\pi}} . \quad (177)$$

$$\left\langle \frac{1}{2} \parallel M_1(q) \parallel \frac{1}{2} \right\rangle \simeq \frac{i}{\sqrt{\pi}} \frac{q\mu}{2m} . \quad (178)$$

where μ is the trinucleon magnetic moment in nuclear magnetons. Therefore we obtain for $q \rightarrow 0$

$$F_L(q) \rightarrow \frac{Z}{\sqrt{4\pi}} . \quad (179)$$

$$F_T(q) \rightarrow \frac{1}{\sqrt{2\pi}} \frac{q\mu}{2m} . \quad (180)$$

The magnetic and charge form factors are then defined as

$$F_C(q) \equiv \frac{\sqrt{4\pi}}{Z} F_L(q) . \quad (181)$$

$$F_M(q) \equiv \sqrt{2\pi} \frac{2m}{q\mu} F_T(q) . \quad (182)$$

so that $F_{C/M}(q = 0) = 1$. From Eqs. (173)–(176), (181) and (182), we obtain that

$$F_M(q) = \frac{2m}{\mu} \frac{1}{q} \langle \Psi_+ | j_x(q\hat{\mathbf{z}}) | \Psi_- \rangle . \quad (183)$$

$$F_C(q) = \frac{1}{Z} \langle \Psi_+ | \rho(q\hat{\mathbf{z}}) | \Psi_+ \rangle . \quad (184)$$

The charge and magnetic radii $\langle r_C^2 \rangle$ and $\langle r_M^2 \rangle$ are finally defined by the relation

$$F_{C/M}(q) \simeq 1 - \frac{q^2 \langle r_{C/M}^2 \rangle}{6} . \quad (185)$$

which can be easily obtained from the the definitions of the form factors in the limit $q \rightarrow 0$, keeping the leading and next-to-leading order term in the expansion of the Bessel functions in Eqs. (164)–(166). The charge and magnetic radii as defined above are proportional to the “slopes” of the form factors at $q^2 = 0$.

5.2 Calculation Details

The matrix elements of the charge and current operators of Eqs. (183) and (184) are evaluated, without any approximation, by Monte Carlo integration based on the Metropolis *et al.* algorithm [95]. We describe here the main steps of the method. For more details see Refs. [67, 73, 76]. A proof of the Metropolis algorithm is given in Ref. [93]. We proceed as follows: (i) from a given starting spatial configuration of the three nucleons $\mathbf{R}_0 = (\mathbf{r}_1, \mathbf{r}_2, \mathbf{r}_3)$, we generate randomly the configuration $\mathbf{R}' = (\mathbf{r}'_1, \mathbf{r}'_2, \mathbf{r}'_3)$. (ii) The probability density $W(\mathbf{R})$ for any given \mathbf{R} is defined as

$$W(\mathbf{R}) \propto \frac{1}{2} \left(\langle \Psi_-^\dagger(\mathbf{R}) \Psi_-(\mathbf{R}) \rangle + \langle \Psi_+^\dagger(\mathbf{R}) \Psi_+(\mathbf{R}) \rangle \right) . \quad (186)$$

where the notation $\langle \dots \rangle$ implies sums over the spin-isospin states of the wave functions Ψ_\pm . (iii) We calculate the ratio

$$r \equiv \frac{W(\mathbf{R}')}{W(\mathbf{R}_0)} , \quad (187)$$

and generate a random number a between 0 and 1. If $a \leq r$, then \mathbf{R}' is accepted, otherwise is rejected. (iv) The procedure is repeated N times and the

accepted spatial configurations are stored. (v) For each of them, the state vectors $j_x(q\hat{\mathbf{z}}) |\Psi_- \rangle$ and $\rho(q\hat{\mathbf{z}}) |\Psi_+ \rangle$ are calculated, by performing exactly the spin-isospin algebra, as described in Refs. [67, 73, 76]. The momentum-dependent terms in $j_x(q\hat{\mathbf{z}})$ and $\rho(q\hat{\mathbf{z}})$ are calculated numerically; for example

$$\nabla_{i,\alpha} \Psi(\mathbf{R}) = \frac{1}{2\delta_{i,\alpha}} [\Psi(\mathbf{R} + \delta_{i,\alpha}) - \Psi(\mathbf{R} - \delta_{i,\alpha})] . \quad (188)$$

where $\delta_{i,\alpha}$ is a small increment in the $r_{i,\alpha}$ component of \mathbf{R} . (vi) The spatial integral is then given by (for $j_x(q\hat{\mathbf{z}})$, as an example)

$$\begin{aligned} \int d\mathbf{r}_1 d\mathbf{r}_2 d\mathbf{r}_3 \Psi_+^\dagger(\mathbf{r}_1 \mathbf{r}_2 \mathbf{r}_3) j_x(q\hat{\mathbf{z}}) \Psi_-(\mathbf{r}_1 \mathbf{r}_2 \mathbf{r}_3) \simeq \\ \frac{1}{N} \sum_{p=1}^N \frac{1}{W(\mathbf{R}_p)} \langle \Psi_+^\dagger(\mathbf{R}_p) j_x(q\hat{\mathbf{z}}) \Psi_-(\mathbf{R}_p) \rangle . \end{aligned} \quad (189)$$

where the spin-isospin dependence is understood.

The statistical error is proportional to $1/\sqrt{N}$. Typically, in the trinucleon form factor calculation reported here, 400,000 configurations are enough to achieve a relative error of a few % at low and moderate values of momentum transfer q ($q \leq 5 \text{ fm}^{-1}$), increasing to $\sim 30\%$ at the highest q -values.

The evaluation of the matrix element of Eq. (183) when also Δ -isobar degrees of freedom are considered, is more complicated. In this case, it is convenient to expand the full wave function $\Psi_{N+\Delta, J_z}$ as

$$\Psi_{N+\Delta, J_z} = \Psi_{J_z} + \sum_{i < j} U_{ij}^{TR} \Psi_{J_z} + \dots . \quad (190)$$

and write, in a schematic notation:

$$\langle \Psi_{N+\Delta, f} | j | \Psi_{N+\Delta, i} \rangle = \langle \Psi_f | j(N \text{ only}) | \Psi_i \rangle + \langle \Psi_f | j(\Delta) | \Psi_i \rangle . \quad (191)$$

where $j(N \text{ only})$ denotes all one- and two-body contributions to $\mathbf{j}(\mathbf{q})$ which only involve nucleon degrees of freedom, i.e., $j(N \text{ only}) = j^{(1)}(N \rightarrow N) + j^{(2)}(NN \rightarrow NN)$. The operator $j(\Delta)$ includes terms involving the Δ -isobar degrees of freedom, associated with the explicit Δ currents $j^{(1)}(N \rightleftharpoons \Delta)$, $j^{(1)}(\Delta \rightarrow \Delta)$, $j^{(2)}(NN \rightleftharpoons N\Delta)$, and with the transition operators U_{ij}^{TR} introduced in Subsection 4.1.5. The operator $j(\Delta)$ is illustrated diagrammatically in Figs. 11 and 12.

The terms (a)–(g) in Fig. 11 and (a)–(f) in Fig. 12 are two-body current operators. The terms (g)–(l) in Fig. 12 are three-body current operators, while the terms (f) and (h)–(j) in Fig. 11 are to be interpreted as renormalization corrections to the “nucleonic” matrix elements $\langle \Psi_f | j(N\text{only}) | \Psi_i \rangle$, due to the presence of Δ -admixture in the wave functions.

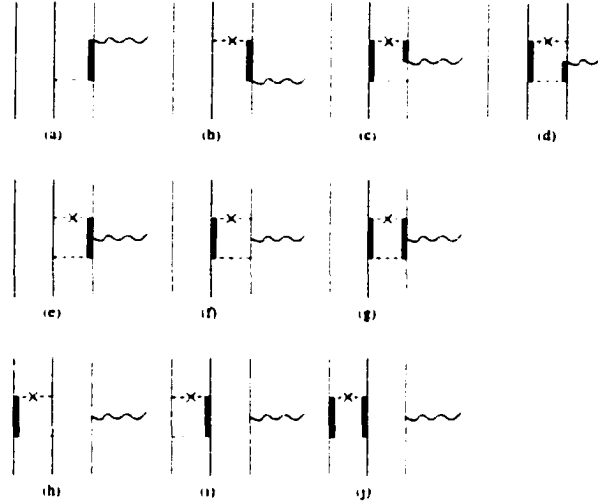


FIG. 11: Diagrammatic representation of operators included in $j(\Delta)$ due to one-body currents $j^{(1)}(N \rightarrow \Delta)$, $j^{(1)}(\Delta \rightarrow \Delta)$, etc., transition correlations $U^{N\Delta}$, $U^{\Delta\Delta}$, and corresponding Hermitian conjugates. Wavy, thin, thick, dashed and cross-dashed lines denote photons, nucleons, Δ -isobars and transition correlations $U^{BB'}$ and $U^{BB'\dagger}$, respectively.

There are, however, additional, connected three-body terms in $j(\Delta)$ that are neglected in the present work. A number of these are illustrated in Fig. 13. Their contribution is expected to be significantly smaller than that from the terms in Figs. 11 and 12 involving transition correlations between two particles only, of the type $U_{ij}^{BB'\dagger} U_{ij}^{BB'}$, but comparable to that from the three-body terms in Fig. 12 having $U_{ij}^{BB'\dagger} U_{jk}^{BB'}$. These have been found to be very small.

The terms in Fig. 11 are expanded as operators acting on the nucleons' coordinates. For example, the terms (a) and (e) in Fig. 11 have the structure, respectively,

$$(a) = j_i^{(1)}(\Delta \rightarrow N) U_{ij}^{\Delta N}, \quad (192)$$

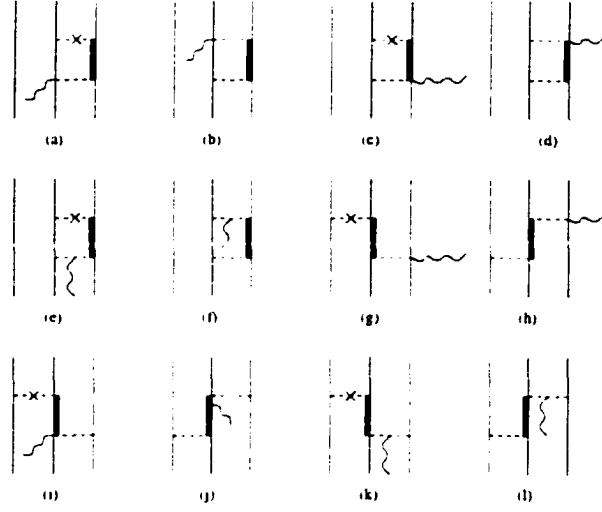


FIG. 12: Diagrammatic representation of operators included in $j(\Delta)$ due to two-body currents $j^{(2)}(NN \rightarrow N\Delta)$, $j^{(2)}(NN \rightarrow \Delta N)$, etc., transition correlations $U^{N\Delta}$, $U^{\Delta\Delta}$, and corresponding Hermitian conjugates. Wavy, thin, thick, dashed and cross-dashed lines denote photons, nucleons, Δ -isobars and transition correlations $U^{BB'}$ and $U^{BB'\dagger}$, respectively.

$$(e) = U_{ij}^{\Delta N\dagger} j_i^{(1)}(\Delta \rightarrow \Delta) U_{ij}^{\Delta N}. \quad (193)$$

which can be reduced to operators involving only Pauli spin and isospin matrices by using the identities

$$\mathbf{S}^\dagger \cdot \mathbf{A} \mathbf{S} \cdot \mathbf{B} = \frac{2}{3} \mathbf{A} \cdot \mathbf{B} - \frac{i}{3} \boldsymbol{\sigma} \cdot (\mathbf{A} \times \mathbf{B}), \quad (194)$$

$$\begin{aligned} \mathbf{S}^\dagger \cdot \mathbf{A} \boldsymbol{\Sigma} \cdot \mathbf{B} \mathbf{S} \cdot \mathbf{C} &= \frac{5}{3} i \mathbf{A} \cdot (\mathbf{B} \times \mathbf{C}) - \frac{1}{3} \boldsymbol{\sigma} \cdot \mathbf{A} \mathbf{B} \cdot \mathbf{C} \\ &\quad - \frac{1}{3} \mathbf{A} \cdot \mathbf{B} \mathbf{C} \cdot \boldsymbol{\sigma} + \frac{4}{3} \mathbf{A} \cdot (\mathbf{B} \cdot \boldsymbol{\sigma}) \mathbf{C}. \end{aligned} \quad (195)$$

where \mathbf{A} , \mathbf{B} and \mathbf{C} are vector operators that commute with $\boldsymbol{\sigma}$, but not necessarily among themselves.

While the terms in Fig. 12 could have been reduced in precisely the same way, the resulting expressions in terms of $\boldsymbol{\sigma}$ and $\boldsymbol{\tau}$ Pauli matrices become too cumbersome. Thus, for these it was found to be more convenient to retain the explicit representation of \mathbf{S} (\mathbf{S}^\dagger) as a 4×2 (2×4) matrix

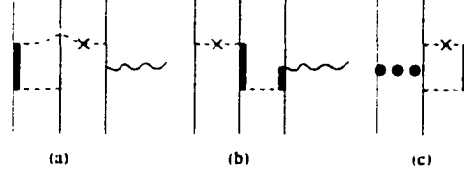


FIG. 13: Diagrams associated with connected three-body terms, which are neglected in the present work. Wavy, thin, thick, dashed, cross-dashed and dotted lines denote photons, nucleons, Δ -isobars, transition correlations $U^{BB'}$ and $U^{BB'\dagger}$, and the two-body current $j^{(2)}(NN \rightarrow N\Delta)$, respectively.

$$S = \begin{pmatrix} -\hat{e}_- & 0 \\ \sqrt{\frac{2}{3}}\hat{e}_0 & -\frac{1}{\sqrt{3}}\hat{e}_- \\ -\frac{1}{\sqrt{3}}\hat{e}_+ & \sqrt{\frac{2}{3}}\hat{e}_0 \\ 0 & -\hat{e}_+ \end{pmatrix}.$$

where $\hat{e}_{\pm} = \mp(\hat{x} \pm i\hat{y})/\sqrt{2}$, $\hat{e}_0 = \hat{z}$, and $\hat{e}_{\mu}^* = (-)^{\mu}\hat{e}_{-\mu}$ and derive the result of terms such as (a)+(c)+(e) = $U_{ij}^{N\Delta\dagger} j_{ij}^{(2)}(NN \rightarrow N\Delta)$ on the state $|\Psi\rangle$ by first operating with $j^{(2)}$ and then with $U^{N\Delta\dagger}$. The Monte Carlo evaluation of the matrix element is then performed with methods similar to those described above.

We finally note that perturbation theory (PT) estimates of the Δ -isobar excitation currents in photo- and electro-nuclear observables typically include only the contribution from single $N \rightleftharpoons \Delta$ transitions (namely diagrams (a) and (b) in Fig. 11) and ignore the change in the wave function normalization. In particular, the PT expressions for the three-body terms in Fig. 12, diagrams (g)-(l) along with those in which the first and third legs are exchanged, can easily be shown to satisfy current conservation with the Fujita-Miyazawa two-pion exchange three-nucleon interaction (2π TNI) [37] described in Chapter 2, which provides the “long-range” component of the three-nucleon interaction.

5.3 Results

In this Section we present results for the magnetic moments, charge and magnetic form factors and radii of ^3H and ^3He . In Subsection 5.3.1 we present the results obtained when only the nucleonic degrees of freedom are considered, while in Subsection 5.3.2 we present the results obtained by including also the Δ -isobar degrees of freedom. The nuclear ground states are described by the PHH wave functions obtained from the AV18/UIX Hamiltonian model. A discussion of the electromagnetic current and charge operators has been given in Chapter 4.

5.3.1 Nucleons Only

We present here our results for the magnetic and charge form factors when purely nucleonic wave functions are used.

The Magnetic Form Factors

The current operator includes, in addition to the one-body current in Eq. (54), the model-independent (MI) two-body currents PS, V, SO, LL and SO2, obtained from the charge-independent part of the AV18 interaction, the model-dependent (MD) $\rho\pi\gamma$ and $\omega\pi\gamma$ two-body currents, and finally the local terms of the $\pi\pi_S$ three-body current associated with the S-wave two-pion exchange three-nucleon interaction of Eq. (93). Because of destructive interference between the S- and D-state components of the wave function, the one-body predictions for the ^3H and ^3He magnetic form factors (MFF) have distinct minima at around $\sim 3.5 \text{ fm}^{-1}$ and $\sim 2.5 \text{ fm}^{-1}$, respectively, in disagreement with the experimental data [96, 97, 98, 99, 100, 101, 102, 103, 104, 105], as shown in Fig. 14. Inclusion of the contributions from the two- and $\pi\pi_S$ three-body currents shifts the zeros in the calculated MFF to higher q -values. While the experimental ^3H MFF is in good agreement with theory over a wide range of momentum transfers, there is a significant discrepancy between the measured and calculated values of the ^3He MFF in the region of the first diffraction minimum. As pointed out already in Chapter 4, this calculation is affected by the rather poor knowledge of the

neutron electromagnetic form factors. In Fig. 14 we show also the results obtained with the Gari-Krümpelmann (GK) parametrization [106] of the nucleon electromagnetic form factors, to check whether this discrepancy between theory and experiment persists when different parametrizations of the nucleon electromagnetic form factors are used. No improvement in describing the experimental results has been found. To fully investigate this aspect, however, the most recent results for the nucleon (in particular proton) electromagnetic form factors [107] should be considered.

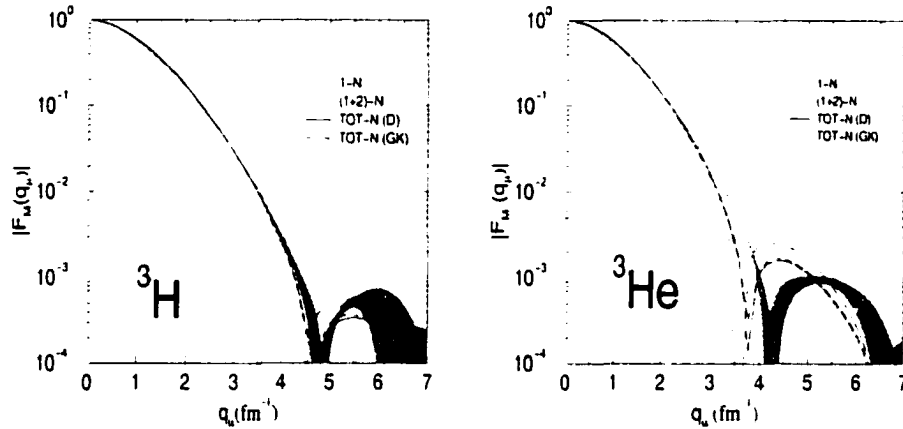


FIG. 14: The magnetic form factors of ^3H and ^3He , obtained with single-nucleon currents (1-N), and with inclusion of two-nucleon current ((1+2)-N) and $\pi\pi_S$ three-nucleon (TOT-N(D)) current contributions, are compared with data (shaded area) from Amroun *et al.* [105]. Theoretical results correspond to the AV18/UIX PHH wave functions, and employ the dipole parametrization (including the Galster factor for $G_E(q_\mu^2)$) for the nucleon electromagnetic form factors. Note that the Sachs form factor $G_E^V(q_\mu^2)$ is used in the model-independent isovector two-body currents obtained from the charge-independent part of the AV18 interaction. Also shown are the total results corresponding to the Gari-Krümpelmann parametrization [106] of the nucleon electromagnetic form factor (TOT-N(GK)).

To have a better insight into the electromagnetic current operator and the structure of the three-nucleon systems, it is useful to define the quantities

$$F_M^{S,V}(q) = \frac{1}{2} [\mu(^3\text{He}) F_M(q; ^3\text{He}) \pm \mu(^3\text{H}) F_M(q; ^3\text{H})] . \quad (196)$$

where $\mu(^3\text{He})$ and $\mu(^3\text{H})$ are the magnetic moments of ^3He and ^3H respectively. In fact, if the ^3H and ^3He ground states were pure $T=1/2$ states, then the F_M^S and F_M^V linear combinations of the three-nucleon MFF would be only influenced by, respectively, the isoscalar (S) and isovector (V) parts of the current operator. For example, the one-body current has the isospin structure

$$j_i^{(1)} = j_i^S + j_i^V \tau_{i,z} . \quad (197)$$

From Eq. (196), using the definition of Eq. (183), we obtain

$$F_M^S(q) \propto \langle \sum_i j_i^S \rangle , \quad (198)$$

$$F_M^V(q) \propto \langle \sum_i j_i^V \rangle , \quad (199)$$

in a schematic notation. However, the ^3H and ^3He ground states are not pure $T=1/2$ states; in fact, the electromagnetic and isospin-symmetry breaking terms present in the AV18 interaction, generate small isospin admixtures with $T > 1/2$. As a consequence, purely isoscalar (isovector) current operators give small, otherwise vanishing, contributions to the F_M^V (F_M^S) MFF.

Among the two- and three-body current operators described in Chapter 4, the PS, V, $\omega\pi\gamma$ and $\pi\pi_S$ currents are purely isovector, while $\rho\pi\gamma$ is purely isoscalar. As already pointed out in Section 4.1.2, the momentum-dependent currents SO, LL, SO2 have both isoscalar and isovector terms. The one-body current has also, as already discussed, both isoscalar and isovector components.

The contributions of the individual components of the two- and three-nucleon ($\pi\pi_S$ term) currents to the F_M^S and F_M^V combinations are shown in Fig. 15. In the diffraction region the PS isovector current gives the dominant contribution to F_M^V , while the contributions from remaining currents are about one order of magnitude or more smaller. The $\pi\pi_S$ current is found to give a very small correction.

Among the two-body contributions to F_M^S , the most important is that due to the SO currents, the remaining operators producing a very small correction. Note that the isovector PS and V currents contribute to F_M^S because of the small isospin-symmetry breaking components present in the ^3H and ^3He wave functions induced by the AV18 model, as mentioned earlier.

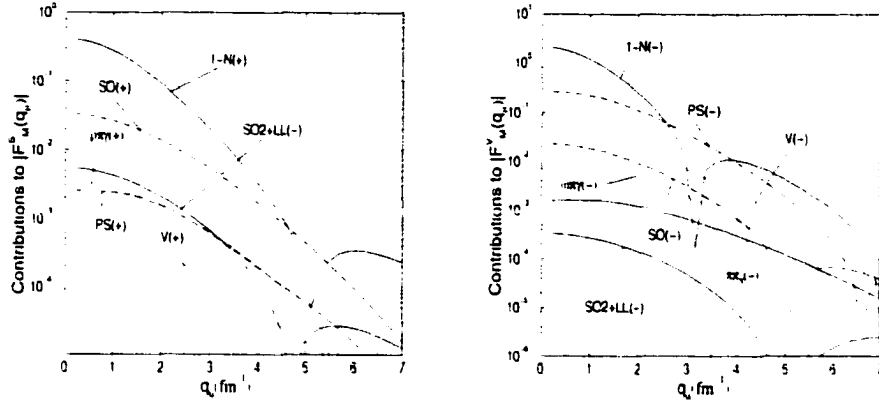


FIG. 15: Individual contributions to the $F_M^S(q_\mu)$ and $F_M^V(q_\mu)$ combinations, Eq. (196), of the ${}^3\text{H}$ and ${}^3\text{He}$ magnetic form factors, obtained with the dipole parametrization of the nucleon electromagnetic form factors. The sign of each contribution is given in parenthesis. Note that, because of isospin-symmetry breaking components present in the ${}^3\text{H}$ and ${}^3\text{He}$ wave functions, the purely isoscalar PS, V and $\pi\pi_S$ currents (purely isoscalar $\rho\pi\gamma$ current) give non vanishing contributions to the $F_M^S(q_\mu)$ ($F_M^V(q_\mu)$) combination. However as the $\pi\pi_S$ ($\rho\pi\gamma$) contribution is very small, is not shown.

Finally, the cumulative contributions to the F_M^S and F_M^V combinations are compared with the experimental data [105] in Fig. 16. The isoscalar form factor $F_M^S(q)$ is rather poorly known, especially at higher q -values. Some discrepancies are present between the full calculation (curve labelled TOT-N) and the experimental results at moderate q -values. For the isovector form factor F_M^V , the zero is calculated to occur at lower q -value than experimentally observed. As shown in the next Section, this discrepancy between theory and experiment remains unresolved even when Δ -isobar degrees of freedom are included in both the nuclear wave functions and currents.

Predictions for the magnetic moments are given in Tables VII and VIII, while those for the magnetic radii are listed in Table IX. These results are discussed in Subsection 5.3.2.

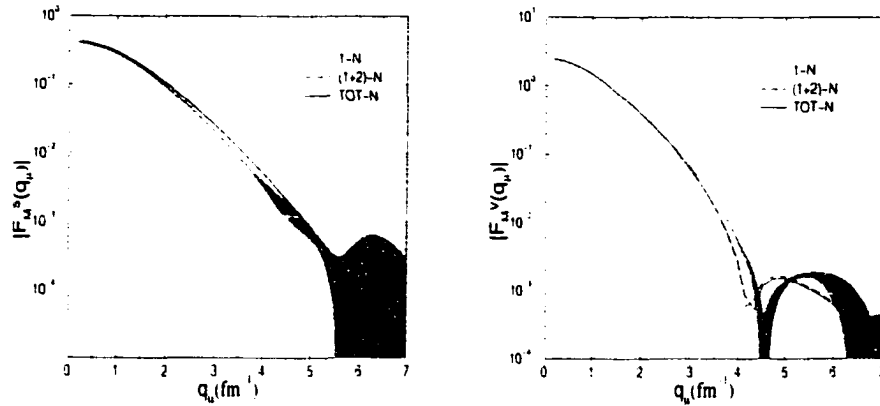


FIG. 16: The $F_M^S(q_\mu)$ and $F_M^V(q_\mu)$ combinations of the ^3H and ^3He magnetic form factors, obtained with single-nucleon currents (1-N), and with inclusion of two-nucleon current ((1+2)-N) and $\pi\pi_S$ three-nucleon current (TOT-N) contributions, are compared with data (shaded area) from Amroun *et al.* [105]. The dipole parametrization is used for the nucleon electromagnetic form factors.

The Charge Form Factors

The charge operator includes, in addition to the one-body term of Eq. (55), the PS, V, ω , $\rho\pi\gamma$ and $\omega\pi\gamma$ two-body operators, discussed in Chapter 4. The calculated ^3H and ^3He charge form factors (CFF) are compared with the experimental data [96, 97, 98, 99, 100, 101, 102, 103, 104, 105] in Fig. 17. There is excellent agreement between theory and experiment, as is clear from this figure. The important role of the two-body contributions above 3 fm^{-1} is also evident. The remarkable success of the present picture based on non-relativistic wave functions and a charge operator including the leading relativistic corrections should be stressed. It suggests, in particular, that the present model for the two-body charge operator is better than one *a priori* should expect. These operators, such as the PS charge operator, fall into the class of relativistic corrections. Thus, evaluating their matrix elements with non-relativistic wave functions represents only the first approximation to a systematic reduction. A consistent treatment

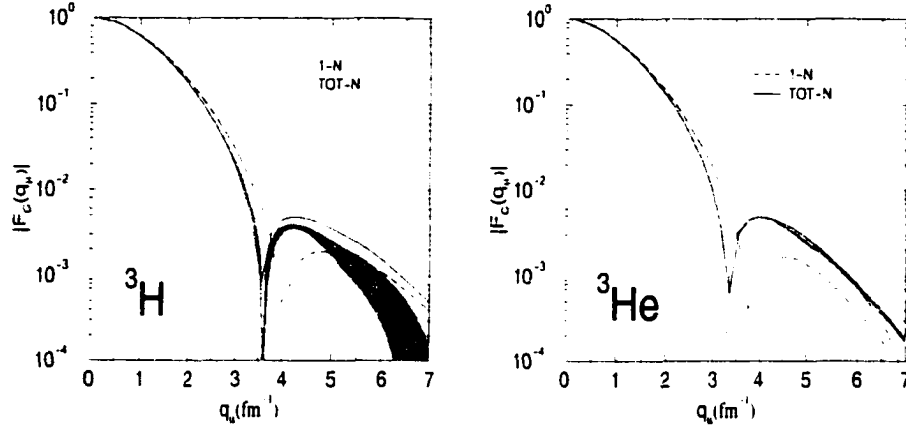


FIG. 17: The charge form factors of ${}^3\text{H}$ and ${}^3\text{He}$, obtained with a single-nucleon charge operator (1-N) and with inclusion of two-nucleon charge operator contributions (TOT-N), are compared with data (shaded area) from Amroun *et al.* [105]. Note that the 1-N results also include the Darwin-Foldy and spin-orbit corrections. Theoretical results correspond to the AV18/UIX PHH wave functions, and employ the dipole parametrization of the nucleon electromagnetic form factors.

of these relativistic effects would require, for example, inclusion of the boost corrections on the nuclear wave functions [71, 72, 108]. Yet, the excellent agreement between the calculated and measured CFF suggests that these corrections may be negligible in the q -range explored so far.

For completeness, we show in Fig. 18 the contributions from the individual components of the charge operator to the isoscalar (S) and isovector (V) form factors, defined, similarly to Eq. (196), as

$$F_C^{S,V}(q) = \frac{1}{2} \left[2 F_C(q; {}^3\text{He}) \pm F_C(q; {}^3\text{H}) \right]. \quad (200)$$

$$\text{Sin} \quad F_C^{S,V}(q) = \frac{1}{2} \left[2 F_C(q; {}^3\text{He}) \pm F_C(q; {}^3\text{H}) \right]. \quad (200)$$

not

Similar observations to the ones made for $F_M^{S/V}(q)$ are valid also for $F_C^{S,V}(q)$. We respectively, purely isovector and isoscalar.

Finally, values for the charge radii of ${}^3\text{H}$ and ${}^3\text{He}$ are listed in Table VI. The results including the contributions associated with the two-body charge operators

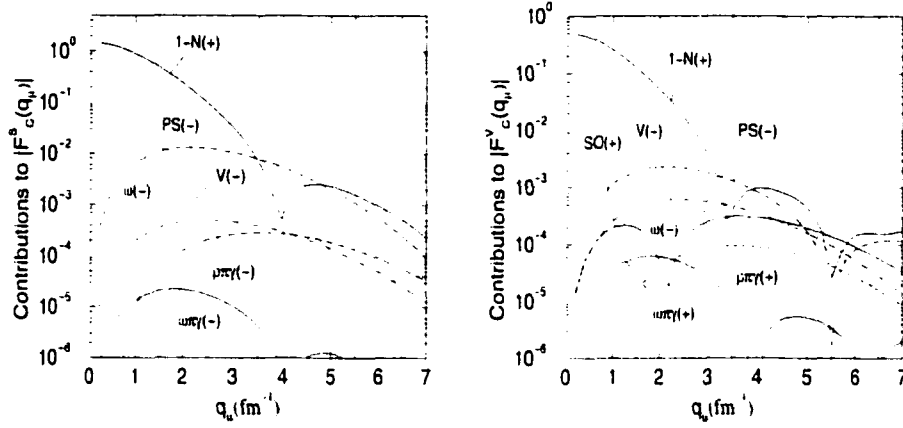


FIG. 18: Individual contributions to the $F_C^S(q_\mu)$ and $F_C^V(q_\mu)$ combinations, Eq. (200), of the ${}^3\text{H}$ and ${}^3\text{He}$ charge form factors, obtained with the dipole parametrization of the nucleon electromagnetic form factors. The sign of each combination is given in parenthesis. Note that, because of isospin-symmetry breaking components present in the ${}^3\text{H}$ and ${}^3\text{He}$ wave functions, the purely isovector $\omega\pi\gamma$ (isoscalar $\rho\pi\gamma$) charge operator gives a non vanishing contribution to the $F_C^S(q_\mu)$ ($F_C^V(q_\mu)$) combination.

are found to be in excellent agreement with experimental data.

5.3.2 Nucleons and Δ 's

The ${}^3\text{H}$ and ${}^3\text{He}$ magnetic form factors obtained by including nucleon and Δ -isobar degrees of freedom in the nuclear wave functions and currents are shown in Fig. 19; individual contributions to the combinations F_M^S and F_M^V are displayed in Fig. 20. Finally, individual and cumulative contributions to the magnetic moments and cumulative contributions to the magnetic radii of the trinucleons are listed in Tables VII, VIII and IX, respectively. Note that in Fig. 20 and Table VII the contributions labelled 1- Δ and 2- Δ are associated with the diagrams in Figs. 11 and 12, respectively. Also note that the individual nucleonic and Δ -isobar contributions in Fig. 20 and Table VII are normalized as, in a schematic

TABLE VI: Cumulative and normalized contributions to the ${}^3\text{H}$ and ${}^3\text{He}$ r.m.s. charge radii, in fm, compared with the experimental data.

	${}^3\text{H}$	${}^3\text{He}$
1-N	1.711	1.919
TOT	1.725	1.928
expt.	1.755 ± 0.086	1.959 ± 0.030

notation,

$$[O] = \frac{\langle \Psi | j_O | \Psi \rangle}{\langle \Psi | \Psi \rangle}. \quad (201)$$

However, the cumulative contributions in Fig. 19 and Table VIII and IX are normalized as

$$[\text{TOT}-\text{N}] = \frac{\langle \Psi | j(N \text{ only}) | \Psi \rangle}{\langle \Psi | \Psi \rangle}. \quad (202)$$

when “nucleons only” terms are retained, and as

$$[\text{TOT}-(\text{N} + \Delta)] = \frac{\langle \Psi_{N+\Delta} | j(N + \Delta) | \Psi_{N+\Delta} \rangle}{\langle \Psi_{N+\Delta} | \Psi_{N+\Delta} \rangle}. \quad (203)$$

when, in addition, the Δ terms are included. This last expression takes into account the change in wave function normalization induced when the Δ -admixture are included.

The MFF of ${}^3\text{H}$ and ${}^3\text{He}$, when the full model for the current operator is used (curves labelled TOT-(N+ Δ)) are in rather good agreement with experiment up to q -values of $\simeq 4 \text{ fm}^{-1}$ and $\simeq 3 \text{ fm}^{-1}$, respectively. The discrepancy between theory and experiment, especially in the ${}^3\text{He}$ MFF first diffraction region, remains unsolved. In fact, the Δ -contributions have been found to be rather small, as can be seen in Fig. 19 comparing the curves labelled TOT-N and TOT-(N+ Δ), and in Fig. 20, comparing the 1-N with the 1- Δ and 2- Δ contributions. This is in contrast with earlier studies [109], where it was suggested that the inclusion of Δ -isobar degrees of freedom could reproduce the experimental data in the region of the first zero. In fact, the 2- Δ contribution obtained in that study [109] had the wrong sign (opposite to that obtained here).

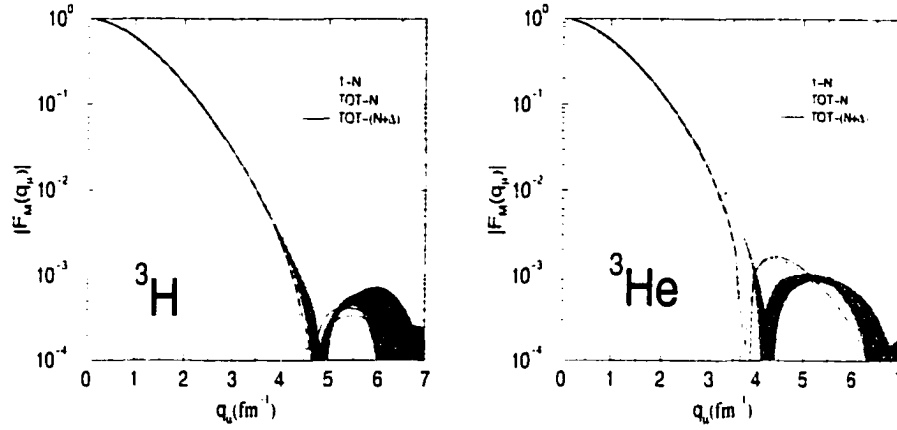


FIG. 19: The magnetic form factors of ${}^3\text{H}$ and ${}^3\text{He}$, obtained with single-nucleon currents (1-N), and with inclusion of two- and three-nucleon current (TOT-N) and Δ (TOT-(N+ Δ)) contributions.

The predicted magnetic moments of the trinucleons are within less than 1% of the experimental values. The predominantly isovector Δ -isobar contributions lead to an increase (in magnitude) of the ${}^3\text{H}$ and ${}^3\text{He}$ magnetic moments calculated with nucleons only degrees of freedom of, respectively, 1.1% and 1.7%. We note that perturbation theory estimates of the Δ -isobar contributions are found to be significantly larger than obtained here [67].

The predicted magnetic radii of ${}^3\text{H}$ and ${}^3\text{He}$ are, respectively, 2% and 3% smaller than the experimental values, but still within experimental errors. Inclusion of the contributions due to two- and three-body exchange currents leads to a decrease of the ${}^3\text{H}$ and ${}^3\text{He}$ magnetic radii by, respectively, 5% and 6%.

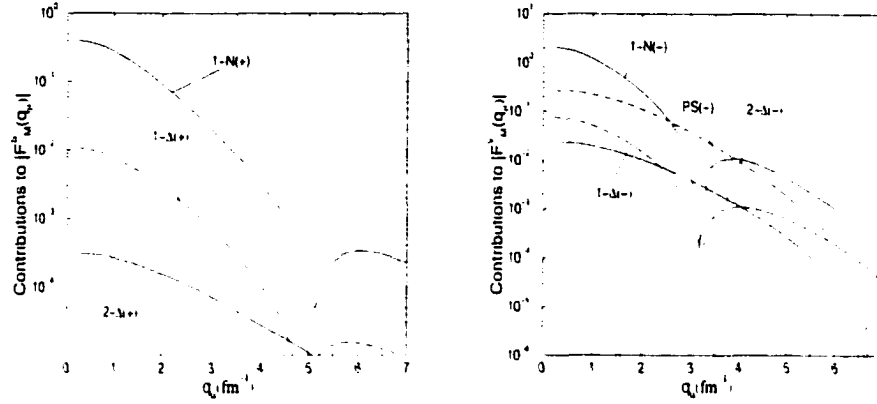


FIG. 20: The single-nucleon contribution to the $F_M^S(q_\mu)$ and $F_M^V(q_\mu)$ combination of the ${}^3\text{H}$ and ${}^3\text{He}$ magnetic form factors is compared with the 1- Δ and 2- Δ contributions, associated respectively with diagrams of Fig. 11 and 12.

TABLE VII: Individual contributions from the different components of the nuclear electromagnetic current operator to the ${}^3\text{H}$ and ${}^3\text{He}$ magnetic moments and their μ_S and μ_V combinations, in nuclear magnetons (n.m.). Note that, because of isospin-symmetry breaking components present in the PHH ${}^3\text{H}$ and ${}^3\text{He}$ wave functions, purely isoscalar (isovector) currents give non vanishing contributions to the μ_V (μ_S) combination. The contributions to μ_S due to the $\pi\pi_S$ and 2- Δ currents and those to μ_V due to the SO2+LL currents are very small and are not listed.

	$\mu({}^3\text{H})$	$\mu({}^3\text{He})$	μ_S	μ_V
1-N	2.571	-1.757	0.407	2.164
PS	0.274	-0.269	0.002	0.271
V	0.046	-0.044	0.001	0.045
SO	0.057	0.010	0.033	0.023
SO2+LL	-0.005	-0.006	-0.005	
$\rho\pi\gamma + \omega\pi\gamma$	0.016	-0.009	0.003	0.012
$\pi\pi_S$	0.002	-0.002		0.002
1- Δ	0.084	-0.064	0.010	0.074
2- Δ	0.024	-0.024		0.024

TABLE VIII: Cumulative and normalized contributions to the ${}^3\text{H}$ and ${}^3\text{He}$ magnetic moments and their μ_S and μ_V combinations, in nuclear magnetons (n.m.), compared with the experimental data.

	$\mu({}^3\text{H})$	$\mu({}^3\text{He})$	μ_S	μ_V
1-N	2.571	-1.757	0.407	2.164
TOT-N	2.961	-2.077	0.442	2.519
TOT-N+1- Δ	2.971	-2.089	0.441	2.530
TOT-(N+ Δ)	2.994	-2.112	0.441	2.553
expt.	2.979	-2.127	0.426	2.553

TABLE IX: Cumulative and normalized contributions to the ${}^3\text{H}$ and ${}^3\text{He}$ r.m.s. magnetic radii, in fm, compared with the experimental data.

	${}^3\text{H}$	${}^3\text{He}$
1-N	1.895	2.040
TOT-N	1.810	1.925
TOT-N+1- Δ	1.804	1.916
TOT-(N+ Δ)	1.800	1.909
expt.	1.840 ± 0.181	1.965 ± 0.153

Chapter 6

The ^3He Threshold Electrodisintegration

Radiative capture, photodisintegration and electrodisintegration reactions are other useful tools for exploring the structure of nuclei and their electromagnetic responses, besides elastic electron-scattering. In the particular case of the three-nucleon systems, there is a large body of experimental results for pd radiative fusion and ^3He photodisintegration and electrodisintegration at threshold. For the ^3He electrodisintegration reaction, however, the data are still quite uncertain. A systematic study of these processes using AV18/UIX PHH wave functions and including one- and two-body components in the model of the electromagnetic transition operators, has been performed in Ref. [15].

In this Chapter we limit our discussion to the ^3He threshold electrodisintegration reaction. In Section 6.1 we define the observables of interest for the reaction $^3\text{He}(\vec{e}, e')pd$ at threshold. In Section 6.2 we list the terms included in the electromagnetic current and charge operators and describe some calculation details. Finally in Section 6.3 we present and discuss our results.

6.1 The ${}^3\text{He}(\vec{e}, e')pd$ Reaction at Threshold

The inclusive cross section for polarized electron scattering from a polarized spin 1/2 target can be written as [15, 110]

$$\frac{d^3\sigma}{d\Omega d\omega} = \Sigma(q, \omega) + h \Delta(q, \omega) . \quad (204)$$

$$\Sigma(q, \omega) = \sigma_M [v_L R_L(q, \omega) + v_T R_T(q, \omega)] , \quad (205)$$

$$\Delta(q, \omega) = \sigma_M [v_{LT'} R_{LT'}(q, \omega) \sin \theta^* \cos \phi^* + v_{T'} R_{T'}(q, \omega) \cos \theta^*] , \quad (206)$$

where σ_M is the Mott cross section defined in Eq. (157), the coefficients v_α are functions of the electron kinematic variables, $h = \pm 1$ is the helicity of the incident electron, and the angles θ^* and ϕ^* specify the direction of the target polarization with respect to $\hat{\mathbf{q}}$, see Fig. 21.

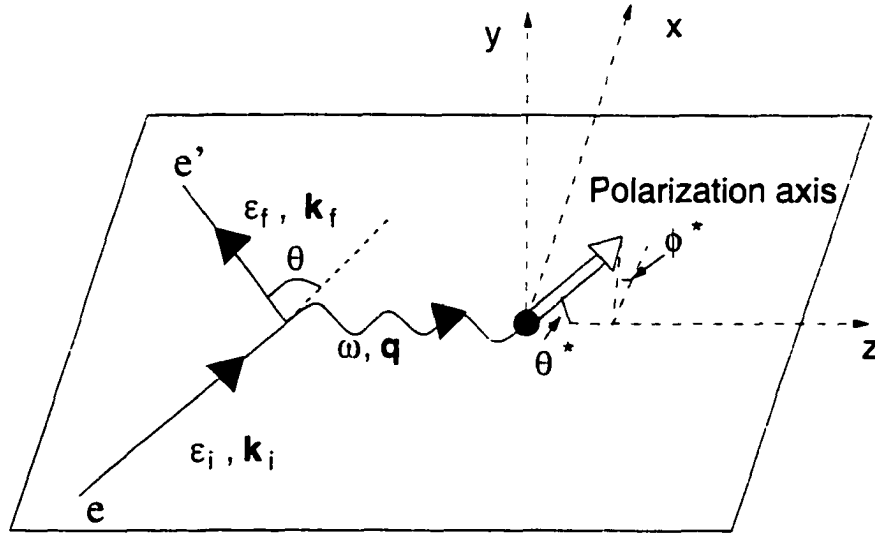


FIG. 21: Kinematic and coordinate system for scattering of polarized electrons from a polarized target.

The kinematic functions v_L and v_T are defined in Eqs. (158) and (159), while $v_{LT'}$ and $v_{T'}$ are given by

$$v_{LT'} = -\frac{1}{\sqrt{2}} \frac{q_\mu^2}{q^2} \tan \frac{\theta}{2} . \quad (207)$$

$$v_{T'} = \sqrt{\frac{q_\mu^2}{q^2} + \tan^2 \frac{\theta}{2} \tan \frac{\theta}{2}}. \quad (208)$$

The response functions R_α contain the nuclear structure information. They are defined in terms of the nuclear charge and current operators $\rho(\mathbf{q})$ and $\mathbf{j}(\mathbf{q})$ as:

$$R_L \equiv \sum_f |\langle f | \rho(\mathbf{q}) | \Psi_{3, \frac{1}{2}\sigma_3} \rangle|^2. \quad (209)$$

$$R_T \equiv \sum_f |\langle f | \mathbf{j}(\mathbf{q}) | \Psi_{3, \frac{1}{2}\sigma_3} \rangle|^2. \quad (210)$$

$$R_{LT'} \equiv -2 \sum_\lambda \Re \left\{ \sum_f \langle f | \rho(\mathbf{q}) | \Psi_{3, \frac{1}{2}\sigma_3} \rangle^* \langle f | j_\lambda(\mathbf{q}) | \Psi_{3, \frac{1}{2}\sigma_3} \rangle \right\}. \quad (211)$$

$$R_{T'} \equiv \sum_\lambda \sum_f [\lambda |\langle f | j_\lambda(\mathbf{q}) | \Psi_{3, \frac{1}{2}\sigma_3} \rangle|^2]. \quad (212)$$

where $\Psi_{3, \frac{1}{2}\sigma_3}$ is the initial ^3He bound state wave function with spin projection σ_3 , and $\lambda = \pm 1$ denote the spherical components of the current operator. We note that the sum over the three-nucleon final states $|f\rangle$ is in fact restricted to include only the pd continuum, since the excitation energies of interest here are below the threshold for the three-body breakup. Finally, note that the unpolarized cross section is obtained from Eq. (204), summing over the electron helicities. The longitudinal-transverse and transverse-transverse asymmetries $A_{LT'}$ and $A_{T'}$ are related to the functions v_α and R_α via the relations:

$$\begin{aligned} A_{LT'}(q, \omega) &= \frac{v_{LT'} R_{LT'}(q, \omega)}{v_L R_L(q, \omega) + v_T R_T(q, \omega)}, \\ A_{T'}(q, \omega) &= \frac{v_{T'} R_{T'}(q, \omega)}{v_L R_L(q, \omega) + v_T R_T(q, \omega)}. \end{aligned} \quad (213)$$

To obtain explicit expressions for the response functions R_α in terms of the reduced matrix elements of Coulomb (C), transverse electric (E) and transverse magnetic (M) multipole operators, already defined in Eqs. (164)–(166), we first introduce the electromagnetic transition amplitudes between the initial ^3He bound state and the final pd continuum state having proton and deuteron with relative momentum \mathbf{p} and spin projections, respectively, σ_2 and σ . These transition amplitudes are given by

$$\rho_{\sigma\sigma_2\sigma_3}(\mathbf{p}, \mathbf{q}) = \langle \Psi_{\mathbf{p}, \sigma\sigma_2}^{(-)} | \rho(\mathbf{q}) | \Psi_{3, \frac{1}{2}\sigma_3} \rangle, \quad (214)$$

$$j_{\sigma\sigma_2\sigma_3}^\lambda(\mathbf{p}, \mathbf{q}) = \langle \Psi_{\mathbf{p}, \sigma\sigma_2}^{(-)} | \hat{\epsilon}_\lambda(\mathbf{q}) \cdot \mathbf{j}(\mathbf{q}) | \Psi_{3, \frac{1}{2}\sigma_3} \rangle . \quad (215)$$

where \mathbf{q} is the momentum transfer and $\hat{\epsilon}_\lambda(\mathbf{q})$, $\lambda = \pm 1$, are the transverse polarizations of the virtual photon. The wave function $\Psi_{\mathbf{p}, \sigma\sigma_2}^{(-)}$ with ingoing-wave boundary condition is expanded as

$$\Psi_{\mathbf{p}, \sigma\sigma_2}^{(-)} = 4\pi \sum_{SS_z} \langle \frac{1}{2}\sigma, 1\sigma_2 | SS_z \rangle \sum_{LL_z JJ_z} i^L \langle SS_z, LL_z | JJ_z \rangle Y_{LL_z}^*(\hat{\mathbf{p}}) \bar{\Psi}_{1+2}^{LSJJ_z(-)} . \quad (216)$$

where the $\bar{\Psi}_{1+2}^{LSJJ_z(-)}$ are related to the $\Psi_{1+2}^{LSJJ_z}$ introduced in Section 3.2 via

$$\bar{\Psi}_{1+2}^{LSJJ_z(-)} = e^{-i\sigma_L} \sum_{L'S'} \left[1 + i R^J \right]_{LS, L'S'}^{-1} \Psi_{1+2}^{L'S'JJ_z} . \quad (217)$$

Here R^J is the R -matrix in channel J and σ_L is the Coulomb phase shift, given by

$$\sigma_L = \arg[\Gamma(L + 1 + i\eta)] , \quad (218)$$

with η defined as

$$\eta = \frac{2\alpha}{v_{\text{rel}}} . \quad (219)$$

α being the fine structure constant and v_{rel} the pd relative velocity. Introducing the expansion of Eqs. (216) and (217) into the matrix elements of Eqs. (214)–(215), one finds:

$$j_{\sigma\sigma_2\sigma_3}^\lambda(\mathbf{p}, \mathbf{q}) = 4\pi \sum_{LL_z SS_z JJ_z} (-i)^L \langle \frac{1}{2}\sigma, 1\sigma_2 | SS_z \rangle \langle SS_z, LL_z | JJ_z \rangle Y_{LL_z}(\hat{\mathbf{p}}) j_{J_z \lambda \sigma_3}^{LSJ}(\mathbf{q}) , \quad (220)$$

$$j_{J_z \lambda \sigma_3}^{LSJ}(\mathbf{q}) = \langle \bar{\Psi}_{1+2}^{LSJJ_z(-)} | \hat{\epsilon}_\lambda(\mathbf{q}) \cdot \mathbf{j}(\mathbf{q}) | \Psi_{3, \frac{1}{2}\sigma_3} \rangle . \quad (221)$$

and similar expressions hold for the $\rho_{\sigma\sigma_2\sigma_3}(\mathbf{p}, \mathbf{q})$ amplitudes. When $\hat{\mathbf{q}}$ is taken along the z -axis, i.e. the spin-quantization axis, standard techniques [93] lead to the following expansions for the amplitudes $\rho_{J_z \sigma_3}^{LSJ}(\mathbf{q})$ and $j_{J_z \lambda \sigma_3}^{LSJ}(\mathbf{q})$ in terms of reduced matrix elements of Coulomb, transverse electric and transverse magnetic multipoles:

$$\rho_{J_z \sigma_3}^{LSJ}(q\hat{\mathbf{z}}) = \sqrt{4\pi} \sum_{\ell=0}^{\infty} i^\ell \sqrt{\frac{2\ell+1}{2J+1}} \langle \frac{1}{2}\sigma_3, \ell 0 | JJ_z \rangle C_\ell^{LSJ}(q) . \quad (222)$$

$$j_{J_z \lambda \sigma_3}^{LSJ}(q\hat{\mathbf{z}}) = -\sqrt{2\pi} \sum_{\ell=1}^{\infty} i^{\ell} \sqrt{\frac{2\ell+1}{2J+1}} \langle \frac{1}{2} \sigma_3, \ell \lambda | J J_z \rangle [\lambda M_{\ell}^{LSJ}(q) + E_{\ell}^{LSJ}(q)] . \quad (223)$$

Here $T_{\ell}^{LSJ}(q)$ is a short notation for $\langle \bar{\Psi}_{1+2}^{LSJ(-)} \| T_{\ell}(q) \| \Psi_{3, \frac{1}{2}} \rangle$, with $T \equiv C, E, M$. The calculation of the matrix elements $\rho_{J_z \sigma_3}^{LSJ}(q\hat{\mathbf{z}})$ and $j_{J_z \lambda \sigma_3}^{LSJ}(q\hat{\mathbf{z}})$ is described in the next Section. Given $\rho_{J_z \sigma_3}^{LSJ}(q\hat{\mathbf{z}})$ and $j_{J_z \lambda \sigma_3}^{LSJ}(q\hat{\mathbf{z}})$, the reduced matrix elements $C_{\ell}^{LSJ}(q)$, $M_{\ell}^{LSJ}(q)$ and $E_{\ell}^{LSJ}(q)$ are obtained inverting Eqs. (222) and (223). For example we have:

$$C_0^{LS\frac{1}{2}}(q) = \frac{1}{\sqrt{2\pi}} \rho_{\frac{1}{2} \frac{1}{2}}^{LS\frac{1}{2}}(q\hat{\mathbf{z}}) . \quad (224)$$

$$M_1^{LS\frac{3}{2}}(q) = \frac{i}{\sqrt{2\pi}} \left[\sqrt{3} j_{\frac{3}{2} 1 \frac{1}{2}}^{LS\frac{3}{2}}(q\hat{\mathbf{z}}) - j_{-\frac{1}{2} -1 \frac{1}{2}}^{LS\frac{3}{2}}(q\hat{\mathbf{z}}) \right] . \quad (225)$$

Using Eqs. (214)-(223), the explicit expressions for the response functions R_{α} in terms of the reduced matrix elements of the multipole operators are given by:

$$R_L = f_{pd} \sum_{LSJ\ell} |C_{\ell}^{LSJ}|^2 . \quad (226)$$

$$R_T = f_{pd} \sum_{LSJ\ell} (|E_{\ell}^{LSJ}|^2 + |M_{\ell}^{LSJ}|^2) . \quad (227)$$

$$R_{LT'} = 2\sqrt{2} f_{pd} \sum_{LSJ} \frac{\sqrt{J+1/2}}{2J+1} \Re \left[\left(C_{-}^{LSJ} + i C_{+}^{LSJ} \right)^* \left[\sqrt{J-1/2} (M_{-}^{LSJ} + E_{-}^{LSJ}) - i \sqrt{J+3/2} (M_{+}^{LSJ} + E_{+}^{LSJ}) \right] \right] . \quad (228)$$

$$R_{T'} = 2 f_{pd} \sum_{LSJ} \frac{1}{2J+1} \left[|M_{-}^{LSJ} + E_{-}^{LSJ}|^2 - |M_{+}^{LSJ} + E_{+}^{LSJ}|^2 - 2 \sqrt{(J+3/2)(J-1/2)} \Im \left[(M_{-}^{LSJ} + E_{-}^{LSJ})^* (M_{+}^{LSJ} + E_{+}^{LSJ}) \right] \right] . \quad (229)$$

where the phase-space factor f_{pd} is given by $f_{pd} = 4\mu p$, and in the interference response functions the notation T_{\pm}^{LSJ} for the reduced matrix elements means $T_{\ell=J\pm 1/2}^{LSJ}$. The magnitude of the relative momentum p is fixed by energy conservation

$$\omega + E_3 = E_2 + \frac{q^2}{2(m_2 + m)} + \frac{p^2}{2\mu} . \quad (230)$$

where E_2 and E_3 are the two- and three-body ground-state energies, m_2 is the deuteron mass and μ is the 1+2 reduced mass. We will refer to the term $p^2/(2\mu)$ as excitation energy and it will be indicated with ω_X below.

6.2 Calculation

The model for the current operator in the matrix element $j_{\sigma\sigma_2\sigma_3}^\lambda(\mathbf{p}, \mathbf{q})$ of Eq. (215) includes, besides the standard one-body term of Eq. (54), also the model-independent (MI) two-body operators PS, V, SO, LL and SO2, obtained from the charge-independent part of the AV18 interaction, the model-dependent (MD) $\rho\pi\gamma$ and $\omega\pi\gamma$ two-body currents, and finally the two-body Δ -contributions arising from the $\mathbf{j}_i(\mathbf{q}; N \rightleftharpoons \Delta)$ and $\mathbf{j}_i(\mathbf{q}; \Delta \rightarrow \Delta)$ operators defined in Eqs. (118) and (119), respectively. The three-body currents associated with the S-wave two-pion exchange three-nucleon interaction (terms labelled $\pi\pi_S$ in the previous Chapters) and with the $NN \rightleftharpoons N\Delta$ transition have not been included. The contributions of these terms were found already small in the trinucleon form factor calculations [13], as discussed in Chapter 5.

The model for the charge operator in the matrix element $\rho_{\sigma\sigma_2\sigma_3}(\mathbf{p}, \mathbf{q})$ of Eq. (214), contains the standard one-body term of Eq. (55), and the two-body contributions PS, V, ω , $\rho\pi\gamma$ and $\omega\pi\gamma$.

The matrix elements of Eqs. (214) and (215) are calculated using the same Monte Carlo techniques based on the Metropolis *et al.* algorithm [95] as the ones discussed in Section 5.2. We have again used the probability density $W(\mathbf{R})$ of Eq. (186), with $\Psi_\pm \equiv \Psi_{3, \frac{1}{2} \pm \frac{1}{2}}$.

Due to the restricted model for the Δ -currents, which includes only $\mathbf{j}_i(\mathbf{q}; N \rightleftharpoons \Delta)$ and $\mathbf{j}_i(\mathbf{q}; \Delta \rightarrow \Delta)$, we do not retain the Δ -contributions associated with the diagrams of Fig. 12. Instead, only the terms shown in Fig. 11 have been considered. These have been calculated with the techniques described in Section 5.2.

6.3 Results

The most recent and systematic experimental study of the unpolarized threshold electrodisintegration of ^3He and ^3H we are aware of was carried out by Retzlaff *et al.* [111] at the MIT/Bates Linear Accelerator Center. The longitudinal and transverse response functions R_L and R_T were obtained using Rosenbluth separations for three-momentum transfers in the range $0.88\text{--}2.87\text{ fm}^{-1}$ and excitation energies from two-body thresholds up to 18 MeV. We are interested here to the inclusive ^3He electron scattering data, which are in agreement with the measurements of earlier experiments [112], after scaling for the slightly different kinematics. No calculations of the ^3H response functions have been carried out in the present study.

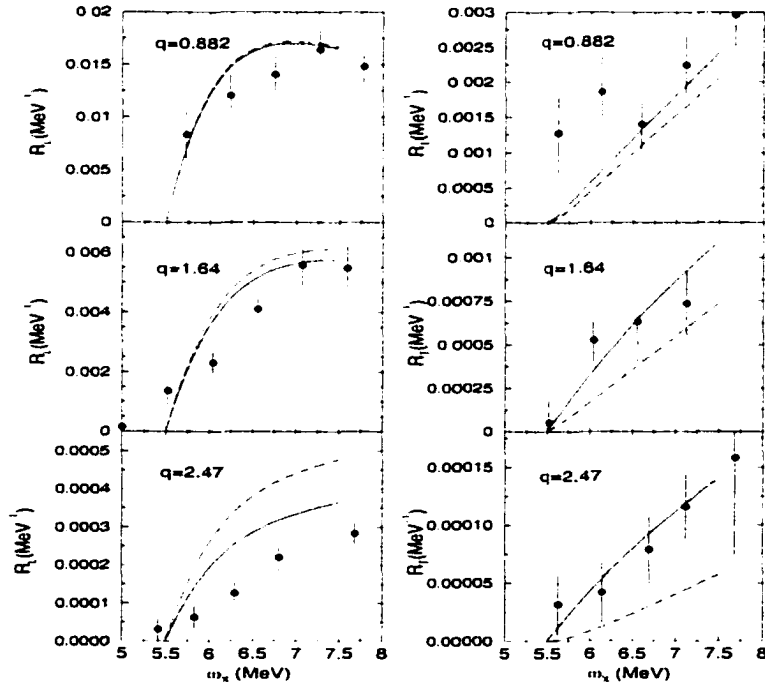


FIG. 22: The longitudinal and transverse response functions of ^3He , obtained with the AV18/UNIX Hamiltonian model and one-body only (dashed lines) or both one- and two-body (solid lines) charge and current operators, are compared with the data of Ref. [111] at excitation energies below the ppn breakup threshold.

The ^3He R_L and R_T results at momentum transfer values $q=0.88, 1.64$ and

2.47 fm^{-1} are shown in Fig. 22, where the data are compared with our calculations performed using one-body only (dashed lines) or both one- and two-body (solid lines) charge and current operators. We have here retained the contributions from $L=0-5$ pd scattering states (see Eqs. (226) and (227)), and we have verified that the expansion is then fully converged. There is satisfactory agreement between theory and experiment for all cases, but for the longitudinal response at $q=2.47 \text{ fm}^{-1}$. The data are affected however by rather large errors. The two-body components of the transition operator play an important role, particularly for the transverse response at the highest q -values. The relative sign between the one- and two-body contributions is consistent with that expected from elastic form factor studies of ^3He [13]. As already seen in Section 5.3, the two-body current (charge) operators increase (decrease) the one-body predictions for the magnetic (charge) form factor at $q \leq 3 \text{ fm}^{-1}$.

In Fig. 23 we show the R_L , $R_{LT'}$, R_T and $R_{T'}$ response functions at a fixed excitation energy $\omega_X = 1 \text{ MeV}$ above the pd threshold, in the three-momentum transfer range $0-5 \text{ fm}^{-1}$. In R_L and $R_{LT'}$ the $L = 0$ pd continuum states give the dominant contribution, while in R_T and $R_{T'}$ both $L = 0$ and $L = 1$ states give equally important contributions over the whole q range. As can be seen comparing the curves where only one-body contributions are retained (labelled “IA”) and those with both one- and two-body contributions (labelled “FULL”), all response functions are substantially affected by two-body currents, especially $R_{LT'}$ and $R_{T'}$.

Finally, in Fig. 24 we show the unpolarized cross section, and the $A_{LT'}$ and $A_{T'}$ asymmetries in the threshold region at an incident electron energy of 4 GeV . The asymmetries are relatively large at high q , and particularly sensitive to two-body currents. The cross section for the chosen kinematics (incident electron energy of 4 GeV , fixed pd excitation energy of 1 MeV , and $0^\circ < \theta < 14^\circ$) is dominated by the longitudinal response function. Note that in Fig. 24 we also show the plane-wave-impulse-approximation (PWIA) results. These have been calculated

by approximating the wave function as

$$\Psi_{1+2}^{LSJJ_z}(\text{PWIA}) = \sum_{\text{cyclic } ijk} \left[[s_i \otimes \phi_d(\mathbf{x}_i)]_S \otimes Y_L(\hat{\mathbf{y}}_i) \right]_{JJ_z} \frac{F_L(pr_{pd})}{pr_{pd}}. \quad (231)$$

See Section 3.2 for notations. The large difference between the PWIA and the IA and FULL results indicates that the final-state interaction between the proton and the deuteron plays an important role.

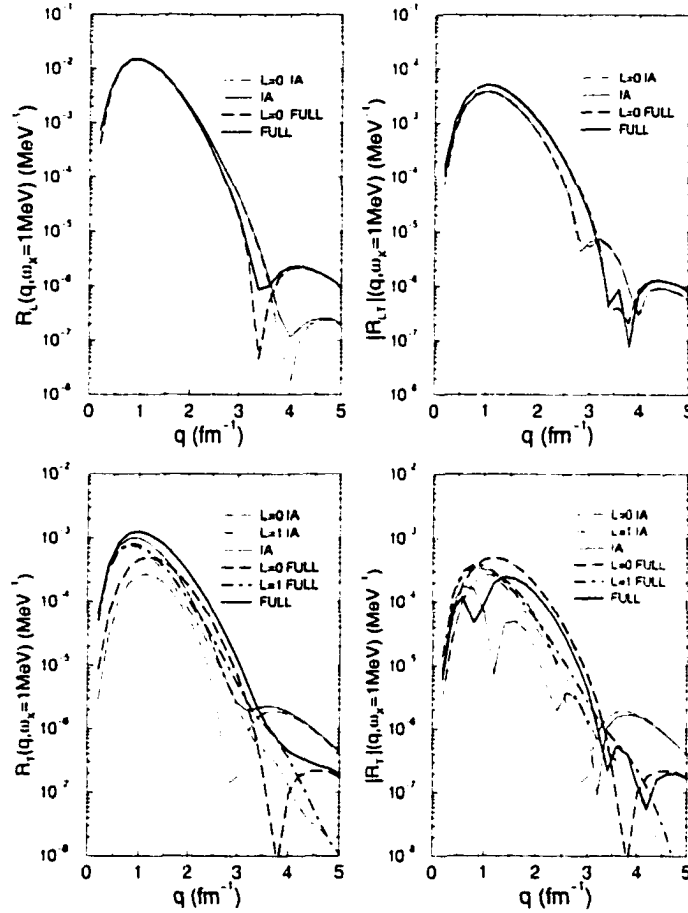


FIG. 23: The longitudinal (R_L), longitudinal-transverse ($R_{LT'}$), transverse (R_T) and transverse-transverse ($R_{T'}$) response functions of ^3He , obtained with the AV18/UIX Hamiltonian model and one-body only (thick dashed lines) or both one- and two-body (thick solid lines) charge and current operators, are displayed at a fixed excitation energy of 1 MeV for three-momentum transfers in the range 0–5 fm^{-1} . In R_L and $R_{LT'}$ we show the contributions associated with the (dominant) S-wave pd scattering states, while in R_T and $R_{T'}$ both S- and P-wave contributions are shown.

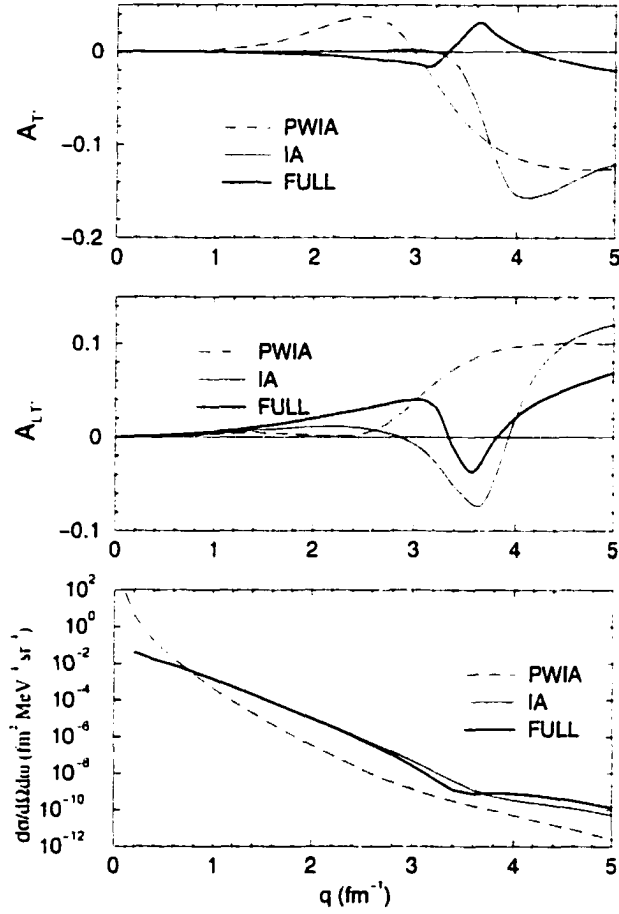


FIG. 24: The inclusive cross section, and the A_{LT} and A_T asymmetries, obtained with the AV18/UIX Hamiltonian model and one-body only (dashed lines) or both one- and two-body (solid lines) charge and current operators, are displayed for ^3He at a fixed excitation energy of 1 MeV for three-momentum transfers in the range $0\text{--}5 \text{ fm}^{-1}$. The results in PWIA (dotted lines) are also shown. The incident electron energy is 4 GeV, and the electron scattering angle is in the range $0\text{--}14^\circ$.

Chapter 7

The *hep* Reaction

There has been recently a revival of interest in the process ${}^3\text{He}(p,e^+\nu_e){}^4\text{He}$ [18, 19, 20, 21, 22], known as the *hep* reaction. This interest has been spurred by the Super-Kamiokande (SK) collaboration measurements of the energy spectrum of electrons recoiling from scattering with solar neutrinos [23, 113, 114]. At energies larger than 14 MeV, more recoil electrons have been observed than expected relative to standard-solar-model (SSM) predictions [24], reduced by a factor of $\simeq 0.5$ to fit the lower-energy bins. The *hep* process is the only source of solar neutrinos with energies larger than 15 MeV—their end-point energy is about 19 MeV. The SSM neutrino flux spectra [24] are shown in Fig. 25. Since the *hep* process has too small a cross section to be studied experimentally, the associated neutrino flux is based only on theoretical calculations [25]. The discrepancy between the observed and SSM energy spectra has therefore led to question the reliability of these *hep* cross section calculations. In particular, the SK collaboration [23] has shown that a large enhancement, by a factor of about 17, of the *hep* contribution would essentially fit the observed excess of recoiling electrons.

The theoretical description of the *hep* process constitutes a challenging problem from the standpoint of nuclear few-body theory, as discussed in Refs. [14, 16]. To explain this aspect, we consider the limit in which the momentum transfer q of the reaction is set to zero. This approximation was taken in all previous calculations, and it can appear to be adequate, since, for the *hep* reaction, $q \leq$

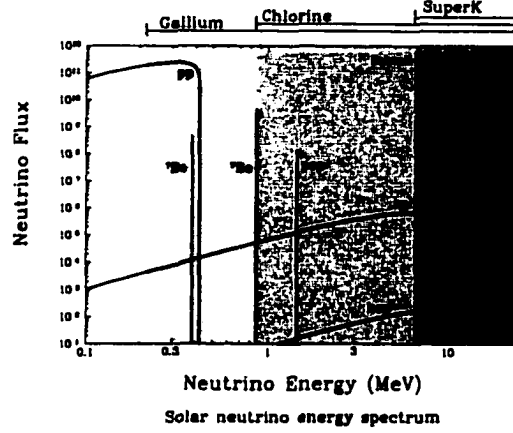


FIG. 25: The SSM solar neutrino energy spectrum. The continuum neutrino fluxes are given in $\text{cm}^{-2} \text{sec}^{-1} \text{MeV}^{-1}$, the lines in $\text{cm}^{-2} \text{sec}^{-1}$.

20 MeV/c. Introducing the $^{2S+1}L_J$ notation for the $p^3\text{He}$ initial state ($S=0.1$ is the channel spin, L the two clusters relative orbital angular momentum and $\mathbf{J} = \mathbf{L} + \mathbf{S}$), in the $q = 0$ limit the hep reaction is induced only by the axial current and axial charge operators, acting, respectively, between the initial 3S_1 and 3P_0 capture channels and the final $J^\pi = 0^+$ ^4He ground state. When P-wave contributions are neglected, therefore, only the axial current operator matrix element between the 3S_1 initial state and the ^4He final state needs to be considered. The non-relativistic one-body axial current operator has been discussed in Chapter 4 (see Eq. (137)), and, in its $q=0$ limit, is known as Gamow-Teller (GT) operator. If the ^4He wave function were to consist of a symmetric S-state term only, namely $\Psi_4 = \phi_4(S) \det[p \uparrow_1, p \downarrow_2, n \uparrow_3, n \downarrow_4]$, then it would be an eigenfunction of the GT operator. Of course, tensor components in the nuclear interactions generate significant D-state admixtures, that partially spoil this eigenstate property. To the extent that this property is approximately satisfied, though, the matrix element of the GT operator between the 3S_1 $p^3\text{He}$ and ^4He states vanishes due

to orthogonality between the initial and final states. Therefore, this transition which is expected to give the leading contribution, is instead suppressed. Thus, to obtain a reliable estimate, one needs: (i) an accurate description of the small components of the ${}^3\text{He}$ and ${}^4\text{He}$ wave functions, in particular the D-state admixtures; (ii) inclusion in the model for the axial current operator of both relativistic corrections and many-body contributions; (iii) inclusion in the $p\,{}^3\text{He}$ initial state of all $L = 0$ and $L = 1$ capture channels. These are in fact the main features of the calculation presented here. In Section 7.1 we define the astrophysical S -factor and the cross section of the hep reaction, while in Section 7.2 we give some details of the calculation. Finally, in Section 7.3 we present and discuss our results.

7.1 The hep Cross Section and Astrophysical S -factor

The astrophysical S -factor at center-of-mass (c.m.) energy E is defined as

$$S(E) = E \sigma(E) e^{2\pi\eta} . \quad (232)$$

where $\sigma(E)$ is the hep cross section and η has been given in Eq. (219). The term $e^{2\pi\eta}$ is the inverse of the so-called Gamow penetration factor, proportional to the probability that the proton and ${}^3\text{He}$ moving with relative velocity v_{rel} , will penetrate their electrostatic repulsion. The definition above factors out the strong energy-dependent terms of $\sigma(E)$, so that $S(E)$ is weakly dependent on E . The c.m. energies of interest involved in the $p\,{}^3\text{He}$ weak capture reaction, are of the order of 10 keV: the energy at which the reaction is most probable to occur, known as the Gamow-peak energy, is in fact 10.7 keV.

In this Section we sketch the derivation of the cross section $\sigma(E)$ for the hep reaction. We proceed in three steps: in Subsection 7.1.1 we define the transition amplitude of the process, performing a partial-wave expansion of the $p\,{}^3\text{He}$ initial scattering state, similar to what was done in Section 6.1; in Subsection 7.1.2 we discuss the multipole decomposition of the nuclear weak charge and current

operators, and in Subsection 7.1.3 we give the final expression for the total cross section $\sigma(E)$.

7.1.1 The Transition Amplitude

The capture process ${}^3\text{He}(p.e^+\nu_e){}^4\text{He}$ is induced by the weak interaction Hamiltonian [14, 93]

$$H_W = \frac{G_V}{\sqrt{2}} \int d\mathbf{x} e^{-i(\mathbf{p}_e + \mathbf{p}_\nu) \cdot \mathbf{x}} l_\sigma j^\sigma(\mathbf{x}) . \quad (233)$$

where G_V is the Fermi coupling constant ($G_V = 1.14939 \cdot 10^{-5} \text{ GeV}^{-2}$ [115]), l_σ is the leptonic weak current

$$l_\sigma = \bar{u}_\nu \gamma_\sigma (1 - \gamma_5) v_e \equiv (\bar{l}_0, -\mathbf{l}) . \quad (234)$$

and $j^\sigma(\mathbf{x})$ is the hadronic weak current density. The positron and (electron) neutrino momenta and spinors are denoted, respectively, by \mathbf{p}_e and \mathbf{p}_ν , and v_e and u_ν . The Bjorken and Drell [66] conventions are used for the metric tensor $g^{\sigma\tau}$ and γ -matrices; however, the spinors are normalized as $v_e^\dagger v_e = u_\nu^\dagger u_\nu = 1$. The reaction and its kinematic are described schematically in Fig. 26.

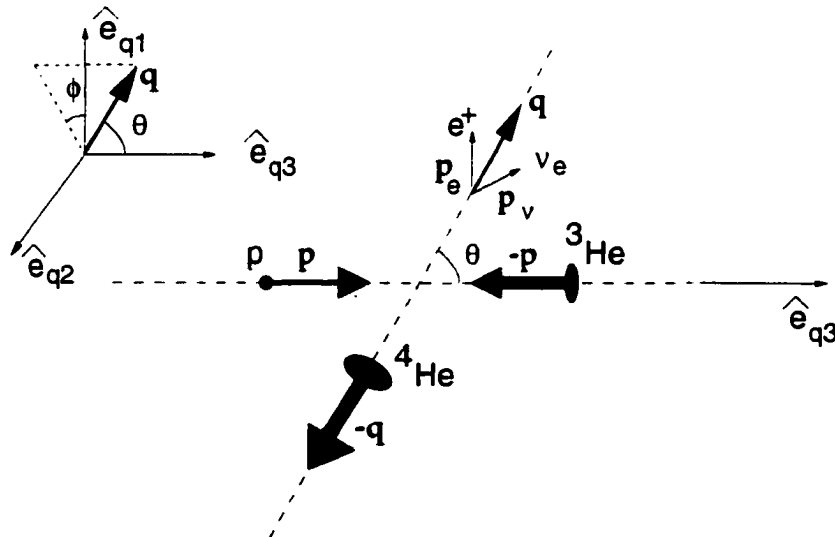


FIG. 26: Schematic representation of the *hep* reaction.

The transition amplitude in the c.m. frame is then given by

$$\langle f|H_W|i\rangle = \frac{G_V}{\sqrt{2}} l^\sigma \langle -\mathbf{q}; {}^4\text{He}|j_\sigma^\dagger(\mathbf{q})|\mathbf{p}; p^3\text{He}\rangle. \quad (235)$$

where $\mathbf{q} = \mathbf{p}_e + \mathbf{p}_\nu$, $|\mathbf{p}; p^3\text{He}\rangle$ and $|\mathbf{q}; {}^4\text{He}\rangle$ represent the $p^3\text{He}$ scattering state with relative momentum \mathbf{p} and ${}^4\text{He}$ bound state recoiling with momentum $-\mathbf{q}$, respectively, and

$$j^\sigma(\mathbf{q}) = \int d\mathbf{x} e^{i\mathbf{q}\cdot\mathbf{x}} j^\sigma(\mathbf{x}) \equiv (\rho(\mathbf{q}) \cdot \mathbf{j}(\mathbf{q})). \quad (236)$$

The dependence of the amplitude upon the spin-projections of the proton and ${}^3\text{He}$ is understood. Since the energies of interest are of the order of 10 keV, it is useful to perform a partial-wave expansion of the $p^3\text{He}$ scattering wave function

$$\Psi_{\mathbf{p}, s_1 s_3}^{(+)} = \sqrt{4\pi} \sum_{LSJJ_z} \sqrt{2L+1} i^L \langle \frac{1}{2}s_1, \frac{1}{2}s_3 | SJ_z \rangle \langle SJ_z, L0 | JJ_z \rangle \bar{\Psi}_{1+3}^{LSJJ_z}, \quad (237)$$

with

$$\bar{\Psi}_{1+3}^{LSJJ_z} = e^{i\sigma_L} \sum_{L'S'} [1 - iR^J]_{LS, L'S'}^{-1} \Psi_{1+3}^{L'S'JJ_z}, \quad (238)$$

where s_1 and s_3 are the proton and ${}^3\text{He}$ spin projections, L , S , and J are the relative orbital angular momentum, channel spin ($S=0,1$), and total angular momentum ($\mathbf{J} = \mathbf{L} + \mathbf{S}$), respectively. R^J is the R -matrix in channel J , and σ_L is the Coulomb phase shift, as defined in Eq. (218). Note that $\Psi^{(+)}$ has been constructed to satisfy outgoing wave boundary conditions, and that the spin quantization axis has been chosen to lie along $\hat{\mathbf{p}}$, which defines the z -axis. The scattering wave function $\Psi_{1+3}^{LSJJ_z}$ as well as the ${}^4\text{He}$ wave function Ψ_4 have been discussed in Chapter 3.

Introducing the expansion of Eqs. (237) and (238) in Eq. (235), we obtain:

$$\begin{aligned} \langle f|H_W|i\rangle &= \frac{G_V}{\sqrt{2}} \sqrt{4\pi} \sum_{LSJJ_z} \sqrt{2L+1} i^L \langle \frac{1}{2}s_1, \frac{1}{2}s_3 | SJ_z \rangle \langle SJ_z, L0 | JJ_z \rangle \\ &\times \left[\bar{l}_0 \langle \Psi_4 | \rho^\dagger(\mathbf{q}) | \bar{\Psi}_{1+3}^{LSJJ_z} \rangle - \sum_{\lambda=0, \pm 1} l_\lambda \langle \Psi_4 | \hat{\mathbf{e}}_{q\lambda}^* \cdot \mathbf{j}^\dagger(\mathbf{q}) | \bar{\Psi}_{1+3}^{LSJJ_z} \rangle \right]. \end{aligned} \quad (239)$$

where, with the future aim of a multipole decomposition of the weak transition operators, the lepton vector \mathbf{l} has been expanded as

$$\mathbf{l} = \sum_{\lambda=0,\pm 1} l_{\lambda} \hat{\mathbf{e}}_{q\lambda}^* . \quad (240)$$

with $l_{\lambda} = \hat{\mathbf{e}}_{q\lambda} \cdot \mathbf{l}$. and

$$\hat{\mathbf{e}}_{q0} \equiv \hat{\mathbf{e}}_{q3} , \quad (241)$$

$$\hat{\mathbf{e}}_{q\pm 1} \equiv \mp \frac{1}{\sqrt{2}} (\hat{\mathbf{e}}_{q1} \pm i \hat{\mathbf{e}}_{q2}) . \quad (242)$$

The orthonormal basis $\hat{\mathbf{e}}_{q1}$, $\hat{\mathbf{e}}_{q2}$, $\hat{\mathbf{e}}_{q3}$ is defined by $\hat{\mathbf{e}}_{q3} = \hat{\mathbf{q}}$, $\hat{\mathbf{e}}_{q2} = \mathbf{p} \times \mathbf{q} / |\mathbf{p} \times \mathbf{q}|$, $\hat{\mathbf{e}}_{q1} = \hat{\mathbf{e}}_{q2} \times \hat{\mathbf{e}}_{q3}$, and is shown in Fig. 26.

7.1.2 The Multipole Expansion

Standard techniques [93] can now be used to perform the multipole expansion of the weak charge and current matrix elements occurring in Eq. (239). In fact, the procedure is quite similar to the one discussed in Section 5.2, for the electromagnetic case. Two main differences need, however, to be taken into account. Firstly, the spin quantization axis is here along $\hat{\mathbf{p}}$ rather than along $\hat{\mathbf{q}}$. Secondly, and most importantly, the longitudinal component of the weak current operator has to be treated explicitly, since its axial-vector part is not conserved. This leads to the introduction of a fourth multipole operator, which we will refer to as the longitudinal (L) multipole (its definition is given below).

To address these complications, we first express the states quantized along $\hat{\mathbf{p}}$ as linear combinations of those quantized along $\hat{\mathbf{q}}$, using Eq. (170). For ease of presentation, we define here θ and ϕ the angles which specify the direction $\hat{\mathbf{q}}$ (see Fig. 26). Then, using the transformation properties under rotations of irreducible tensor operators, we can obtain the following expressions for the matrix elements of charge and current operators:

$$\langle \Psi_4 | \rho^\dagger(\mathbf{q}) | \bar{\Psi}_{1+3}^{LSJJ_z} \rangle = \sqrt{4\pi} (-i)^J (-)^{J-J_z} D_{-J_z,0}^J(-\phi, -\theta, \phi) C_J^{LSJ}(q) , \quad (243)$$

$$\langle \Psi_4 | \hat{\mathbf{e}}_{q0}^* \cdot \mathbf{j}^\dagger(\mathbf{q}) | \bar{\Psi}_{1+3}^{LSJJ_z} \rangle = \sqrt{4\pi} (-i)^J (-)^{J-J_z} D_{-J_z,0}^J(-\phi, -\theta, \phi) L_J^{LSJ}(q) , \quad (244)$$

$$\begin{aligned} \langle \Psi_4 | \hat{\mathbf{e}}_{q\lambda}^* \cdot \mathbf{j}^\dagger(\mathbf{q}) | \bar{\Psi}_{1+3}^{LSJJ_z} \rangle = & - \sqrt{2\pi} (-i)^J (-)^{J-J_z} D_{-J_z, -\lambda}^J(-\phi, -\theta, \phi) \\ & \times \left[\lambda M_f^{LSJ}(q) + E_f^{LSJ}(q) \right]. \end{aligned} \quad (245)$$

Here $\lambda = \pm 1$, and C_f^{LSJ} , L_f^{LSJ} , E_f^{LSJ} and M_f^{LSJ} denote the reduced matrix elements of the Coulomb (C), longitudinal (L), transverse electric (E) and transverse magnetic (M) multipole operators, following the same notation introduced in Section 6.1. The explicit expressions for the C , E and M multipole operators have been given in Eqs. (164)–(166), while the longitudinal multipole is defined as [93]

$$L_{ll_z}(q) = \frac{i}{q} \int d\mathbf{x} \mathbf{j}(\mathbf{x}) \cdot \nabla j_l(qx) Y_{ll_z}(\hat{\mathbf{x}}). \quad (246)$$

where $\mathbf{j}(\mathbf{x})$ is the nuclear current density and $j_l(qx)$ are spherical Bessel functions.

Finally, it is useful to consider the transformation properties under parity of the multipole operators. The weak charge/current operators have components of both scalar/polar-vector (V) and pseudoscalar/axial-vector (A) character, and hence

$$T_{ll_z} = T_{ll_z}(V) + T_{ll_z}(A). \quad (247)$$

where T_{ll_z} is any of the multipole operators above. Obviously, the parity of l th-pole V -operators is opposite of that of l th-pole A -operators. The parity of Coulomb, longitudinal, and electric l th-pole V -operators is $(-)^l$, while that of magnetic l th-pole V -operators is $(-)^{l+1}$, in analogy to the corresponding electromagnetic multipoles (see Section 5.1).

7.1.3 The Cross Section

The cross section for the ${}^3\text{He}(p, e^+ \nu_e){}^4\text{He}$ reaction at a c.m. energy E is given by

$$\begin{aligned} \sigma(E) = & \int 2\pi \delta\left(\Delta m + E - \frac{q^2}{2m_4} - E_e - E_\nu\right) \frac{1}{v_{\text{rel}}} \\ & \times \frac{1}{4} \sum_{s_e s_\nu} \sum_{s_1 s_3} |\langle f | H_W | i \rangle|^2 \frac{d\mathbf{p}_e}{(2\pi)^3} \frac{d\mathbf{p}_\nu}{(2\pi)^3}, \end{aligned} \quad (248)$$

where $\Delta m = m + m_3 - m_4 = 19.287$ MeV (m , m_3 and m_4 are, respectively, the proton, the ${}^3\text{He}$ and the ${}^4\text{He}$ rest masses), and v_{rel} is the p ${}^3\text{He}$ relative velocity,

$v_{\text{rel}} = p/\mu$, μ being the reduced mass. $\mu = mm_3/(m + m_3)$. It is convenient to write:

$$\frac{1}{4} \sum_{s_e s_\nu} \sum_{s_1 s_3} |\langle f | H_W | i \rangle|^2 = (2\pi)^2 G_V^2 L_{\sigma\tau} N^{\sigma\tau}, \quad (249)$$

where the lepton tensor $L^{\sigma\tau}$ is defined as

$$\begin{aligned} L^{\sigma\tau} &\equiv \frac{1}{2} \sum_{s_e s_\nu} l^\sigma l^{\tau*} = \frac{1}{2} \text{tr} \left[\gamma^\sigma (1 - \gamma_5) \frac{\not{p}_e - m_e}{2E_e} \gamma^\tau (1 - \gamma_5) \frac{\not{p}_\nu}{2E_\nu} \right] \\ &= v_e^\sigma v_\nu^\tau + v_\nu^\sigma v_e^\tau - g^{\sigma\tau} v_e \cdot v_\nu + i \epsilon^{\sigma\alpha\tau\beta} v_{e,\alpha} v_{\nu,\beta}. \end{aligned} \quad (250)$$

with $\epsilon^{0123} = -1$, $v_e^\sigma = p_e^\sigma/E_e$ and $v_\nu^\sigma = p_\nu^\sigma/E_\nu$ are the lepton four-velocities. The nuclear tensor $N^{\sigma\tau}$ is defined as

$$N^{\sigma\tau} \equiv \sum_{s_1 s_3} W^\sigma(\mathbf{q}; s_1 s_3) W^{\tau*}(\mathbf{q}; s_1 s_3), \quad (251)$$

where

$$W^{\sigma=0}(\mathbf{q}; s_1 s_3) = \sum_{LSJ} X_0^{LSJ}(\hat{\mathbf{q}}; s_1 s_3) C_J^{LSJ}(q), \quad (252)$$

$$W^{\sigma=3}(\mathbf{q}; s_1 s_3) = \sum_{LSJ} X_0^{LSJ}(\hat{\mathbf{q}}; s_1 s_3) L_J^{LSJ}(q), \quad (253)$$

$$W^{\sigma=\pm 1}(\mathbf{q}; s_1 s_3) = -\frac{1}{\sqrt{2}} \sum_{LSJ} X_{\pm 1}^{LSJ}(\hat{\mathbf{q}}; s_1 s_3) \left[\pm M_J^{LSJ}(q) + E_J^{LSJ}(q) \right]. \quad (254)$$

The dependence upon the direction $\hat{\mathbf{q}}$ and proton and ^3He spin projections s_1 and s_3 is contained in the functions X_λ^{LSJ} given by

$$\begin{aligned} X_\lambda^{LSJ}(\hat{\mathbf{q}}; s_1 s_3) &= \sum_{J_z} \sqrt{2L+1} i^L (-i)^J (-)^{J-J_z} \langle \frac{1}{2} s_1, \frac{1}{2} s_3 | S J_z \rangle \langle S J_z, L 0 | J J_z \rangle \\ &\times D_{-J_z, \lambda}^J(-\phi, -\theta, \phi), \end{aligned} \quad (255)$$

with $\lambda = 0, \pm 1$. Note that the Cartesian components of the lepton and nuclear tensors ($\sigma, \tau = 1, 2, 3$) are relative to the orthonormal basis $\hat{\mathbf{e}}_{q1}$, $\hat{\mathbf{e}}_{q2}$, $\hat{\mathbf{e}}_{q3}$, defined at the end of Section 7.1.1.

The expression for the nuclear tensor can be further simplified by making use of the reduction formulas for the product of rotation matrices [94]. In fact, it can easily be shown that the dependence of $N^{\sigma\tau}$ upon the angle $\cos\theta = \hat{\mathbf{p}} \cdot \hat{\mathbf{q}}$ can be expressed in terms of Legendre polynomials $P_n(\cos\theta)$ and associated Legendre

functions $P_n^m(\cos\theta)$ with $m = 1, 2$. However, given the large number of channels included in the present study (all $L=0$ and $L=1$ capture states), the resulting equations for $N^{\sigma\tau}$ are not particularly illuminating. Indeed, the calculation of the cross section, Eq. (248), is carried out numerically with the techniques discussed in Subsection 7.2.2.

A thorough discussion of the cross section expression of Eq. (248) and its long-wavelength-approximation has been given in Ref. [14]. Here, we only remark that the long-wavelength-approximation for the cross section, commonly used in all previous studies, leads to inaccurate results.

7.2 Calculation

The calculation of the $p^3\text{He}$ weak capture cross section proceeds in two steps: first, we evaluate, via Monte Carlo techniques, the weak charge and current operator matrix elements, and by inverting Eqs. (243)-(245), we decompose these in terms of the reduced matrix elements of the multipole operators. Second, we evaluate the cross section by carrying out numerically the integrations of Eq. (248). These two steps are discussed in Subsections 7.2.1 and 7.2.2, respectively. The model for the weak charge and current operators has been described in Chapter 4.

7.2.1 Monte Carlo Calculation of Matrix Elements

In a frame where the direction of the momentum transfer $\hat{\mathbf{q}}$ also defines the quantization axis of the nuclear spins, the matrix elements of the weak charge and current operators have the multipole expansion

$$\langle \Psi_4 | \rho^\dagger(\mathbf{q}) | \bar{\Psi}_{1+3}^{LSJ, J_z=0} \rangle = \sqrt{4\pi} i^J C_J^{LSJ}(q) . \quad (256)$$

$$\langle \Psi_4 | \hat{\mathbf{e}}_{q0}^* \cdot \mathbf{j}^\dagger(\mathbf{q}) | \bar{\Psi}_{1+3}^{LSJ, J_z=0} \rangle = \sqrt{4\pi} i^J L_J^{LSJ}(q) , \quad (257)$$

$$\langle \Psi_4 | \hat{\mathbf{e}}_{q\lambda}^* \cdot \mathbf{j}^\dagger(\mathbf{q}) | \bar{\Psi}_{1+3}^{LSJ, J_z=\lambda} \rangle = \sqrt{2\pi} i^J \left[\lambda M_J^{LSJ}(q) + E_J^{LSJ}(q) \right] . \quad (258)$$

with $\lambda = \pm 1$. The expressions above can easily be obtained from those in Eqs. (243)-(245), by setting $\theta=\phi=0$ and using $D_{J_z, J_z}^J(0, 0, 0) = \delta_{J_z, J_z}$. The reduced matrix elements of the multipole operators are then obtained inverting

Eqs. (256)–(258). As an example, the reduced matrix element of the axial electric multipole involving a transition from the $p^3\text{He } ^3\text{S}_1$ state is simply given by

$$E_1^{011}(q; A) = -\frac{i}{\sqrt{2\pi}} \langle \Psi_4 | \hat{\mathbf{e}}_{q\lambda}^* \cdot \mathbf{j}^\dagger(\mathbf{q}; A) | \bar{\Psi}_{1+3}^{011, J_z=\lambda} \rangle . \quad (259)$$

The problem is now reduced to evaluate matrix elements of the same type as on the right-hand-side of Eq. (259). Similarly to the procedure described in Section 5.2, we schematically write these matrix elements as

$$\frac{\langle \Psi_{4, N+\Delta} | O | \Psi_{1+3, N+\Delta} \rangle}{[\langle \Psi_{4, N+\Delta} | \Psi_{4, N+\Delta} \rangle \langle \Psi_{1+3, N+\Delta} | \Psi_{1+3, N+\Delta} \rangle]^{1/2}} . \quad (260)$$

where the initial and final states wave functions contain both nucleon and Δ -isobar degrees of freedom and are obtained using the transition correlation operator method (TCO) described in Subsection 4.1.5. When the full wave functions are expanded as in Eq. (190), the numerator of Eq. (260) can be expressed as

$$\langle \Psi_{4, N+\Delta} | O | \Psi_{1+3, N+\Delta} \rangle = \langle \Psi_4 | O(N \text{ only}) | \Psi_{1+3} \rangle + \langle \Psi_4 | O(\Delta) | \Psi_{1+3} \rangle , \quad (261)$$

where the operator $O(N \text{ only})$ denotes all one- and two-body contributions to the weak charge or current operator O , involving only nucleon degrees of freedom, while $O(\Delta)$ includes terms that involve the Δ -isobar degrees of freedom. A diagrammatical illustration of the terms contributing to $O(\Delta)$ is given in Fig. 27. Connected three-body terms containing more than a single Δ isobar have been ignored, since their contributions are expected to be negligible. Indeed, the contribution from diagram (d) of Fig. 27 has already been found numerically very small.

The two-body terms of Fig. 27 are expanded as operators acting on the nucleons' coordinates with the same procedure described in Section 5.2 for the terms of Fig. 11. The three- and four-body terms instead have been calculated retaining the explicit representation of \mathbf{S} (\mathbf{S}^\dagger) as a 4×2 (2×4) matrix (see Section 5.2),

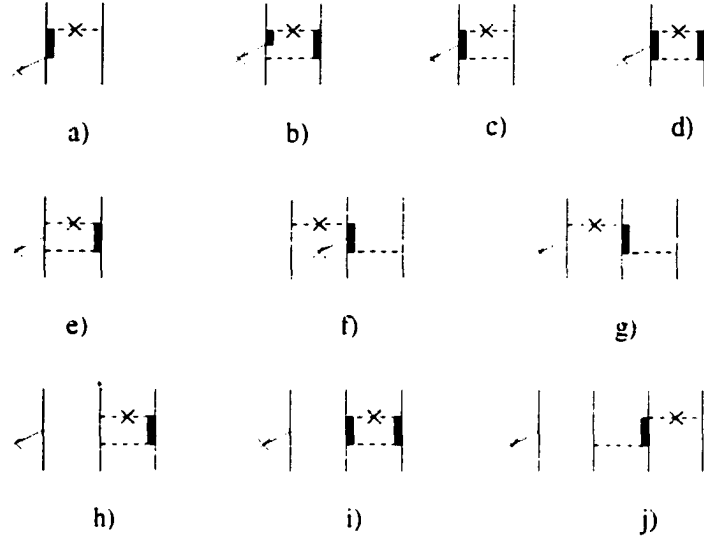


FIG. 27: Diagrammatic representation of the operators included in $O(\Delta)$, due to the one-body current and charge operators, to the transition correlations $U^{N\Delta}$ and $U^{\Delta\Delta}$ and the corresponding Hermitian conjugates. Thin, thick, dashed and cross-dashed lines denote, respectively, nucleons, Δ -isobars, and transition correlations $U^{BB'}$ and $U^{BB'\dagger}$.

and of Σ as a 4×4 matrix

$$\Sigma = \begin{pmatrix} 3\hat{e}_0 & \sqrt{6}\hat{e}_- & 0 & 0 \\ -\sqrt{6}\hat{e}_+ & \hat{e}_0 & \sqrt{8}\hat{e}_- & 0 \\ 0 & -\sqrt{8}\hat{e}_+ & -\hat{e}_0 & \sqrt{6}\hat{e}_- \\ 0 & 0 & -\sqrt{6}\hat{e}_+ & -3\hat{e}_0 \end{pmatrix}.$$

where $\hat{e}_\pm = \mp(\hat{x} \pm i\hat{y})/\sqrt{2}$, $\hat{e}_0 = \hat{z}$, and $\hat{e}_\mu^* = (-)^\mu \hat{e}_{-\mu}$. The result of terms such as (f) $= U_{ij}^{N\Delta\dagger} O_j^{(1)}(\Delta \rightarrow \Delta) U_{jk}^{\Delta N}$ on the nucleon-only state $|\Psi\rangle$ has been derived by first operating with $U_{jk}^{\Delta N}$, then with $O_j^{(1)}(\Delta \rightarrow \Delta)$, and finally with $U_{ij}^{N\Delta\dagger}$. The terms associated with diagrams (f), (g) and (j) were neglected in previous calculations [25].

The matrix elements in Eq. (261) are computed, without any approximation, by Monte Carlo integrations, according to the Metropolis *et al.* algorithm [95]

as described in Section 5.2. It has been found however more convenient to use a probability density $W(\mathbf{R})$ proportional to

$$W(\mathbf{R}) \propto \sqrt{\langle \Psi_4^\dagger(\mathbf{R}) \Psi_4(\mathbf{R}) \rangle} . \quad (262)$$

where the notation $\langle \dots \rangle$ implies sums over the spin-isospin states of the ${}^4\text{He}$ wave function. Typically, 200,000 configurations are enough to achieve a relative error $\leq 5\%$ on the total S -factor.

We finally discuss here an important aspect of the model for the axial transition operators. As already pointed out in Subsection 4.2.5, in the model for the $N\Delta$ and $\Delta\Delta$ weak axial charge and current operators, the axial coupling constants g_A^* and \bar{g}_A , see Eqs. (150)–(153), are not well known. In the quark-model, they are related to the axial coupling constant of the nucleon by the relations $g_A^* = (6\sqrt{2}/5)g_A$ and $\bar{g}_A = (1/5)g_A$. However, given the uncertainties inherent to quark-model predictions, a more reliable estimate for g_A^* is obtained by determining its value phenomenologically in the following way. It is well established by now [12] that the one-body axial current of Eq. (137) leads to a $\simeq 4\%$ underprediction of the measured Gamow-Teller matrix element in tritium β -decay, see Table X. Since the contributions of $\Delta \rightarrow \Delta$ axial currents (as well as those due to the two-body operators of Subsection 4.2.3) are found to be numerically very small, as can be seen again from Table X, this 4 % discrepancy can then be used to determine g_A^* . Obviously, this procedure produces different values for g_A^* depending on how the Δ -isobar degrees of freedom are treated. These values are listed in Table XI for comparison. The g_A^* value that is determined in the context of a TCO calculation based on the AV28Q interaction, is about 40 % larger than the naive quark-model estimate. However, when perturbation theory is used for the treatment of the Δ isobars, the g_A^* value required to reproduce the Gamow-Teller matrix element of tritium β -decay is much smaller than the TCO estimate.

7.2.2 Calculation of the Cross Section

Once the reduced matrix elements (RMEs) in Eqs. (256)–(258) have been obtained, the calculation of the cross section $\sigma(E)$ is reduced to performing the

TABLE X: Contributions to the Gamow-Teller (GT) matrix element of tritium β -decay, obtained with the PHH trinucleon wave functions corresponding to the AV18/UIX Hamiltonian model. The rows labelled “one-body NR” and “one-body RC” list the contributions associated with the single-nucleon axial current operators of Eq. (137) and Eq. (138), respectively, while the row labelled “mesonic” lists the sum of the contributions due to the π -, ρ -, and $\rho\pi$ -exchange axial current operators of Eqs. (142)–(144). The rows labelled “ Δ - g_A^* ” and “ Δ - \bar{g}_A ” list the contributions arising from the one-body Δ -currents of Eqs. (150) and (151), respectively. The row labelled “ Δ -renormalization” lists the contributions associated with renormalization corrections to the “nucleonic” matrix element of $j_i^{(1)}(\mathbf{q}; A)$, due to the presence of Δ -admixture in the wave functions. The cumulative result reproduces the “experimental value” 0.957 for the GT matrix element [12], once the change in the wave functions normalization due to the presence of Δ -components is taken into account.

GT matrix element	
one-body NR	0.9218
one-body RC	-0.0084
mesonic	0.0050
Δ - g_A^*	0.0509
Δ - \bar{g}_A	0.0028
Δ -renormalization	0.0074

TABLE XI: The values of the $N \rightarrow \Delta$ axial coupling constant g_A^* in units of g_A , when the Δ -isobar degrees of freedom are treated in perturbation theory (PT), or in the context of a TCO calculation based on the AV28Q interaction. The purely nucleonic CHH wave functions correspond to the AV18/UIX Hamiltonian model.

Δ -isobar treatment	g_A^*/g_A
PT	1.224
TCO	2.868

integrations over the electron and neutrino momenta in Eq. (248) numerically. We write

$$\sigma(E) = \frac{1}{(2\pi)^2} \frac{G_V^2}{v_{\text{rel}}} \int_0^{p_e^*} dp_e p_e^2 \int_{-1}^1 dx_e \int_{-1}^1 dx_\nu \int_0^{2\pi} d\phi p_\nu^2 f^{-1} L_{\sigma\tau} N^{\sigma\tau} . \quad (263)$$

where one of the azimuthal integrations has been carried out, since the integrand only depends on the difference $\phi = \phi_e - \phi_\nu$. The δ -function occurring in Eq. (248) has also been integrated out resulting in the factor f^{-1} , with

$$f = \left| 1 + \frac{p_e x_{e\nu}}{m_4} + \frac{p_\nu}{m_4} \right| . \quad (264)$$

The magnitude of the neutrino momentum is fixed by energy conservation to be

$$p_\nu = \frac{2\bar{\Delta}}{1 + p_e x_{e\nu}/m_4 + \sqrt{(1 + p_e x_{e\nu}/m_4)^2 + 2\bar{\Delta}/m_4}} . \quad (265)$$

where $\bar{\Delta} = \Delta m + E - E_e - p_e^2/2m_4$. The variable $x_{e\nu}$ is defined as

$$x_{e\nu} = \hat{\mathbf{p}}_e \cdot \hat{\mathbf{p}}_\nu = x_e x_\nu + \sqrt{1 - x_e^2} \sqrt{1 - x_\nu^2} \cos \phi , \quad (266)$$

where $x_e = \cos \theta_e$ and $x_\nu = \cos \theta_\nu$. Finally, the integration over the magnitude of the electron momentum extends from zero up to

$$p_e^* = \sqrt{\left[\sqrt{m_4^2 + m_e^2 + 2m_4(\Delta m + E)} - m_4^2 \right]^2 - m_e^2} . \quad (267)$$

The lepton tensor is explicitly given by Eq. (250), while the nuclear tensor is constructed using Eqs. (251)–(255). Computer codes have been developed to calculate the required rotation matrices corresponding to the $\hat{\mathbf{q}}$ -direction (θ, ϕ) with

$$\begin{aligned} \cos \theta = \hat{\mathbf{z}} \cdot \hat{\mathbf{q}} &= \frac{\hat{\mathbf{z}} \cdot (\mathbf{p}_e + \mathbf{p}_\nu)}{|\mathbf{p}_e + \mathbf{p}_\nu|} \\ &= \frac{p_e x_e + p_\nu x_\nu}{\sqrt{p_e^2 + p_\nu^2 + 2p_e p_\nu x_{e\nu}}} . \end{aligned} \quad (268)$$

Finally, note that the nuclear tensor requires the values of the RMEs at the momentum transfer q , with $q = \sqrt{p_e^2 + p_\nu^2 + 2p_e p_\nu x_{e\nu}}$. To make the dependence

upon q of the RMEs explicit. we have performed an expansion for $q \rightarrow 0$ of the multipole operators given in Eqs. (164)-(166) and (246). Given the low momentum transfers involved, $q \leq 20$ MeV/c, the leading and next-to-leading order terms are sufficient in the expansion. The multipoles are therefore explicitly written as

$$T_J^{LSJ}(q) = q^m (t_0^{LSJ} + t_2^{LSJ} q^2) . \quad (269)$$

where $m = J$ for the Coulomb C_J and magnetic M_J multipole operators, and $m = J - 1$ for the electric E_J and longitudinal L_J ones. However, when $J = 0$, the leading-order term of the expansion of the longitudinal operator L_0 is of order of q [93]. Note that the long-wavelength-approximation corresponds, typically, to retaining only the t_0 term.

A moderate number of Gauss points (of the order of 10) for each of the integrations in Eq. (263) is sufficient to achieve convergence within better than one part in 10^3 . The computer program has been successfully tested by reproducing the result obtained analytically, when only the 3S_1 $E_1(A)$ and $L_1(A)$ and 3P_0 $C_0(A)$ RMEs are retained.

7.3 Results

In this Section we present our main results, for a more detailed discussion, see Ref. [14]. In Subsection 7.3.1 we give the results of the astrophysical S -factor, at three different energies. In Subsection 7.3.2 we discuss the RME values for two of the initial capture channels, the 3S_1 and 3P_0 . The former case is considered to compare with previous calculations [25, 51], while the latter is discussed as an example of one of the P-wave contributions. Finally, in Subsection 7.3.3, we consider the implications to the SK neutrino spectrum.

7.3.1 Results for the S -factor

Our results for the astrophysical S -factor, calculated using CHH wave functions with the AV18/UIX Hamiltonian model, at three different c.m. energies, are given

in Table XII. By inspection of the table, we note that: (i) the energy dependence is rather weak: the value at 10 keV is only about 4 % larger than that at 0 keV; (ii) the P-wave capture states are found to be important, contributing about 40 % of the calculated S -factor. However, the contributions from D-wave channels are expected to be very small. It has been explicitly verified that they are indeed small in 3D_1 capture. (iii) The many-body axial currents play a crucial role in the (dominant) 3S_1 capture, where they reduce the S -factor by more than a factor of four.

TABLE XII: The *hep* S -factor, in units of 10^{-20} keV b, calculated with CHH wave functions corresponding to the AV18/UIX Hamiltonian model, at $p^3\text{He}$ c.m. energies $E=0, 5$, and 10 keV. The rows labelled “one-body” and “full” list the contributions obtained by retaining the one-body only and both one- and many-body terms in the nuclear weak current. The contributions due the 3S_1 channel only and all S- and P-wave channels are listed separately.

	$E=0$ keV		$E=5$ keV		$E=10$ keV	
	3S_1	S+P	3S_1	S+P	3S_1	S+P
one-body	26.4	29.0	25.9	28.7	26.2	29.3
full	6.38	9.64	6.20	9.70	6.36	10.1

The different contributions from the S- and P-wave capture channels to the zero energy S -factor are listed in Table XIII. Note that the sum of the channel contributions is a few % smaller than the total result reported at the bottom of the table, due to the presence of interference terms among multipole operators connecting different capture channels [14]. The results obtained using the two-nucleon AV18 and the older two- and three-nucleon AV14/UVIII interaction models are also listed. The dominant contribution to the S -factor is obtained from the 3S_1 capture channel. The 3P_0 capture channel contribution is not the largest P-wave contribution, as instead expected in previous studies [21], although it is the only one surviving at $q=0$. A detailed analysis of the 3S_1 and 3P_0 RMEs is given in the next Subsection.

By comparing the AV18 and AV18/UIX results, we note that inclusion of the

TABLE XIII: Contributions of the S- and P-wave capture channels to the *hep* *S*-factor at zero $p^3\text{He}$ c.m. energy in 10^{-20} keV b. The results correspond to the AV18/UIX, AV18 and AV14/UVIII Hamiltonian models.

	AV18/UIX	AV18	AV14/UVIII
1S_0	0.02	0.01	0.01
3S_1	6.38	7.69	6.60
3P_0	0.82	0.89	0.79
1P_1	1.00	1.14	1.05
3P_1	0.30	0.52	0.38
3P_2	0.97	1.78	1.24
TOTAL	9.64	12.1	10.1

three-nucleon interaction reduces the total *S*-factor by about 20 %. This decrease is mostly in the 3S_1 contribution, and can be traced back to a corresponding reduction in the magnitude of the one-body axial current matrix elements. The latter are sensitive to the triplet scattering length, for which the AV18 and AV18/UIX models predict, respectively, 10.0 fm and 9.13 fm (see Table IV). This 20 % difference in the total *S*-factor values for AV18 and AV18/UIX emphasizes the need for performing the calculation using a Hamiltonian model that reproduces the binding energies and low-energy scattering parameters for the three- and four-nucleon systems. This is true for the AV18/UIX model, but not for the AV18 model.

The different contributions to the astrophysical *S*-factor when the older AV14/UVIII potential model is used are given in the last column of Table XIII. By comparing these results with the ones obtained with the AV18/UIX, we observe that both the S- and P-wave contributions are not significantly changed; in particular, the 3S_1 capture *S*-factor values differ for only about 3 %. This is due to our procedure of constraining the model dependent two-body axial currents by fitting the Gamow-Teller matrix element of tritium β -decay, as discussed at the end of Subsection 7.2.1. Note that the AV14/UVIII Hamiltonian also reproduces the low-energy properties for the three- and four-nucleon systems.

The chief conclusion of this Subsection is that our best estimate for the S -factor at 10 keV, close to the Gamow-peak energy, is 10.1×10^{-20} keV b. This value is $\simeq 4.5$ times larger than the value adopted in SSM, based on Ref. [25], of 2.3×10^{-20} keV b. It is therefore important to point out the differences between the present and the previous study of Ref. [25]: (i) we have included all P-wave contributions; (ii) we have retained the full dependence on the momentum transfer q ; (iii) we have used the CHH method to describe the initial and final state wave functions, corresponding to the latest generation of realistic interactions. The CHH method is known to be more accurate than the variational Monte Carlo (VMC) technique used in Ref. [25], and it better describes the small components of the wave function to which the GT operator is most sensitive. (iv) We have included the $1/m^2$ relativistic corrections in the one-body axial current operator. In 3S_1 capture, for example, these terms increase by 25 % the L_1 and E_1 matrix elements calculated with the GT operator (see below).

7.3.2 The 3S_1 and 3P_0 Captures

The 3S_1 capture is induced by the weak axial charge and current, and weak vector current operators via the multipoles $C_1(A)$, $L_1(A)$, $E_1(A)$, and $M_1(V)$, while the 3P_0 capture is induced by the weak axial charge and the longitudinal component of the weak axial current operators via the multipoles $C_0(A)$ and $L_0(A)$, respectively. The cumulative contributions to the RMEs of these multipoles obtained with AV18/UIX CHH wave functions, at zero c.m. energy and at a lepton momentum transfer $q=19.2$ MeV/c are listed in Tables XIV and XVI. Note that the RMEs listed in all tables are related to those defined in Eqs. (243)–(245) via

$$\overline{T}_J^{LSJ} = \sqrt{\frac{v_{\text{rel}}}{4\pi\alpha} [e^{2\pi\eta} - 1]} T_J^{LSJ}, \quad (270)$$

which can be shown to remain finite in the limit $v_{\text{rel}} \rightarrow 0$, corresponding to zero energy. The cumulative nucleonic contributions are normalized as

$$[\text{one-body + mesonic}] = \frac{\langle \Psi_4 | O(N \text{ only}) | \Psi_{1+3} \rangle}{[\langle \Psi_4 | \Psi_4 \rangle \langle \Psi_{1+3} | \Psi_{1+3} \rangle]^{1/2}}. \quad (271)$$

However, when the Δ -isobar contributions are added to the cumulative sum, the normalization changes to

$$[\text{one-body} + \text{mesonic} + \Delta] = \frac{\langle \Psi_{4.N+\Delta} | O(N \text{ only}) + O(\Delta) | \Psi_{1+3.N+\Delta} \rangle}{[\langle \Psi_{4.N+\Delta} | \Psi_{4.N+\Delta} \rangle \langle \Psi_{1+3.N+\Delta} | \Psi_{1+3.N+\Delta} \rangle]^{1/2}}. \quad (272)$$

The normalization of the initial scattering state Ψ_{1+3} is the same as that of ${}^3\text{He}$, up to corrections of order (volume) $^{-1}$. The three- and four-body normalization ratios $\langle \Psi_{N+\Delta} | \Psi_{N+\Delta} \rangle / \langle \Psi | \Psi \rangle$ have been given in Chapter 4, Table V.

TABLE XIV: Cumulative contributions to the reduced matrix elements (RMEs) $\overline{C}_1(q; A)$, $\overline{L}_1(q; A)$, $\overline{E}_1(q; A)$ and $\overline{M}_1(q; V)$ in ${}^3\text{S}_1$ capture at zero p ${}^3\text{He}$ c.m. energy. The momentum transfer q is 19.2 MeV/c, and the results correspond to the AV18/UIX Hamiltonian model. The row labelled “one-body” lists the contributions associated with the operators in Eq. (135) for the weak axial charge $\rho(A)$, Eq. (136) for the weak axial current $\mathbf{j}(A)$, and Eq. (133) for the weak vector current $\mathbf{j}(V)$; the row labelled “mesonic” lists the results obtained by including, in addition, the contributions associated with the operators in Eqs. (145)–(147) for $\rho(A)$, Eqs. (142)–(144) for $\mathbf{j}(A)$, and Eqs. (88)–(89) for $\mathbf{j}(V)$, with the substitutions $\tau_{i,z} \rightarrow \tau_{i,\pm}$ and $(\boldsymbol{\tau}_i \times \boldsymbol{\tau}_j)_z \rightarrow (\boldsymbol{\tau}_i \times \boldsymbol{\tau}_j)_\pm$ (see Subsection 4.2.2); finally, the row labelled “ Δ ” lists the results obtained by also including the contributions of the operators in Eqs. (152)–(153) for $\rho(A)$, Eqs. (150)–(151) for $\mathbf{j}(A)$, and Eqs. (154)–(155) for $\mathbf{j}(V)$. The Δ contributions in both $\rho(A)$ and $\mathbf{j}(A)$ are calculated with the TCO method, and take into account the change in normalization of the wave functions due to the presence of Δ -components. Those in $\mathbf{j}(V)$ are calculated in perturbation theory. Note that the RMEs are purely imaginary and in fm $^{3/2}$ units.

	$\overline{C}_1(q; A)$	$\overline{L}_1(q; A)$	$\overline{E}_1(q; A)$	$\overline{M}_1(q; V)$
one-body	0.147×10^{-1}	-0.730×10^{-1}	-0.106	0.333×10^{-2}
mesonic	0.156×10^{-1}	-0.679×10^{-1}	-0.984×10^{-1}	-0.263×10^{-2}
Δ	0.155×10^{-1}	-0.293×10^{-1}	-0.440×10^{-1}	-0.484×10^{-2}

Inspection of the ${}^3\text{S}_1$ capture RMEs of Table XIV, shows that: (i) the $C_1(A)$ RMEs are not small, compared to the dominant $L_1(A)$ and $E_1(A)$ terms. (ii) There is destructive interference between the one- and many-body axial current contributions to the $L_1(A)$ and $E_1(A)$ RMEs, as it was first obtained in Ref. [51], using VMC wave functions. (iii) Among the many-body axial current contributions, those associated with Δ -excitation are the largest.

TABLE XV: Cumulative contributions, at momentum transfers $q=0$ and 19.2 MeV/c, to the reduced matrix elements (RMEs) $\overline{L}_1(q; A)$ and $\overline{E}_1(q; A)$ of the weak axial current in ${}^3\text{S}_1$ capture at zero $p^3\text{He}$ c.m. energy. The results correspond to the AV18/UIX Hamiltonian model. Notations as in Table XIV for “one-body”, “mesonic” and “ Δ -TCO”, which there was labelled “ Δ ”. Finally, the row labelled “ Δ -PT” lists the results obtained by including the contributions of the operator in Eq. (150), calculated in perturbation theory (PT). The Δ -TCO results also take into account the change in normalization of the wave functions due to the presence of Δ -components. Note that the RMEs are purely imaginary and in $\text{fm}^{3/2}$ units.

	$\overline{L}_1(q; A)$		$\overline{E}_1(q; A)$	
	$q=0$ MeV/c	$q=19.2$ MeV/c	$q=0$ MeV/c	$q=19.2$ MeV/c
one-body	-0.880×10^{-1}	-0.730×10^{-1}	-0.125	-0.106
mesonic	-0.829×10^{-1}	-0.679×10^{-1}	-0.117	-0.984×10^{-1}
Δ -TCO	-0.440×10^{-1}	-0.293×10^{-1}	-0.625×10^{-1}	-0.440×10^{-1}
Δ -PT	-0.447×10^{-1}	-0.298×10^{-1}	-0.631×10^{-1}	-0.443×10^{-1}

To study the q -dependence of the dominant $L_1(A)$ and $E_1(A)$ multipoles, we have listed in Table XV the cumulative contributions to the multipoles RMEs at two different momentum transfers $q=0$ and $q=19.2$ MeV/c. The q -dependence is important only for the one-body contribution. In fact, the difference between the $q=0$ and $q=19.2$ MeV/c RMEs is constant for all the cumulative contributions (0.015 and 0.019 for $L_1(A)$ and $E_1(A)$, respectively). The last row of Table XV, labelled “ Δ -PT”, lists the RMEs obtained using perturbation theory in the treatment of the Δ -isobar degrees of freedom (see Subsection 4.1.5). Note that in this case, the results have been normalized according to Eq. (271). Comparing these RMEs with the ones obtained in the TCO context (row labelled “ Δ -TCO”), we see a difference of only 1-2 %. This is due to the fact that in both cases the $N\Delta$ axial coupling constant g_A^* is obtained by fitting the Gamow-Teller matrix element in tritium β -decay, as discussed in Section 7.2. The dependence of our calculation on the Δ -isobar degrees of freedom treatment is therefore strongly reduced.

The ${}^3\text{P}_0$ capture RMEs are presented in Table XVI. We first note that the ${}^3\text{P}_0$

multipoles are in fact not small: both the $C_0(A)$ and $L_0(A)$ RMEs are of the same order of magnitude as the $E_1(A)$ and $L_1(A)$ RMEs in 3S_1 capture. Furthermore, there is constructive interference between the one- and many-body contributions to both the axial charge and current operators. In particular, the two-body axial charge operators of Subsection 4.2.4, among which the pion-exchange term is dominant, give a $\simeq 20\%$ correction to the one-body contribution in the $C_0(A)$ RME. The $L_0(A)$ RME is about 40 % of, and has the same sign as, the $C_0(A)$ RME. This positive relative sign produces a destructive interference between these RMEs in the cross section, substantially reducing the 3P_0 overall contribution to the S -factor [14]. The $C_0(A)$ and $L_0(A)$ RMEs are in fact expected to be of the same sign, as discussed in Ref. [14].

TABLE XVI: Cumulative contributions to the reduced matrix elements (RMEs) $\overline{C}_0(q; A)$ and $\overline{L}_0(q; A)$ in 3P_0 capture at zero p ^3He c.m. energy. The momentum transfer q is 19.2 MeV/c, and the results correspond to the AV18/UIX Hamiltonian model. Notations as in Table XIV. Note that the RMEs are purely imaginary and in $\text{fm}^{3/2}$ units.

	$\overline{C}_0(q; A)$	$\overline{L}_0(q; A)$
one-body	0.371×10^{-1}	0.182×10^{-1}
mesonic	0.444×10^{-1}	0.183×10^{-1}
Δ	0.459×10^{-1}	0.188×10^{-1}

7.3.3 Implications for the Super-Kamiokande Solar Neutrino Spectrum

The Super-Kamiokande (SK) experiment detects solar neutrinos by neutrino-electron scattering. It is sensitive, according to the SSM (see Fig. 25), to the very energetic neutrinos from the ^8B weak decay ($^8\text{B} \rightarrow ^4\text{He} + ^4\text{He} + e^+ + \nu_e$) and from the *hep* reaction. In the SSM the *hep* neutrinos contribution is expected to be very small. However, due to a larger end-point energy respect to the ^8B weak decay, the *hep* reaction is the only source of solar neutrinos at energies larger than

$\simeq 15$ MeV.

The SK results are presented as ratio of the measured to the SSM predicted events when no neutrino oscillations are included, as function of the recoil electron energy. Over most of the spectrum, this ratio is constant at $\simeq 0.5$ [23]. At the highest energies, however, there is an excess of events relative to the $0.5 \times \text{SSM}$ prediction. This is seen in Fig. 28 where the SK results from 825 days of data acquisition [23] are shown by the points (the error bars denote the combined statistical and systematic error); the dotted line is the $0.5 \times \text{SSM}$ prediction.

To study the effects of our new value for the S -factor, 10.1×10^{-20} keV b (see Table XII) to the SK spectrum, we introduce the ratio α of the *hep* flux to its SSM value as

$$\alpha \equiv \frac{S_{\text{new}}}{S_{\text{SSM}}} \times P_{\text{osc}} , \quad (273)$$

where P_{osc} is the observed suppression factor due to neutrino oscillations. Therefore, if *hep* neutrino oscillations are ignored, then $\alpha = (10.1 \times 10^{-20} \text{ keV b}) / (2.3 \times 10^{-20} \text{ keV b}) = 4.4$, while if the *hep* neutrinos are suppressed by $\simeq 0.5$, then $\alpha = 2.2$. The long-dashed and solid lines in Fig. 28 indicate the effect of these two different values of α on the ratio of the electron spectrum with both ${}^8\text{B}$ and *hep* to that with only ${}^8\text{B}$ (the SSM). Two other arbitrary values of α (10 and 20) are shown for comparison.

From Fig. 28, we can conclude that the enhancement of the S -factor found in this calculation, although large, is not enough to completely resolve the discrepancies between the present SK results and the SSM predictions. However, this accurate calculation of the S -factor, and the consequent absolute prediction for the *hep* neutrino flux, will allow much greater discrimination among the proposed solutions to this problem, based on different solar neutrino oscillation scenarios.

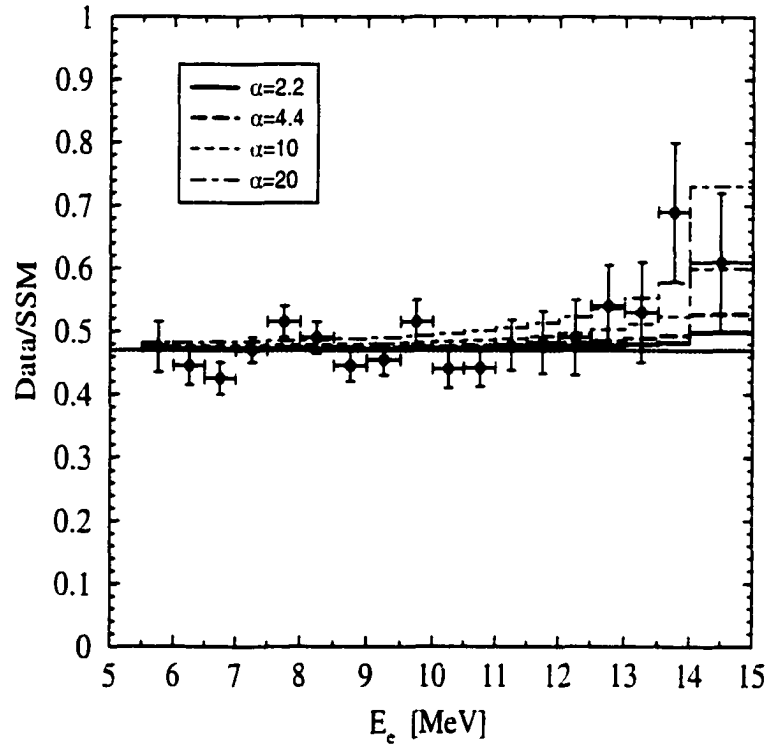


FIG. 28: Electron energy spectrum for the ratio between the Super-Kamiokande 825-days data and the expectation based on unoscillated ${}^8\text{B}$ neutrinos [24]. The data are taken from Ref. [23]. The 5 curves from the bottom to the top correspond respectively to no *hep* contribution (dotted line), $\alpha=2.2$, 4.4, 10, 20, with α defined in Eq. (273).

Chapter 8

Conclusions

In the present thesis, we have reported on accurate calculations for three nuclear processes: elastic electron-scattering on ^3H and ^3He [13], ^3He electrodisintegration at threshold [15], and the *hep* reaction [14, 16]. We have used a non-relativistic approach, based on latest generation models for the nuclear Hamiltonian and electroweak currents.

For the first two processes, we have compared our predictions with the available experimental data. Generally, the calculated observables agree well with the measured ones. It should be reemphasized that, in order to achieve such agreement, realistic models for both the nuclear Hamiltonian and electromagnetic transition operators must be used. Indeed, the impulse approximation completely fails to reproduce the experimental results, and many-body contributions to the electromagnetic charge and current operators need to be included to achieve agreement with the data.

Some discrepancies, however, still remain unresolved: the ^3He magnetic form factor first zero occurs at lower momentum transfer q than experimentally observed. Furthermore, the ^3He longitudinal response function at high q seems to be overpredicted by theory. These discrepancies provide important motivations to (i) look for improvements and refinements to models of nuclear interactions and/or electroweak currents, and (ii) perform more accurate experiments in order

to confirm the existing data, some of which have large errors. Indeed, new experimental proposals to investigate these discrepancies are currently under study at the Thomas Jefferson National Accelerator Facility [17].

Finally, the *hep* reaction calculation provides an example of how our approach can be applied to study reactions, which occur in stellar interiors at very low energies and have too small a cross section to be measured experimentally. Some of these processes are very important in determining solar fusion rates and primordial abundances of elements; the importance of accurate theoretical predictions is therefore evident. A systematic study of electroweak capture reactions involving nuclei up to $A \leq 8$ will be the object of future work.

Bibliography

- [1] J. Carlson and R. Schiavilla, *Rev. Mod. Phys.* **70**, 743 (1998).
- [2] R. Machleidt, F. Sammarruca, and Y. Song, *Phys. Rev. C* **53**, R1483 (1996).
- [3] R.B. Wiringa, V.G.J. Stoks, and R. Schiavilla, *Phys. Rev. C* **51**, 38 (1995).
- [4] B.S. Pudliner, V.R. Pandharipande, J. Carlson, S.C. Pieper, and R.B. Wiringa, *Phys. Rev. C* **56**, 1720 (1997).
- [5] R.B. Wiringa, S.C. Pieper, J. Carlson, and V.R. Pandharipande, *nucl-th/0002022*.
- [6] B.S. Pudliner, V.R. Pandharipande, J. Carlson, and R.B. Wiringa, *Phys. Rev. Lett.* **74**, 4396 (1995).
- [7] A. Kievsky, M. Viviani, and S. Rosati, *Nucl. Phys. A* **551**, 241 (1993).
- [8] A. Kievsky, M. Viviani, and S. Rosati, *Nucl. Phys. A* **577**, 511 (1994).
- [9] A. Kievsky, M. Viviani, and S. Rosati, *Phys. Rev. C* **52**, R15 (1995).
- [10] M. Viviani, A. Kievsky, and S. Rosati, *Few-Body Syst.* **18**, 25 (1995).
- [11] M. Viviani, S. Rosati, and A. Kievsky, *Phys. Rev. Lett.* **81**, 1580 (1998).
- [12] R. Schiavilla *et al.*, *Phys. Rev. C* **58**, 1263 (1998).
- [13] L.E. Marcucci, D.O. Riska, and R. Schiavilla, *Phys. Rev. C* **58**, 3069 (1998).

- [14] L.E. Marcucci, R. Schiavilla, M. Viviani, A. Kievsky, S. Rosati, and J.F. Beacom, nucl-th/0006005, submitted to Phys. Rev. C.
- [15] M. Viviani, A. Kievsky, L.E. Marcucci, S. Rosati, and R. Schiavilla, Phys. Rev. C **61**, 064001 (2000).
- [16] L.E. Marcucci, R. Schiavilla, M. Viviani, A. Kievsky, and S. Rosati, nucl-th/0003065, accepted in Phys. Rev. Lett.
- [17] D.W. Higinbotham, private communication.
- [18] J.N. Bahcall and P.I. Krastev, Phys. Lett. B **436**, 243 (1998).
- [19] G. Fiorentini, V. Berezinsky, S. Degl'Innocenti, and B. Ricci, Phys. Lett. B **444**, 387 (1998).
- [20] R. Escrivano, J.M. Frère, A. Gevaert, and P. Monderen, Phys. Lett. B **444**, 397 (1998).
- [21] C.J. Horowitz, Phys. Rev. C **60**, 022801(R) (1999).
- [22] W.M. Alberico, J. Barnabéu, S.M. Bilenky, and W. Grimus, Phys. Lett. B **478**, 208 (2000).
- [23] Y. Suzuki, contribution to Lepton-Photon Symposium 99 (1999), <http://www-sk.icrr.u-tokyo.ac.jp/doc/sk/pub/index.html>.
- [24] J.N. Bahcall, S. Basu, and M.H. Pinsonneault, Phys. Lett. B **433**, 1 (1998).
- [25] R. Schiavilla, R.B. Wiringa, V.R. Pandharipande, and J. Carlson, Phys. Rev. C **45**, 2628 (1992).
- [26] R.B. Wiringa, R.A. Smith, and T.L. Ainsworth, Phys. Rev. C **29**, 1207 (1984).
- [27] R.B. Wiringa, Phys. Rev. C **43**, 1585 (1991).

- [28] R.A. Arndt, L.D. Roper, R.L. Workman, and M.W. McNaughton, Phys. Rev. D **45**, 3995 (1992).
- [29] V.G.J. Stoks, R.A.M. Klomp, C.P.F. Terheggen, and J.J. de Swart, Phys. Rev. C **49**, 2950 (1994).
- [30] V.G.J. Stoks, R. Timmermans, and J.J. de Swart, Phys. Rev. C **47**, 512 (1993).
- [31] R.A. Arndt, R.L. Workman, and M.M. Pavan, Phys. Rev. C **49**, 2729 (1994).
- [32] T.E.O. Ericson, *et al.*, Phys. Rev. Lett. **75**, 1046 (1995).
- [33] R.A. Arndt, I.I. Strakovsky, and R.L. Workman, Phys. Rev. C **52**, 2246 (1995).
- [34] D.V. Bugg and R. Machleidt, Phys. Rev. C **52**, 1203 (1995).
- [35] V.G.J. Stoks and J.J. de Swart, Phys. Rev. C **42**, 1235 (1990).
- [36] J.L. Friar, G.L. Payne, V.G.J. Stoks, and J.J. de Swart, Phys. Lett. B **311**, 4 (1993).
- [37] J. Fujita and H. Miyazawa, Progr. Theor. Phys. **17**, 360 (1957).
- [38] R.B. Wiringa, V. Ficks, and A. Fabrocini, Phys. Rev. C **38**, 1010 (1988).
- [39] W. Glöckle, *The Quantum Mechanical Few-Body Problem* (Springer-Verlag, Berlin-Heidelberg, 1983).
- [40] C.R. Chen, G.L. Payne, J.L. Friar, and B.F. Gibson, Phys. Rev. C **33**, 1740 (1986).
- [41] W. Glöckle *et al.*, Few Body Syst. Suppl. **8**, 9 (1995).
- [42] J.L. Ballot and M. Fabre de la Ripelle, Ann. Phys. (NY) **127**, 62 (1980).
- [43] M. Fabre de la Ripelle, Ann. Phys. (NY) **147**, 281 (1983).

- [44] A. Kievsky, S. Rosati, and M. Viviani, Nucl. Phys. A **501**, 503 (1989).
- [45] A. Kievsky, S. Rosati, and M. Viviani, Phys. Rev. Lett. **82**, 3759 (1999).
- [46] M. Viviani, private communication.
- [47] A. Kievsky *et al.*, Phys. Rev. C **58**, 3085 (1998).
- [48] K.F. Famularo *et al.*, Phys. Rev. **93**, 928 (1954)
- [49] E. George and L.D. Knutson, private communication.
- [50] M. Viviani, A. Kievsky, and S. Rosati, in preparation (2000).
- [51] J. Carlson, D.O. Riska, R. Schiavilla, and R.B. Wiringa, Phys. Rev. C **44**, 619 (1991).
- [52] T. deForest and J.D. Walecka, Adv. Phys. **15**, 1 (1966).
- [53] J.L. Friar, Ann. Phys. **81**, 332 (1973).
- [54] D.O. Riska, Prog. Part. Nucl. Phys. **11**, 199 (1984).
- [55] M. Chemtob and M. Rho, Nucl. Phys. A **163**, 1 (1971); **212**, 628 (1973).
- [56] D.O. Riska, Phys. Scr. **31**, 107 (1985).
- [57] D.O. Riska, Phys. Scr. **31**, 471 (1985).
- [58] D.O. Riska and M. Poppius, Phys. Scr. **32**, 581 (1985).
- [59] P.G. Blunden and D.O. Riska, Nucl. Phys. A **536**, 697 (1992).
- [60] K. Tsushima, D.O. Riska, and P.G. Blunden, Nucl. Phys. A **559**, 543 (1993).
- [61] A. Buchmann, W. Leidemann, and H. Arenhövel, Nucl. Phys. A **443**, 726 (1985).
- [62] K. Ohta, Nucl. Phys. A **495**, 564 (1989).

- [63] K. Ohta, Phys. Rev. C **39**, 2302 (1989).
- [64] H. Berg *et al.*, Nucl. Phys. A **334**, 21 (1980).
- [65] R. Schiavilla and D.O. Riska, Phys. Rev. C **43**, 437 (1991).
- [66] J.D. Bjorken and S.D. Drell, *Relativistic Quantum Mechanics* (McGraw-Hill, New York, 1964).
- [67] R. Schiavilla, V.R. Pandharipande, and D.O. Riska, Phys. Rev. C **40**, 2294 (1989).
- [68] M. Viviani, R. Schiavilla, and A. Kievsky, Phys. Rev. C **54**, 534 (1996).
- [69] J. Carlson, D.O. Riska, R. Schiavilla, and R.B. Wiringa, Phys. Rev. C **42**, 830 (1990).
- [70] S. Weinberg, Phys. Rev. Lett. **18**, 188 (1967).
- [71] J.L. Friar, Ann. Phys. **104**, 380 (1977).
- [72] S.A. Coon and J.L. Friar, Phys. Rev. C **34**, 1060 (1986).
- [73] R. Schiavilla, V.R. Pandharipande, and D.O. Riska, Phys. Rev. C **41**, 309 (1990).
- [74] Ch. Hajduk, P.U. Sauer, and W. Strueve, Nucl. Phys. A **405**, 581 (1983).
- [75] A. Picklesimer, R.A. Rice, and R. Brandenburg, Phys. Rev. Lett. **68**, 1484 (1992).
- [76] J. Lomnitz-Adler, V.R. Pandharipande, and R.A. Smith, Nucl. Phys. A **361**, 399 (1981).
- [77] R.B. Wiringa, private communication.
- [78] V.G.J. Stoks, R.A.M. Klomp, M.C.M. Rentmeester, and J.J. de Swart, Phys. Rev. C **48**, 792 (1993).

- [79] C.E. Carlson, Phys. Rev. D **34**, 2704 (1986).
- [80] D. Lin and M.K. Liou, Phys. Rev. C **43**, R930 (1991).
- [81] T.E.O. Ericson and W. Weise, *Pions and Nuclei* (Clarendon Press, Oxford, 1988).
- [82] E. Adelberger *et al.*, Rev. Mod. Phys. **70**, 1265 (1998).
- [83] Particle Data Group, R.M. Barnett *et al.*, Phys. Rev. D **54**, 1 (1996).
- [84] H. Abele *et al.*, Phys. Lett. B **407**, 212 (1997).
- [85] M. Gmitro and P. Truöl, Adv. Nucl. Phys. **18**, 241 (1987).
- [86] I.S. Towner, Phys. Rep. **155**, 263 (1987).
- [87] R. Machleidt, Adv. Nucl. Phys. **19**, 189 (1989).
- [88] M. Kirchbach, D.O. Riska, and K. Tsushima, Nucl. Phys. A **542**, 616 (1992).
- [89] E.K. Warburton, Phys. Rev. Lett. **66**, 1823 (1991); Phys. Rev. C **44**, 233 (1991).
- [90] K. Kubodera, J. Delorme, and M. Rho, Phys. Rev. Lett. **40**, 755 (1978).
- [91] I.S. Towner, Nucl. Phys. A **542**, 631 (1992).
- [92] T. W. Donnelly and I. Sick, Rev. Mod. Phys. **56**, 461 (1984).
- [93] J.D. Walecka, *Theoretical Nuclear and Subnuclear Physics* (Oxford University Press, New York, 1995).
- [94] A.R. Edmonds, *Angular Momentum in Quantum Mechanics* (Princeton University Press, Princeton, 1957).
- [95] N. Metropolis *et al.*, J. Chem. Phys. **21**, 1087 (1953).
- [96] H. Collard *et al.*, Phys. Rev. **138**, 357 (1965).

- [97] J.S. McCarthy, I. Sick, and R. Whitney, Phys. Rev. C **15**, 1396 (1977).
- [98] Z.M. Szalata *et al.*, Phys. Rev. C **15**, 1200 (1977).
- [99] R.G. Arnold *et al.*, Phys. Rev. Lett. **40**, 1429 (1978).
- [100] J.M. Cavedon *et al.*, Phys. Rev. Lett. **49**, 978 (1982).
- [101] P.C. Dunn *et al.*, Phys. Rev. C **27**, 71 (1983).
- [102] C.R. Ottermann *et al.*, Nucl. Phys. A **435**, 688 (1985).
- [103] F.P. Juster *et al.*, Phys. Rev. Lett. **55**, 2261 (1985).
- [104] D.H. Beck *et al.*, Phys. Rev. Lett. **59**, 1537 (1987).
- [105] A. Amroun *et al.*, Nucl. Phys. A **579**, 596 (1994).
- [106] M. Gari and W. Krümpelmann, Phys. Lett. B **173**, 10 (1986).
- [107] M.K. Jones *et al.*, Phys. Rev. Lett. **84**, 1398 (2000).
- [108] R. Schiavilla, *Perspectives in Nuclear Physics at Intermediate Energies*, S. Boffi, C. Ciofi degli Atti, and M. Giannini, eds., (World Scientific, Singapore, 1996).
- [109] W. Strueve, Ch. Hajduk, P.U. Sauer, and W. Theis, Nucl. Phys. A **465**, 651 (1987).
- [110] T.W. Donnelly and A.S. Raskin, Ann. Phys. (N.Y.) **169**, 247 (1986).
- [111] G.A. Retzlaff *et al.*, Phys. Rev. C **49**, 1263 (1994).
- [112] R.F. Frosch *et al.*, Phys. Lett. **24B**, 54 (1967); B.T. Chertok *et al.*, Phys. Rev. Lett. **23**, 34 (1969); P.T. Kan *et al.*, Phys. Rev. C **12**, 1118 (1975); G. Köbschall *et al.*, Nucl. Phys. A **412**, 294 (1983).
- [113] Y. Fukuda *et al.*, Phys. Rev. Lett. **82**, 2430 (1999).

- [114] M.B. Smy, hep-ex/9903034.
- [115] J.C. Hardy, I.S. Towner, V.T. Koslowsky, E. Hagberg, and H. Schmeing,
Nucl. Phys. A **509**, 429 (1990).

Vita

Laura Elisa Marcucci
Department of Physics
Old Dominion University
Norfolk, VA 23529

Date and Place of Birth: 12/12/1971. Lucca, Italy

Education:

Ph.D. in Theoretical Nuclear Physics, June 2000: Old Dominion University

Dissertation: *Electroweak Structure of Three- and Four-Body Nuclei*

Laurea in Physics, November 1995: University of Pisa, Italy

Thesis: *Accurate Calculations of $A=3$ Nuclei*, awarded *summa cum laude*

Awards: Luise Meyer-Schutzmeister Award, Year 2000

Recent Publications:

1. A. Kievsky *et al.*, Few-Body Systems, **22**, 1 (1997)
2. L.E. Marcucci *et al.*, Phys. Rev. C **58**, 3069 (1998)
3. M. Viviani *et al.*, Phys. Rev. C **61**, 064001 (2000)
4. L.E. Marcucci *et al.*, nucl-th/0003065, accepted in Phys. Rev. Lett.
5. L.E. Marcucci *et al.*, preprint JLAB-THY-00-15, submitted to Phys. Rev. C

Typeset using L^AT_EX.